TECHNISCHE UNIVERSITÄT WIEN

DISSERTATION

On The Infrared Divergence and Basis Set Completeness Of Coupled-Cluster Theories

zur Erlangung des akademischen Grades

Doktor der technischen Wissenschaften

eingereicht von

Nikolaos Masios

Matrikelnummer 11838929

ausgeführt am Institut für Theoretische Physik
der Fakultät für Physik der Technischen Universität Wien

Betreuer: Univ.-Prof. Dr. Andreas Grüneis

Wien, am 15.4.2024, _____ _____

(Unterschrift Verfasser/in) (Unterschrift Betreuer/in)

Eidesstattliche Erklärung

Hiermit erkläre ich, dass ich diese Arbeit selbständig verfasst habe, dass ich die verwendeten Quellen und Hilfsmittel vollständig angegeben habe und dass ich die Stellen der Arbeit - einschließslich Tabellen, Karten und Abbildungen -, die anderen Werken oder dem Internet im Wortlaut oder dem Sinn nach entnommen sind, auf jeden Fall unter Angabe der Quelle als Entlehnung kenntlich gemacht habe.

Unterschrift: _____

Datum: _____

Ort: _____

Στους γονείς μου,

Βιργινία και Γιώργο.

Ithaka gave you the marvelous journey.
Without her you wouldn't have set out.
She has nothing left to give you now.

-C. P. Cavafy

Contents

Acknowledgments

In our field, it is rare to find professors who are characterized by humility, generosity, and create a working environment that feels like family. For these reasons, I am sincerely grateful to my supervisor, Prof. Andreas Grüneis, for welcoming me to his research group and for the fruitful collaboration we have had. I extend special thanks to my colleagues, Alejandro Gallo, Faruk Salihbegovic, Felix Hummel, Tobias Schäfer, for the scientific discussions, valuable help, and time we shared during these years. My greatest appreciation goes to Andreas Irmler, whose persistence, guidance, and care played a pivotal role in shaping this work. I wish them all a successful and fulfilling future.

To my friends, who are nothing less than family–Danny, Spyros, Maria, and Paris–I am grateful not only for your unconditional support during challenging times but also for always being truthful with me.

To the person who unexpectedly entered my life in the final stretch; my sweet Lara and our memories.

Lastly, I owe everything to my two heroes, Virginia and George. Without your love, values, strength, and support, nothing would be feasible. This work is dedicated to you and to your unfulfilled dreams.

Abstract

It is said that for a civilization to thrive, three essential pillars must develop independently while also complementing each other: ethics or moral philosophy, science, and politics. If any of these pillars falters, the civilization may be deemed stagnant or at risk of collapse. In an analogous manner, science, containing physics, consists of the two foundational pillars of theory and experiment, shaping our comprehension of the world for centuries. Their ongoing interplay has been vital for explaining and predicting physical phenomena and properties of a plethora of materials.

In our technologically ever-growing and fast-paced era, computing has quickly evolved to become the *third pillar* of science, bridging the gap between theory and experiment. Although, the affordability in computational power and memory has increased unimaginably over the decades, certain computationally-based theories still fail to accurately describe or predict physical properties for some classes of materials. For instance, the state-of-the-art Density Functional Theory, for the last 60 years, provides a decent trade-off between accuracy and computational cost, but exhibits limitations when applied to specific systems owing to approximations in the existing exchange-correlation functionals. Hence, the development of wavefunction methods, such as coupled-cluster theory, that offer a systematically improvable treatment of correlation effects, is of paramount significance.

Following two introductory chapters, this work is divided into two major parts. Chapter 3, focuses on CCSD and CCSD(T) methods applied to the Uniform Electron Gas in the thermodynamic limit. We blend existing analytical proofs with our own analytical and numerical findings to provide a clear understanding of the infrared divergences in zero-gap systems. This lays the theoretical foundation of a new method, CCSD(cT). When applied to metallic lithium, this method exhibits remarkable agreement with experimental estimates. It maintains the advantages of the widely used CCSD(T),

such as being accurate for insulating systems and computationally more efficient than including all triple excitations. In Chapter 4, a detailed analysis on the convergence of correlation energies is presented, along with associated quantities, with respect to the size of the employed basis set of coupled-cluster theories, such as CCSD, CCSD(T), and CCSD(cT). The truncation of the basis functions introduces a basis set incompleteness error (BSIE), altering the electronic wavefunction and pair correlation at short inter-electronic distances. A comprehensive exploration of coupled-cluster theories in this context provides valuable corrections to the BSIE, not only saving substantial computational resources but also enhancing our understanding of short-range correlation effects.

Zusammenfassung

Es wird gesagt, dass für eine Zivilisation, um gedeihen zu können, drei wesentliche Säulen unabhängig voneinander entwickeln müssen, während sie sich auch gegenseitig ergänzen: Ethik oder Moralphilosophie, Wissenschaft und Politik. Wenn eine dieser Säulen ins Wanken gerät, könnte die Zivilisation als stagnierend oder gefährdet eingestuft werden. Auf analoge Weise besteht die Wissenschaft, die die Physik umfasst, aus den beiden grundlegenden Säulen der Theorie und des Experiments, die seit Jahrhunderten unsere Auffassung von der Welt prägen. Ihr fortwährendes Zusammenspiel war entscheidend für die Erklärung und Vorhersage physikalischer Phänomene und Eigenschaften einer Vielzahl von Materialien.

In unserer technologisch stetig wachsenden und schnelllebigen Ära hat sich die Informatik schnell zu der *dritten Säule* der Wissenschaft entwickelt, die die Kluft zwischen Theorie und Experiment überbrückt. Obwohl die Erschwinglichkeit von Rechenleistung und Speicherplatz in den letzten Jahrzehnten unglaublich zugenommen hat, versagen bestimmte rechnergestützte Theorien immer noch darin, die physikalischen Eigenschaften für einige Materialklassen genau zu beschreiben oder vorherzusagen. Die Density Functional Theory, beispielsweise, bietet seit 60 Jahren einen guten Kompromiss zwischen Genauigkeit und Rechenkosten, zeigt jedoch Grenzen auf, wenn sie auf bestimmte Systeme angewendet wird, aufgrund von Approximationen in den bestehenden Austausch-Korrelations-Funktionalen. Daher ist die Entwicklung von Wellenfunktionsmethoden, wie der Coupled-Cluster-Theorie, die eine systematisch verbesserbare Behandlung von Korrelationseffekten bietet, von höchster Bedeutung.

Nach zwei einführenden Kapiteln ist diese Arbeit in zwei Hauptteile unterteilt. Kapitel 3 konzentriert sich auf die Anwendung von CCSD- und CCSD(T)-Methoden auf das Uniforme Elektronengas im thermodynamischen Grenzwert. Wir kombinieren bestehende analytische Beweise mit unseren eigenen analytischen und numerischen Ergeb-

nissen, um ein klares Verständnis der Infrarot-Divergenzen in Systemen ohne Bandlücke zu vermitteln. Dies legt den theoretischen Grundstein für eine neue Methode, CCSD(cT). Wenn sie auf metallisches Lithium angewendet wird, zeigt diese Methode bemerkenswerte Übereinstimmung mit experimentellen Ergebnissen. Sie behält die Vorteile der weit verbreiteten CCSD(T)-Methode bei, wie die Genauigkeit für isolierende Systeme und die rechnerische Effizienz im Vergleich zur Einbeziehung aller Dreifachanregungen. In Kapitel 4 wird eine detaillierte Analyse zur Konvergenz der Korrelationsenergien mit zugehörigen Größen im Hinblick auf die Größe des verwendeten Basis-Sets von Coupled-Cluster-Theorien, wie CCSD, CCSD(T) und CCSD(cT), präsentiert. Die Abschneidung der Basisfunktionen führt zu einem Fehler der Basisunvollständigkeit (BSIE), der die elektronische Wellenfunktion und die Paarkorrelation bei kurzen interelektronischen Abständen verändert. Eine umfassende Erforschung von Coupled-Cluster-Theorien in diesem Kontext liefert wertvolle Korrekturen für die BSIE, die nicht nur erhebliche Rechenressourcen sparen, sondern auch unser Verständnis der Kurzreichweiten-Korrelationseffekte verbessern.

Introduction

For almost 2.500 years, the revolutionary idea proposed by Leucippus and Democritus —that nature is comprised of atoms and void— debunked the prevailing Pre-Socratic philosophies of cosmology and cosmogony, which attributed the building blocks of nature to the four basic elements. This statement was the cornerstone that paved the way for a gradual scientific evolution until the *Golden Age* of the 20th century and the emergence of quantum mechanics. The quest for the "Holy Grail", that of solving the Schrödinger equation for any system, thus granting access to observables, has been of great significance since then.

Certainly though, over the years, physics has always been closely intertwined with the development of technology, each acting as a stimulus for the advancement of the other. This exponential growth led us into the advent of the *Computer age*, with the development of efficient algorithms and programs nowadays enabling us to tackle systems and regimes that were previously inaccessible, even just a decade ago.

Nevertheless, even after such a progress, as physicists, we still encounter certain limitations. A prominent example of such constraints is evident in electronic structure theory, specifically the challenge of electronic correlation. Mean-field approximations are, presently, considered adequate enough for interpreting physical systems, where electrons are portrayed as itinerant and distributed throughout the entire medium. However, these theories start to falter when correlations become significant, and the localized character of the electrons on short time-scales coexists with the itinerant character on long time-scales. This is when mean-field theories not only fail to accurately capture this crossover, but also struggle to predict associated properties. Despite various methods employing model Hamiltonians striving to predict properties of these specific systems, *ab initio* methods are now deemed more essential than ever.

The significance of electronic correlations was heightened in 2023 when the Nobel prize was awarded for *generating attosecond pulses of light for the study of electron dynamics in matter*. This groundbreaking discovery opened the door to tracking, in real-time, the movement and rearrangement of electrons in atoms and molecules, such as during the breaking of a chemical bond. Therefore, due to technological advancements of our era, the development of wavefunction theories and approximations that can accurately capture electronic correlations becomes increasingly crucial, as their impact can now be measured at more precise energy and time scales.

Examples of this importance include describing potential energy surfaces of molecules, providing information about molecular structure and geometry, including bond lengths and angles, determining ionization potentials and electron affinities, studying the impact of defects, impurities, and dopants on the electronic and structural properties of materials, understanding their behaviors, obtaining information about the electronic density distribution during reactions and how it affects the overall catalytic process, and gaining an understanding of phase transitions in condensed matter systems, among other applications.

One of the most successful methods in modeling the physical properties of systems that do not exhibit strong correlation character is Density Functional Theory (DFT). However, when it comes to describing strong electronic correlation, the shortcomings arise from the approximate nature of the exchange-correlation (XC) functionals. If exact, these functionals would accurately capture the quantum nature of matter. An illustrative example of the limitations of DFT based on all currently employed XC functionals is the stretched H_2 molecule. For that reason, wavefunction methods, which improve upon mean-field theories, are necessary for the inclusion of the missing electronic correlation.

One of the most popular wavefunction-based theories is coupled-cluster theory. Initially introduced in nuclear physics and quantum chemistry, efforts were made to extend the application of this post-Hartree-Fock wavefunction method to periodic systems. Notably, coupled-cluster with singles and doubles excitations [CCSD] and coupled-cluster with singles, doubles, and perturbative triples [CCSD(T)], which have already proven

to be adequate for achieving chemical accuracy in weakly correlated molecular systems, have also demonstrated high accuracy in predicting properties for both insulating and semiconducting solids.

While the performance of CCSD in metallic solids lags behind that of Density Functional Theory (DFT) using approximate exchange-correlation (XC) functionals, there is promise in its ability to yield reasonably accurate energy predictions. If systematically improved, it could play an essential role in materials development and optimization. Unfortunately, CCSD(T), like other perturbative methods, appears problematic in metallic systems due to the so-called infrared catastrophe. Therefore, higher levels of excitations in coupled-cluster theory need to be included for the systematic improvement of calculated properties. However, this comes at a higher computational and memory cost, as the scaling depends on system size, leading the community to search for elegant approximations that can capture both computational efficiency and accuracy.

When employed in conjunction with DFT, these methods can complement each other, contributing to a better physical and chemical understanding of the electronic structure of matter. Additionally, producing accurate benchmark results will assist the entire electronic structure theory community in further improving computationally efficient *ab initio* theories and interpreting experimental findings more reliably.

Context and framework of the thesis

In this work, the author has implemented and developed an efficient code within the framework of coupled-cluster theories, allowing one to perform *ab initio* calculations on the uniform electron gas model. The latter has long served as an archetype for the material category of simple metals. Our main focus was on investigating two limiting cases, where much of the intriguing physics consistently emerges: the long-range and short-range regimes. Proper treatment of the correlation effects in these domains is crucial for establishing reliable and highly accurate many-electron theories in condensed-matter systems.

Through a detailed analysis of current coupled-cluster theories, their limitations in the long-range regime has been addressed, such as infrared divergencies, and a new method has been introduced that yields convergent correlation energies in metallic systems. Computationally, this regime is approached by increasing systematically the system sizes, eventually extrapolating to the thermodynamic limit. This limit is essential for understanding the properties of solids and establishing benchmarks for experimental data.

Furthermore, when following the path of the Schrödinger equation, one operates within a truncated Hilbert space of single particle orbitals. This truncation has a significant impact on the description of correlation effects at short interelectronic distances, introducing errors in resolving the electronic wavefunction when two electrons are in close proximity. Given these considerations, a thorough investigation has been conducted into the asymptotic behavior of existing coupled-cluster theories concerning short interelectronic separations. Additionally, insights gained from these short distances can contribute valuable information about the pair correlation function. If connected to the exchange-correlation hole density, can lead to improved exchange-correlation functionals for DFT.

Overall, the main structure of the thesis is organized as follows:

- Chapter 1, briefly presents the key theoretical methods essential for and employed in the subsequent chapters of the work. Following the Hartree-Fock mean-field theory, post-Hartree-Fock methods are introduced, including Møller-Plesset perturbation theory and coupled-cluster hierarchies.

- In Chapter 2, the theoretical framework for the Uniform Electron Gas toy model is presented, indicating the necessary modifications for computational calculations. Furthermore, small numerical applications of the aforementioned theories on the Uniform Electron Gas were performed, aiming to get acquainted with the computational caveats that arise, such as finite-size effects and basis set incompleteness error, and discussing methods of overcoming these challenges.

- Chapter 3 is devoted to a detailed analysis of CCSD and CCSD(T) methods when applied to the paradigm of the Uniform electron gas in the thermodynamic limit. By integrating pre-existing analytical proofs with our numerical results, a new method has been introduced, termed *coupled-cluster singles, doubles with perturbative complete triples* [CCSD(cT)]. When applied to metallic lithium, this method demonstrates excellent agreement with experimental estimates, retaining all the desirable properties of CCSD(T), such as accuracy for insulating systems and low computational cost compared to full, iterative inclusion of triple excitations.

- Chapter 4 serves as a pedagogical analysis, focusing on the convergence of correlation energies, along with related quantities, with respect to the employed basis set size for coupled-cluster theories, such as CCSD, CCSD(T), and CCSD(cT). The truncation of these basis functions gives rise to a basis set incompleteness error (BSIE), shaping both the electronic wavefunction and the pair correlation at short interelectronic distances. A thorough examination of the coupled-cluster theories in this domain offers meaningful corrections to the BSIE, not only saving significant computational resources but also enhancing our understanding of short-range correlation effects.

- In Chapter 5, we conclude and provide a brief summary of the key points covered and discussed throughout this work.

Finally, we note that in this work nuclear vibrations, relativistic effects, etc, are excluded and all calculations are performed at zero temperature. Moreover, the Einstein summation convention applies to repeated indices throughout this work.

Chapter 1

Theory is knowledge that sometimes works, and sometimes does not

Nearly a century has elapsed since the introduction of one of the most famous equations in the history of mankind [1]. However, Schrödinger's equation remains exactly solvable only for atomic hydrogen and certain one-electron molecules or ions. The reason lies in the electrostatic interactions among the electrons, which could be characterized as the doubled-edged sword of physics. While crucial, when combined with the intrinsic quantum properties of electrons, for the plethora of materials constituting our world, they also play a pivotal role in complicating the solution of Schrödinger's equation.

Despite living in the most advanced technological era humanity has ever witnessed, computational limitations persist, even when dealing with systems involving some dozens of electrons. This constraint is often referred to as the "exponential wall" [$\mathcal{O}(e^N)$]. We can comprehend, thus, how much higher the complexity is in a solid, where the number of atoms reaches Avogadro's scale. Therefore, approximations that address the *Gordian knot* of the many-body problem in materials science are of paramount

significance. One such approach involves the quest for effective one-particle approximations to solve the original many-body problem.

1.1 The many-body puzzle

In the non-relativistic limit the Hamiltonian of the many-body problem can be expressed as,

$$\hat{H} = \hat{H}^{(n)}_{\text{kin}} + \hat{H}^{(e)}_{\text{kin}} + \hat{H}^{(n-n)}_{\text{int}} + \hat{H}^{(e-n)}_{\text{int}} + \hat{H}^{(e-e)}_{\text{int}}, \tag{1.1}$$

where the superscripts e and n refer to electron and nuclei, respectively. Solving Eq. (1.1) will give us access to the full wavefunction of the many-body problem, consequently enabling the calculation of all observable properties. However, the first simplification occurs with the decoupling of degrees of freedom of electrons and nuclei, known as the Born-Oppenheimer approximation. As the nuclei are significantly heavier than the electrons, they can be treated as stationary on all timescales relevant to the electrons. Moreover, the nuclei-nuclei interaction only introduces a constant shift to the total energy of the system. Consequently, the first and third terms in Eq. (1.1) can be omitted, resulting in the electronic many-body Hamiltonian given by,

$$\hat{H} = \underbrace{-\frac{1}{2}\sum_{i=1}^{N}\nabla_i^2 - \sum_{i,I}^{N,N_I}\frac{Z_I}{|\mathbf{r}_i - \mathbf{R}_I|}}_{\hat{H}_1} + \underbrace{\frac{1}{2}\sum_{i\neq j}^{N}\frac{1}{|\mathbf{r}_i - \mathbf{r}_j|}}_{\hat{H}_2}. \tag{1.2}$$

Here, $\mathbf{r}_i$ and $\mathbf{R}_I$ represent the positions of the i-th electron and I-th nucleus of the system. Additionally, the one-body operators in the first and second terms, denoted as $\hat{H}_1$, account for the kinetic energy of the electrons and the electrostatic interactions with the nuclei, respectively, while the third term, the two-body operator ($\hat{H}_2$) corresponds to the Coulomb repulsion between the electrons.

In the following sections, we will discuss theoretical methods that offer an approximate solution to Eq. (1.2).

1.2 The mean-field Hartree-Fock method

Hartree-Fock (HF) approximation is a method employed in quantum chemistry and condensed matter physics to address the many-electron Schrödinger equation by providing an approximate solution. It simplifies the problem by treating each electron independently, much like in Bloch's theorem or Density Functional Theory (DFT) through Kohn-Sham equations. HF is commonly referred to as a mean-field theory because each electron interacts electrostatically with the average charge distribution of the other $N-1$ electrons. Despite its simplicity, HF plays a crucial role in understanding the origin and accurately capturing around 98% of the total energy [2]. Furthermore, it serves as the starting point for more advanced methods that focus on electronic correlations.

To describe the entire system of electrons, Hartree initially employed a trial wave function in a Rayleigh-Ritz variational calculation, taking the form of a product of single-particle orbitals. However, wavefunctions of this form are inconsistent with Pauli's exclusion principle, as they lack antisymmetry under the exchange of any two coordinates.

A practice that ensures the antisymmetry of the wavefunction is to represent it as a Slater determinant of independent particle wavefunctions. The Slater determinant (SD) can be expressed in shorthand as a product of diagonals:

$$|\Phi_0\rangle = |ijk\ldots n\rangle\,, \tag{1.3}$$

where the letters i, j, k, ..., n correspond to the set of spin-orbitals $\{\phi_i\}$ with arbitrary spin. By applying Slater-Condon rules, we can evaluate one- and two-electron integrals. Since the Hamiltonian involves two-body operators, we consider a SD for two electrons. According to the variational principle, the optimal spin orbitals are those that minimize the electronic energy:

$$E_{\mathrm{HF}} = \min_{\{\phi_n\}} \langle\Phi_0|\,\hat{H}\,|\Phi_0\rangle = \min_{\{\phi_n\}} [\langle\Phi_0|\,\hat{H}_1\,|\Phi_0\rangle + \langle\Phi_0|\,\hat{H}_2\,|\Phi_0\rangle], \tag{1.4}$$

$$\langle\Phi_0|\,\hat{H}_1\,|\Phi_0\rangle = \sum_{i=1}^{N}\langle\Phi_0|\,\hat{h}(i)\,|\Phi_0\rangle = \sum_{i=1}^{N}\langle i|\,\hat{h}(i)\,|i\rangle\,, \tag{1.5}$$

$$\langle\Phi_0|\,\hat{H}_2\,|\Phi_0\rangle = \frac{1}{2}\sum_{i,j}^{N}\langle\Phi_0|\,\frac{1}{|\mathbf{r}_i-\mathbf{r}_j|}\,|\Phi_0\rangle \equiv \frac{1}{2}\sum_{i,j}^{N}\Big[\underbrace{\langle ij|\,\frac{1}{r_{ij}}\,|ij\rangle}_{Coulomb\ J_{ij}} - \underbrace{\langle ij|\,\frac{1}{r_{ij}}\,|ji\rangle}_{Exchange\ K_{ij}}\Big]. \tag{1.6}$$

Note that, we can omit the exception $i \neq j$ in Eq. (1.6) since the two terms for $i = j$ in this sum cancel each other out. In a solid, excluding one of the N terms is, of course, without practical significance.[1] Here, the Coulomb operator J_{ij} describes the classical electrostatic repulsion between the charged particles. Specifically, it signifies the average potential that the electron in orbital ϕ_i with coordinates, for instance, r_1, "senses" due to the charge density generated by ϕ_j with coordinates r_2. In a sense, J acts as an effective one-electron operator, as each electron behaves as an independent particle interacting with a mean-field generated by all N electrons. On the other hand, the exchange operator K_{ij} is somewhat unique. It arises directly from the antisymmetry principle, for which there is no classical analogue, and cancels the "unphysical" self-interaction of an electron with its own potential. Exchange integrals assume a form similar to Coulomb integrals, except now the orbital indices i and j are permuted in the ket.

The one-body part of the Hamiltonian in Eq. (1.2) and the two-electron operators can be combined into an effective one-electron operator, namely,

$$\hat{\mathcal{F}} = \hat{h} + \sum_{j}^{N}(\hat{J}_j - \hat{K}_j), \tag{1.7}$$

known as the Fock Operator. The summation for $\hat{J}_j$ and $\hat{K}_j$ includes all occupied orbitals. To systematically solve for $\hat{\mathcal{F}}$ and obtain the corresponding eigenstates and eigenenergies, we employ the framework of the Rayleigh-Ritz variational principle. According to this principle, the Hartree-Fock energy will be an upper bound for the exact energy. Hence, the goal is to minimize, with respect to the orbitals, the expression:

$$\delta\mathcal{L}[\{i\}] = \delta E_{\mathrm{HF}}[\{i\}] - \varepsilon_{ji}\sum_{i,j}^{N}\delta(\langle i|j\rangle - \delta_{ij}) = 0, \tag{1.8}$$

[1] N denotes the number of electrons of the system.

where ε_{ji} being the Lagrange multipliers with constraint $\langle i|j\rangle = \delta_{ij}$, the orthonormality of the orbitals. Without going into much detail, we obtain the non-canonical Hartree-Fock equations:

$$\hat{\mathcal{F}}_i \, |i\rangle = \varepsilon_{ij} \sum_j |j\rangle \, . \tag{1.9}$$

Note that the derived expression doesn't represent an eigensystem since the action of $\hat{\mathcal{F}}$ on $|i\rangle$ does not yield $|i\rangle$. Nevertheless, a unitary transformation of the spin-orbitals can be determined to diagonalize the Lagrange multiplier matrix ε_{ij}. Consequently, we obtain the following canonical Hartree-Fock equations:

$$\hat{\mathcal{F}}_{\tilde{i}} \left|\tilde{i}\right\rangle = \varepsilon_{\tilde{i}} \left|\tilde{i}\right\rangle , \tag{1.10}$$

which appear as a true eigensystem using canonical spin-orbitals. It's crucial to note that despite the occupied orbital rotation, the Fock operator and the energies remain invariant to unitary transformation.

Since $\hat{\mathcal{F}}$ is a one-electron operator, whereas both $\hat{J}_j$ and $\hat{K}_j$ depend on all orbitals, the resulting differential equations need to be solved iteratively. This process is known as the Self-Consistent Field (SCF) procedure. In other words, the Hartree-Fock equations establish a self-consistent field conceptual framework, determined through an iterative method. Typically, starting with a basis of wavefunctions of independent particles, a set of new functions is defined by solving the differential equations. The process repeats until the input and output wavefunctions practically coincide. For convergence, a mixture of the input and output wavefunctions from the previous step usually serves as the input for the next iterative step. From this point onward, the orbitals with the lowest eigenenergies are termed occupied orbitals, while those with higher eigenenergies are referred to as unoccupied or virtual orbitals. It's essential to emphasize that even the Hartree-Fock equations provide an approximate solution to the problem, as obtaining an exact solution would require in general the use of a superposition of Slater determinants.

To calculate the total energy of the system under investigation, we must consider the energy that the Hartree-Fock approximation fails to account for. The term *correlation* energy, introduced by Löwdin, is defined as:

$$E_{\mathrm{c}} = E - E_{\mathrm{HF}}, \tag{1.11}$$

where the missing correlation energy E_c is the difference between the exact, non-relativistic energy E and the HF energy E_{HF}, assuming a complete one-electron basis.

1.3 Stepping into correlations: The Møller-Plesset perturbation theory

Hartree-Fock theory captures only correlation effects induced by spin statistics, i.e., electrons of same spin are correlated in space. To account for dynamic correlations, that emerge due to the Coulomb interaction between the electrons, various post-Hartree-Fock methods have been developed. Among them is the scheme of Rayleigh-Schrödinger perturbation theory on many-body systems, or many-body perturbation theory (MBPT), where the free electrons constitute the solvable unperturbed system with known mathematical solutions, while the electronic interaction is treated as a perturbation. In this section, we will present the particular case of Møller-Plesset (MP) perturbation theory [3], in which the Hartree-Fock solution appears as the zero-order approximation, resulting in a zero first-order energy correction. The famous next-order correction, referred to as MP2, is extensively employed in the fields of quantum chemistry and solid state physics. The reason behind its widespread use is the capture of long-range or van der Waals interactions, which mean-field theories, such as Hartree-Fock or Density Functional Theory (DFT) using approximate and local exchange-correlation (XC) functionals, fail to account for.

To begin with, the Hamiltonian of the many-body system, within the context of MP perturbation theory, reads,

$$\hat{H} = \hat{H}_0 + \hat{\mathcal{V}}, \tag{1.12}$$

where $\hat{H}_0 = \hat{F}$ represents the Fock operator, and $\hat{\mathcal{V}} = \hat{H} - \hat{H}_0$ denotes the perturbation. The zeroth-order ground-state wavefunction solution to the unperturbed Hamiltonian $\hat{H}_0$ is the Hartree-Fock Slater determinant, constructed with canonical orbitals, which are eigenstates of the Fock operator,

$$\hat{H}_0 |\Psi_0\rangle = E_0 |\Psi_0\rangle , \tag{1.13}$$

where E_0 is the zeroth-order energy, given as the sum of the eigenenergies of the canonical Hartree-Fock orbitals in Eq. (1.10). Based on that, the first-order energy correction to the zeroth-order Hamiltonian $\hat{H}_0$, supplemented with the zeroth-order energy, will yield the Hartree-Fock energy, namely,

$$\langle\Psi_0|\,\hat{H}_0\,|\Psi_0\rangle + \langle\Psi_0|\,\hat{\mathcal{V}}\,|\Psi_0\rangle = E_0 + E_1 = E_{\mathrm{HF}}. \tag{1.14}$$

To improve on the HF ground state with MP theory, we must take into account at least the second-order energy correction, expressed as:

$$E_2 = -\sum_{n\neq 0} \frac{|\,\langle\Psi_0|\,\hat{\mathcal{V}}\,|\Psi_n\rangle\,|^2}{E_n - E_0}, \tag{1.15}$$

where $|\Psi_n\rangle$ represents a priori single, double, triple, and so forth, excited determinants. Indeed, as $\hat{\mathcal{V}}$ is a two-body operator, according to Slater's rules, matrix elements involving triple and higher excitations with respect to $|\Psi_0\rangle$ are zero. Additionally, contributions from single excitations, due to Brillouin's theorem, also lead to vanishing terms. Consequently, only double excitations of the form $|\Psi_n\rangle = \left|\Psi_{ij}^{ab}\right\rangle$ contribute.[2] In this case, the two-body part of the perturbation operator yields a non-zero matrix element:

$$\langle\Psi_0|\,\hat{\mathcal{V}}\,\left|\Psi_{ij}^{ab}\right\rangle = \langle ij|ab\rangle - \langle ji|ab\rangle = \langle ij||ab\rangle\,. \tag{1.16}$$

Furthermore, the zeroth-order energy associated with the doubly-excited determinants $\left|\Psi_{ij}^{ab}\right\rangle$ is given by,

$$E_n = E_{ij}^{ab} = E_0 + \epsilon_a + \epsilon_b - \epsilon_i - \epsilon_j, \tag{1.17}$$

leading to the second-order MP energy correction:

$$E_c^{\mathrm{MP2}} = -\frac{1}{4}\sum_{ij}^{\mathrm{occ.}}\sum_{ab}^{\mathrm{vir.}} \frac{|\,\langle ij||ab\rangle\,|^2}{\epsilon_a + \epsilon_b - \epsilon_i - \epsilon_j}. \tag{1.18}$$

In the case of closed-shell systems, assuming each orbital is doubly occupied with spin-up and spin-down electrons, the expression for the MP2 correlation energy can be derived by summing over spin coordinates, specifically,

$$E_c^{\mathrm{MP2}} = -\sum_{ij}^{\mathrm{occ.}}\sum_{ab}^{\mathrm{vir.}} \frac{\langle ij|ab\rangle\,[2\,\langle ab|ij\rangle - \langle ba|ij\rangle]}{\epsilon_a + \epsilon_b - \epsilon_i - \epsilon_j}, \tag{1.19}$$

[2] Here, $\left|\Psi_{ij}^{ab}\right\rangle$ denotes a doubly excited determinant, where two electrons from the occupied orbitals i and j have been excited to the unoccupied, or virtual, orbitals a and b.

where a, b and i, j now represent spatial occupied and virtual orbitals, respectively. Energy expressions for higher order perturbation expansions, denoted as MP3, MP4, and so forth, can be found in the literature.

It is evident from Eq. (1.19) that if the denominator is zero, the MP2 energy diverges. This occurs in periodic systems with zero band gap, such as metals, or in systems exhibiting a small HOMO-LUMO gap. In both cases, MP2 theory fails, and other post-Hartree-Fock methods are needed, albeit computationally expensive.

Additionally, it is worth noting that MP2 implementations typically scale as $\mathcal{O}(N^5)$, where N is a measure of the system size. Nevertheless, successful efforts have been made to reduce this quintic scaling to a quartic or even cubic one [4, 5].

1.4 A powerful post-Hartree-Fock method: The coupled-cluster theory

Since Møller-Plesset perturbation theory exhibits limitations when applied to certain systems, coupled-cluster (CC) theory emerges as a more compact and precise framework for the study of electronic correlations. In this post-Hartree-Fock method, the wavefunction is approximated using a linear combination of Slater determinants by correlating the motions of any number of occupied electrons through *cluster* functions. In fact, these functions replace any number of occupied orbitals-those that provide the minimum energy in the HF approximation-with a linear combination of n-tuples of orbitals belonging to the virtual manifold, where n denotes the number of occupied electrons being correlated. This procedure for obtaining the exact wavefunction of the system can be simplified using second quantization notation, giving rise to an exponential ansatz in the form of,

$$|\Psi\rangle = |\Psi_{\mathrm{CC}}\rangle = e^{\hat{T}} |\Phi_0\rangle \,, \tag{1.20}$$

where $|\Phi_0\rangle$ is the Hartree-Fock, or reference, wavefunction, and $|\Psi\rangle$ represents the exact solution to our many-body problem,

$$\hat{H} |\Psi\rangle = E |\Psi\rangle \,. \tag{1.21}$$

The exponential of the excitation cluster operator $\hat{T}$ is given by the expansion:[3]

$$e^{\hat{T}} = 1 + \hat{T} + \frac{\hat{T}^2}{2!} + \frac{\hat{T}^3}{3!} + \cdots = \sum_{n=0}^{\infty} \frac{\hat{T}^n}{n!}, \tag{1.22}$$

where $\hat{T}$ for an N-electron system is defined as,

$$\hat{T} = \hat{T}_1 + \hat{T}_2 + ... + \hat{T}_N, \tag{1.23}$$

with the subscripts referring to the number of excited electrons. For instance, using second quantization operators, the total one-orbital cluster operator is specified as:

$$\hat{T}_1 = \sum_{\mu} \hat{t}_\mu = \sum_{ia} t_i^a \hat{\alpha}_a^\dagger \hat{\alpha}_i, \tag{1.24}$$

where $\hat{t}_i$ and t_i^a represent the single-orbital cluster operator and its coefficient, respectively. The annihilation operator $\hat{\alpha}_i$ destroys an electron in orbital i from the reference determinant it acts on, while the creation operator $\hat{\alpha}_a^\dagger$ creates an electron in the orbital a. Similarly, the total two-orbital cluster operator is introduced as:

$$\hat{T}_2 = \frac{1}{2} \sum_{\mu,\nu} \hat{t}_{\mu\nu} = \frac{1}{4} \sum_{ijab} t_{ij}^{ab} \hat{\alpha}_a^\dagger \hat{\alpha}_b^\dagger \hat{\alpha}_j \hat{\alpha}_i, \tag{1.25}$$

where electrons in orbitals i and j are annihilated and placed in orbitals a and b. To determine the cluster coefficients, or *amplitudes*, t_i^a, t_{ij}^{ab}, and so forth, we begin by substituting Eq. (1.20) in Eq. (1.21), resulting in,

$$\hat{H} e^{\hat{T}} |\Phi_0\rangle = E e^{\hat{T}} |\Phi_0\rangle . \tag{1.26}$$

Applying a "projective" technique, one can multiply this equation by the reference Φ_0 from the left, obtaining the subsequent expression for the energy,

$$\langle \Phi_0 | \hat{H} e^{\hat{T}} |\Phi_0\rangle = E \langle \Phi_0 | e^{\hat{T}} |\Phi_0\rangle = E, \tag{1.27}$$

where intermediate normalization, i.e. $\langle \Phi_0 | \Psi_{\mathrm{CC}} \rangle = 1$, has been assumed. Additionally, expressions for the cluster amplitudes can be derived by left-projecting Eq. (1.26) onto

[3] The operators $\hat{T}_i$s are referred to as excitation operators, since the determinants they produce from $|\Phi_0\rangle$ resemble excited states in Hartree-Fock theory.

the excited determinants produced by the action of the cluster operator, $\hat{T}$, on the reference, e.g.,

$$\left\langle \Psi_{ij\ldots}^{ab\ldots} \right| \hat{H} e^{\hat{T}} \left| \Phi_0 \right\rangle = E \left\langle \Psi_{ij\ldots}^{ab\ldots} \right| e^{\hat{T}} \left| \Phi_0 \right\rangle , \tag{1.28}$$

where $\left| \Psi_{ij\ldots}^{ab\ldots} \right\rangle$ depicts an excited determinant in which occupied orbitals i, j, etc. have been substituted by virtual, or unoccupied, orbitals a, b, etc. Projections of this type yield a set of nonlinear equations, dependent on energy,[4] for the amplitudes, ultimately leading to the exact wavefunction when the excitation operators are fully included up to the number of electrons. However, despite the insights we can gain from this procedure for the coupled cluster method, its most significant drawback is that these equations are not suited for practical computer implementations.

Before we continue, it is worth noting that by substituting Eq. (1.22) into Eq. (1.27), a natural truncation emerges. Specifically, cubic and higher powers of the cluster operator $\hat{T}$ lead to at least threefold excitations. Since the electronic Hamiltonian consists of one- and two-body operators, according to Slater's rules, the matrix elements between determinants that differ by more than two orbitals are zero.

In order to derive the energy expression and set of amplitude equations suitable for computational implementation we multiply the coupled-cluster Schrödinger equation (1.26) by the inverse of the exponential operator. This leads to the following form, which can also be viewed as an eigenvalue problem,

$$e^{-\hat{T}} \hat{H} e^{\hat{T}} \left| \Phi_0 \right\rangle = E \left| \Phi_0 \right\rangle , \tag{1.29}$$

where the similarity-transformed Hamiltonian $\bar{H} = e^{-\hat{T}} \hat{H} e^{\hat{T}}$, is used in place of the normal electronic Hamiltonian $\hat{H}$. By projecting Eq. (1.29) onto the multi-electron Hilbert space of determinants that describe all possible excitations, namely,

$$\left| \mathcal{H} \right\rangle = \left| \Phi_0 \right\rangle + \left| \Psi_i^a \right\rangle + \left| \Psi_{ij}^{ab} \right\rangle + \left| \Psi_{ijk}^{abc} \right\rangle + \cdots + \left| \Psi_{\overbrace{ijk\ldots\mathcal{L}}^{N}}^{\overbrace{abc\ldots\mathcal{Z}}^{N}} \right\rangle , \tag{1.30}$$

[4] This implies the presence of *unlinked* terms or diagrams in the set of equations, similar to the unlinked diagrams in MBPT. The cancellation of these unlinked terms is of great importance and closely related to the extensivity of the CC method, i.e., the linear scaling of the energy with the number of electrons.

where

$$\left|\Psi^{\overbrace{abc\ldots\mathcal{Z}}^{N}}_{\underbrace{ijk\ldots\mathcal{L}}_{N}}\right\rangle \equiv \prod_{h=a}^{\mathcal{Z}} \hat{\alpha}_h^\dagger \prod_{g=\mathcal{L}}^{i} \hat{\alpha}_g \left|\Phi_0\right\rangle \tag{1.31}$$

we obtain the following modified energy expression and set of amplitude equations,

$$\langle\Phi_0|\,\bar{H}\,|\Phi_0\rangle = E, \tag{1.32}$$
$$\langle\Psi_i^a|\,\bar{H}\,|\Phi_0\rangle = 0, \tag{1.33}$$
$$\left\langle\Psi_{ij}^{ab}\right|\bar{H}\,|\Phi_0\rangle = 0, \tag{1.34}$$
$$\left\langle\Psi_{ijk}^{abc}\right|\bar{H}\,|\Phi_0\rangle = 0, \tag{1.35}$$
$$\vdots$$

The advantage of this procedure is that the set of amplitude equations is now decoupled from the energy expression.[5] Moreover, a simplification occurs when applying the Baker-Campbell-Hausdorff (BCH) formula to the similarity-transformed Hamiltonian $\bar{H}$. This results in a linear combination of nested commutators of the Hamiltonian $\hat{H}$ with the cluster operator $\hat{T}$,

$$\bar{H} = \hat{H} + \left[\hat{H},\hat{T}\right] + \frac{1}{2!}\left[\left[\hat{H},\hat{T}\right],\hat{T}\right] + \frac{1}{3!}\left[\left[\left[\hat{H},\hat{T}\right],\hat{T}\right],\hat{T}\right] + \frac{1}{4!}\left[\left[\left[\left[\hat{H},\hat{T}\right],\hat{T}\right],\hat{T}\right],\hat{T}\right] + \ldots . \tag{1.36}$$

Similar to the natural truncation described earlier for Eq. (1.27), the BCH expansion also exhibits a natural truncation. Specifically, due to the fact that the cluster operators commute with each another, but not with the two-body Coulomb interaction of the Hamiltonian $\hat{H}$, the BCH expansion exactly terminates at fourth order. Thus, by using the truncated expansion, we derive analytic expressions for the commutators in Eq. (1.36). When these expressions are substituted into the energy and amplitude equations and Wick's theorem is applied, an efficient implementation can be achieved. However, one final step remains to be taken: deciding the level of truncation for the cluster operator $\hat{T}$.

[5] The set of these equations is known as the *linked* CC equations, which are equivalent to the *unlinked* equations discussed previously.

1.4.1 The all around coupled-cluster singles and doubles (CCSD) amplitude equations

The truncation of the cluster operator $\hat{T}$ at specific excitation levels is closely related to the available computational resources and the characteristics of the systems under study. This process will eventually introduce a hierarchy of coupled-cluster techniques, such as CCS ($\hat{T} \approx \hat{T}_1$), CCSD ($\hat{T} \approx \hat{T}_1 + \hat{T}_2$) , CCSDT ($\hat{T} \approx \hat{T}_1 + \hat{T}_2 + \hat{T}_3$), and so forth. Hence, the abbreviations S, D, T stand for singles, doubles, and triples excitations, respectively.

One of the most well-known approximations to the cluster operator $\hat{T}$, with a wide application in quantum chemistry and condensed matter physics, is the coupled-cluster singles and doubles method. The CCSD wavefunction ansatz is expressed as follows,

$$|\Psi_{\mathrm{CCSD}}\rangle = e^{\hat{T}_1+\hat{T}_2}\,|\Phi_0\rangle = \Bigg(1 + \hat{T}_1 + \frac{1}{2!}\hat{T}_1^2 + \frac{1}{3!}\hat{T}_1^3 + \frac{1}{4!}\hat{T}_1^4 + \hat{T}_2 + \frac{1}{2!}\hat{T}_2^2 + \hat{T}_2\hat{T}_1 + \frac{1}{2!}\hat{T}_2\hat{T}_1^2 + \ldots\Bigg)\,|\Phi_0\rangle\,. \tag{1.37}$$

To determine the CCSD energy and the so-called cluster amplitudes t_i^a, and t_{ij}^{ab}, we insert Eq. (1.37) into the Schrödinger equation and follow the projecting procedure discussed previously in this section, namely,

$$\langle\Phi_0|\,\tilde{H}\,|\Phi_0\rangle = E_{\mathrm{c}}^{\mathrm{CCSD}}, \tag{1.38}$$

$$\langle\Psi_i^a|\,\bar{H}\,|\Phi_0\rangle = 0, \tag{1.39}$$

$$\left\langle\Psi_{ij}^{ab}\right|\,\bar{H}\,|\Phi_0\rangle = 0. \tag{1.40}$$

Here, we define $\tilde{H} = \bar{H} - E_{\mathrm{HF}}$, and $E_{\mathrm{c}}^{\mathrm{CCSD}}$ represents the correlation energy computed at the CCSD level. For practical implementations, the aforementioned equations need to be reformulated to explicitly involve Hamiltonian matrix elements and amplitudes, making them directly applicable. This can be accomplished through further algebraic transformations, including the Baker-Campbell-Hausdorff (BCH) expansion, Wick's theorem, Slater rules or even diagrammatic techniques.[6] From Eq. (1.38) we can derive

[6] The diagrammatic techniques utilized in coupled-cluster methods share similarities with the Feynman techniques employed in MBPT. However, coupled-cluster terms are represented by Goldstone diagrams, and their "rules" can be found in various textbooks [6].

the correlation energy expression:

$$E_{\mathrm{c}}^{\mathrm{CCSD}} = 2f_a^i t_i^a + w_{ab}^{ij}(t_i^a t_j^b + t_{ij}^{ab}). \tag{1.41}$$

We note that only double and squared single amplitudes appear in the expression of the CCSD correlation energy. This is because higher excitations do not make a direct contribution to the correlation energy, as the electronic Hamiltonian contains at most two-body operators. In addition, the single amplitude t_i^a can be obtained from Eq. (1.39) leading to the equation:

$$\begin{aligned}\Delta_i^a t_i^a = f_i^a - 2f_c^k t_k^a t_i^c + \kappa_c^a t_i^c - \kappa_i^k t_k^a + \kappa_c^k(2t_{ki}^{ca} - t_{ik}^{ca}) + \kappa_c^k t_i^c t_k^a + w_{ic}^{ak} t_k^c \\ + w_{cd}^{ak}(t_{ik}^{cd} + t_i^c t_k^d) - w_{ic}^{kl}(t_{kl}^{ac} + t_k^a t_l^c),\end{aligned} \tag{1.42}$$

while the expression for the double amplitude, following from Eq. (1.40), is given by,

$$\begin{aligned}\Delta_{ij}^{ab} t_{ij}^{ab} = v_{ij}^{ab} + \chi_{ij}^{kl}(t_{kl}^{ab} + t_k^a t_l^b) + \chi_{cd}^{ab}(t_{ij}^{cd} + t_i^c t_j^d) + P\lambda_c^a t_{ij}^{cb} - P\lambda_i^k t_{kj}^{ab} \\ + P(v_{ic}^{ab} - v_{ic}^{kb} t_k^a) t_j^c - P(v_{ij}^{ak} + v_{ic}^{ak} t_j^c) t_k^b + P(2\chi_{ic}^{ak} - \chi_{ci}^{ak}) t_{kj}^{cb} \\ - P\chi_{ic}^{ak} t_{kj}^{cb} - P\chi_{ci}^{bk} t_{kj}^{ac}.\end{aligned} \tag{1.43}$$

Presented here are the closed-shell coupled-cluster singles and doubles amplitude equations for spatial orbitals, which can also be found elsewhere [7]. As evident, the projected equations are nonlinear and coupled with respect to the amplitudes, involving an iterative solution process. Once the amplitudes are obtained, the CCSD correlation energy can be evaluated using Eq. (1.41). The introduced intermediates κ, λ, and χ play a crucial role in reducing the computational cost of the CCSD method from $\mathcal{O}(N^8)$ to $\mathcal{O}(N^6)$. Despite this improvement, the computationally most demanding term is the $v_{cd}^{ab} t_{ij}^{cd}$, requiring N^6 operations. This categorizes CCSD in the computational complexity class of $\mathcal{O}(N^6)$, with memory storage for the double amplitudes of order $\mathcal{O}(N^4)$. The intermediates are expressed as follows:

$$\kappa_i^k = w_{cd}^{kl}(t_{il}^{cd} + t_i^c t_l^d) \tag{1.44}$$

$$\kappa_c^a = -w_{cd}^{kl}(t_{kl}^{ad} + t_k^a t_l^d) \tag{1.45}$$

$$\kappa_c^k = f_c^k + w_{cd}^{kl} t_l^d \tag{1.46}$$

$$\lambda_i^k = \kappa_i^k + f_c^k t_i^c + w_{ic}^{kl} t_l^c \tag{1.47}$$

$$\lambda_c^a = \kappa_c^a - f_c^k t_k^a + w_{cd}^{ak} t_k^d \tag{1.48}$$

$$\chi_{ij}^{kl} = v_{ij}^{kl} + v_{ic}^{kl} t_j^c + v_{cj}^{kl} t_i^c + v_{cd}^{kl}(t_{ij}^{cd} + t_i^c t_j^d) \tag{1.49}$$

$$\chi_{cd}^{ab} = v_{cd}^{ab} - v_{cd}^{ak} t_k^b - v_{cd}^{kb} t_k^a \tag{1.50}$$

$$\chi_{ic}^{ak} = v_{ic}^{ak} - v_{ic}^{lk} t_l^a + v_{dc}^{ak} t_i^d - \frac{1}{2} v_{dc}^{lk}(t_{il}^{da} + 2t_i^d t_l^a) + \frac{1}{2} w_{dc}^{lk} t_{il}^{ad} \tag{1.51}$$

$$\chi_{ci}^{ak} = v_{ci}^{ak} - v_{ci}^{lk} t_l^a + v_{cd}^{ak} t_i^d - \frac{1}{2} v_{cd}^{lk}(t_{il}^{da} + 2t_i^d t_l^a), \tag{1.52}$$

where, $P\{\dots\}_{ij}^{ab} = \{\dots\}_{ij}^{ab} + \{\dots\}_{ji}^{ba}$ is the permutation operator, and the *two-electron Coulomb integrals* w_{ij}^{ab}, are given as $w_{ij}^{ab} = 2\langle ab|ij\rangle - \langle ba|ij\rangle$.

Finally, it is important to note that CCSD includes all the terms from MP2 and MP3 perturbation theory. However, from the MP4 level, it only includes terms associated with pairs of electrons being excited. The strength of the method lies in the resummation of these terms to infinite order. Nevertheless, to incorporate processes that correlate more than two electrons, one has to climb the ladder of the hierarchy of coupled-cluster techniques.

1.4.2 Hidden gems in coupled-cluster theory

After a closer examination of the doubles amplitude equation (1.43), we can identify the following terms:

$$\Delta_{ij}^{ab} t_{ij}^{ab} = v_{ij}^{ab} + 2\, v_{ic}^{ak} t_{kj}^{cb} + 2\, t_{ik}^{ac} v_{cj}^{kb} + 4\, t_{ik}^{ac} v_{cd}^{kl} t_{lj}^{db}. \tag{1.53}$$

A diagrammatic illustration of these terms using Goldstone diagrams corresponds to the topology of *ring* diagrams, which are the hallmark of the historical Random-Phase-Approximation (RPA). This approach was introduced in different frameworks by Bohm and Pines, Macke, and Gell-Mann and Brueckner.

By iteratively solving Eq. (1.53), the resulting *converged* amplitudes can be utilized to calculate the correlation energy. According to Freeman, who applied the ring coupled-cluster doubles (rCCD) equation, as it was named, to the unpolarized electron gas

for various electronic densities, when compared to Hedin's RPA results, the agreement falls within numerical accuracy [8].

Furthermore, Scuseria *et al* [9], through an algebraic analysis of the doubles amplitude equation, concluded that RPA is equivalent to rCCD, comprising a subset of coupled-cluster doubles (CCD) terms, while it can further include an infinite summation of Brueckner's ladder or higher-order exchange diagrams. Additionally, he noted that an $\mathcal{O}(N^4)$ scaling for the evaluation of the doubles amplitude equation is feasible.[7] The revival of RPA in recent years can be attributed to its ability to capture long-range interactions, a feature that is absent in widely used density-functional approximations such as Local Density Approximation (LDA) and Generalized Gradient Approximation (GGA).

1.4.3 Coupled-cluster singles and doubles with perturbative triples [CCSD(T)] approximation

The next anticipated step to improve the wavefunction and correlation energy within the coupled-cluster methodology is the inclusion of triple excitations. Despite several studies demonstrating the importance of triple and higher excitations in accurately predicting various systems properties, their application is restricted to small system sizes. Specifically, the computational cost of coupled-cluster singles, doubles and triples (CCSDT) increases by two orders of magnitude, i.e. $\mathcal{O}(N^8)$, while due to the iterative nature of the method, storage of the triple-excitation amplitudes t_{ijk}^{abc} is necessary. For instance, the memory requirements for a system of 14 electrons and 1.000 unoccupied orbitals nearly approach 2.5TB, when storing the data in double precision.

One approach that is less expensive, resulting in a good trade-off between computational cost and accuracy for a large range of applications in the field of quantum chemistry, is the incorporation of triple excitations in a perturbative manner [10]. On the contrary, when applied to metallic systems, it exhibits a divergence similar to MP2 perturbation theory [11]. The CCSD(T) approximation, as denoted, is characterized

[7] To achieve this, the rCCD formulation is combined with the Cholesky decomposition technique.

by a computational cost of $\mathcal{O}(N^7)$. Due to its perturbative nature, the correlation energy can be calculated without the need for triple amplitude storage. Specifically, the triple excitation amplitudes are given by:

$$\Delta_{ijk}^{abc} t_{ijk}^{abc} = P(t_{ij}^{ae} v_{ek}^{bc} - t_{im}^{ab} v_{jk}^{mc}), \tag{1.54}$$

where the permutation operator is defined as:

$$P\{\dots\}_{ijk}^{abc} = \{\dots\}_{ijk}^{abc} + \{\dots\}_{ikj}^{acb} + \{\dots\}_{kij}^{cab} + \{\dots\}_{kji}^{cba} + \{\dots\}_{jki}^{bca} + \{\dots\}_{jik}^{bac}. \tag{1.55}$$

Based on Eq. (1.54) the correlation energy at the CCSD(T) level can be expressed as:

$$E_{\mathrm{c}}^{\mathrm{CCSD(T)}} = E_{\mathrm{c}}^{\mathrm{CCSD}} + \bar{t}_{abc}^{\,ijk} t_{ijk}^{abc} \Delta_{ijk}^{abc}, \tag{1.56}$$

where $E_{\mathrm{c}}^{\mathrm{CCSD}}$ is retrieved by Eq. (1.41) and $\bar{t}_{abc}^{\,ijk}$ is defined as [12],

$$\bar{t}_{abc}^{\,ijk} = \frac{4}{3} t_{abc}^{ijk} - 2t_{acb}^{ijk} + \frac{2}{3} t_{bca}^{ijk}. \tag{1.57}$$

It is worth noting that the CCSD(T) approximation includes all triple excitation terms that appear in MP4 perturbation theory. Thus, CCSD and CCSD(T) incorporate the entire set of diagrams for the evaluation of the correlation energy that occurs in MP3 and MP4 perturbation theory, respectively, and even beyond that through the infinite resummation of terms at the CCSD level of theory.

Summarizing, coupled cluster theory, initially proposed by Coester and Kümmel in the field of nuclear physics [13], was introduced to the study of electron correlation in quantum chemistry by Čížek and Paldus in the 1960s [14]. Since then, it has evolved into a powerful, successful, and widely used electronic structure theory method for addressing correlation effects in many-electron systems.

In the following chapters, we will attempt to apply Hartree-Fock and post-Hartree-Fock theories to the Uniform Electron Gas model, detect shortcomings and limitations, provide a thorough analysis of the terms appearing in MP perturbation theory and coupled-cluster approximations, and offer a treatment for the caveats of divergent coupled-cluster methods.

Chapter 2

The Uniform Electron Gas: an intertemporal toy model

Instead of deriving sophisticated, approximate single-particle solutions of the original many-body problem, one might take a different tack by developing toy model Hamiltonians. Among these models is the Uniform Electron Gas (UEG), commonly referred to as the "Jellium" model, introduced in the early 1930s as an archetype by J. Bardeen for the qualitative study of metallic systems.[1]

Since then, the UEG has served as the workhorse model for extensive studies, both analytical and numerical. Notably, in 1965, Kohn and Sham [15] demonstrated that knowledge of an analytical parametrization of the UEG correlation energy enables approximate calculations for atoms, molecules and solids within the framework of DFT. Additionally, its correlated fermionic nature is intertwined to a plethora of physical phenomena, including Wigner crystallization, spin-polarization transitions, screening effects, the quasi-particle picture of collective excitations known as plasmons, and more.

In this chapter, we will provide a brief theoretical description of the UEG, along with the necessary modifications and procedural steps, required for generating numerical

[1] The term "Jellium" was coined by the American physicist C. Herring.

results, using a variety of theories and approximations. Furthermore, we will outline the computational limitations that need to be addressed in order to obtain qualitative results resembling the prototype.

2.1 Theoretical description of the model

The UEG serves as a simplification of the complex, real nature of a many-particle system, particularly of solids, offering an approximate study of their properties. The following assumptions are considered: initially, during the formation of the solid, there is complete detachment of the valence electrons from each atomic nucleus, while the remaining components remain bound to it, entirely unaffected by the presence of other atoms. Subsequently, the resulting positive ions are "mushed up" — hence the name Jellium — to form a continuous, homogeneous, and isotropic quantity of positive charge with a density of $+ne$. Having thus completely reshaped the crystalline characteristics of the solid, one can conclude that the Jellium model involves a system of N electrons with a density of $n = N/\Omega$, interacting not only among themselves through the Coulomb potential but also with the aforementioned static positive quantity, commonly referred to as the background. The presence of the latter ensures the electrical neutrality of the system, described by the Hamiltonian:

$$\hat{H} = -\frac{1}{2}\sum_{i=1}^{N}\nabla_i^2 + \frac{1}{2}\sum_{i\neq j}^{N}\frac{1}{|\mathbf{r}_i - \mathbf{r}_j|} - \sum_{i=1}^{N}\int d^3r' \frac{n}{|\mathbf{r}_i - \mathbf{r}'|} + \frac{1}{2}\int d^3r \int d^3r' \frac{n^2}{|\mathbf{r} - \mathbf{r}'|}. \quad (2.1)$$

In Eq. (2.1), the first term accounts for the kinetic energy of the electrons, while the second term, denoted as $\hat{H}_{el-el}$, represents their repulsion energy due to the electrostatic interaction among them. The third ($\hat{H}_{el-b}$) and fourth ($\hat{H}_{b-b}$) terms describe the energy arising from the interactions of electrons with the positively charged background and within the background itself, respectively.

Due to the long-range nature of the Coulomb interaction, each term describing the corresponding interactions diverges in the thermodynamic limit (TDL). The latter plays a fundamental role in the analytical description of many-body quantum systems, determining the properties of the bulk medium. Consequently, it is essential to consistently

consider the limit in which the system volume extends throughout space, i.e., $\Omega \to \infty$. Moreover, for well-defined physical properties, the number of particles in the system should also approach infinity, $N \to \infty$, so that the density remains constant. However, the electrical neutrality of the system requires that the sum of the terms in the Hamiltonian remains well-defined in the given limit. To ensure the correctness of the intermediate mathematical operations, we introduce a convergence-exponential term of the form [16]:

$$\frac{1}{|\mathbf{r}-\mathbf{r}'|} = \lim_{\mu\to 0} \frac{e^{-\mu|\mathbf{r}-\mathbf{r}'|}}{|\mathbf{r}-\mathbf{r}'|}, \tag{2.2}$$

which leads to the modification of the Coulomb potential into a Yukawa potential. The Fourier transform of the latter is given by,

$$\frac{e^{-\mu|\mathbf{r}|}}{|\mathbf{r}|} = \frac{1}{\Omega}\sum_{\mathbf{q}} e^{i\mathbf{q}\cdot\mathbf{r}} \frac{4\pi}{|\mathbf{q}|^2+\mu^2}. \tag{2.3}$$

Using the result from (2.3) each interaction term of the Hamiltonian (2.1) is expressed as:

$$\begin{aligned}\hat{H}_{b-b} &= \lim_{\mu\to 0}\Big[\frac{n^2}{2}\int d^3r \int d^3r' \,\frac{e^{-\mu|\mathbf{r}-\mathbf{r}'|}}{|\mathbf{r}-\mathbf{r}'|}\Big] = \lim_{\mu\to 0}\Big[\frac{n^2}{2}\int d^3r \int d^3\rho \,\frac{e^{-\mu\rho}}{\rho}\Big] \\ &= \lim_{\mu\to 0}\Big[\frac{n^2}{2}\Omega\frac{4\pi}{\mu^2}\Big] = \lim_{\mu\to 0}\Big[\frac{1}{2}\frac{N^2}{\Omega}\frac{4\pi}{\mu^2}\Big],\end{aligned}$$

$$\begin{aligned}\hat{H}_{el-b} &= \lim_{\mu\to 0}\Big[-n\sum_{i=1}^{N}\int d^3r' \,\frac{e^{-\mu|\mathbf{r}_i-\mathbf{r}'|}}{|\mathbf{r}_i-\mathbf{r}'|}\Big] = \lim_{\mu\to 0}\Big[-n\sum_{i=1}^{N}\int d^3\rho \,\frac{e^{-\mu\rho}}{\rho}\Big] \\ &= \lim_{\mu\to 0}\Big[-\frac{N^2}{\Omega}\frac{4\pi}{\mu^2}\Big],\end{aligned}$$

$$\begin{aligned}\hat{H}_{el-el} &= \lim_{\mu\to 0}\Big[\frac{1}{2}\sum_{i\neq j}^{N}\frac{e^{-\mu|\mathbf{r}_i-\mathbf{r}_j|}}{|\mathbf{r}_i-\mathbf{r}_j|}\Big] = \lim_{\mu\to 0}\Big[\frac{1}{2}\frac{4\pi}{\Omega}\sum_{i\neq j}^{N}\sum_{\mathbf{q}}\frac{e^{i\mathbf{q}\cdot(\mathbf{r}_i-\mathbf{r}_j)}}{|\mathbf{q}|^2+\mu^2}\Big] \\ &= \frac{1}{2}\sum_{i\neq j}^{N}\frac{1}{\Omega}\sum_{\mathbf{q}\neq 0}\Big(\frac{4\pi}{|\mathbf{q}|^2}\Big)e^{i\mathbf{q}\cdot(\mathbf{r}_i-\mathbf{r}_j)} + \lim_{\mu\to 0}\Big[\frac{1}{2}\frac{N(N-1)}{\Omega}\frac{4\pi}{\mu^2}\Big].\end{aligned}$$

The two resulting terms in the electrostatic interaction between the electrons arise by separating the $\mathbf{q}=0$ component from the $\mathbf{q}$-sum. The first term is associated with

fluctuations in charge density due to the Coulomb interaction. Meanwhile, the second term, corresponding to the zero value of the wave vector $\mathbf{q}$, pertains to the static and uniform distribution of the electronic charge density in space. In the thermodynamic limit, where $N \gg 1$, it can be inferred for the second term that:

$$\frac{1}{2}\frac{N(N-1)}{\Omega}\frac{4\pi}{\mu^2} \approx \frac{1}{2}\frac{N^2}{\Omega}\frac{4\pi}{\mu^2}. \tag{2.4}$$

Summarizing the results of the electrostatic energies in conjunction with Eq. (2.4), we arrive at the cancellation of the three terms that diverge as μ^{-2}, an outcome that reflects the electrical neutrality of the system. As a consequence, we end up with a degenerate system of interacting particles that obey the Fermi-Dirac statistics, as the only non-zero terms in the Hamiltonian (2.1), in the thermodynamic limit, are the kinetic energy of electrons and their electrostatic interaction, corresponding to the term with $\mathbf{q} \neq 0$, namely,

$$\hat{H} = -\frac{1}{2}\sum_{i=1}^{N}\nabla_i^2 + \frac{1}{2}\sum_{i\neq j}^{N} v(\mathbf{r}_i - \mathbf{r}_j), \tag{2.5}$$

where taking the Fourier transform of $v(\mathbf{r}_i - \mathbf{r}_j)$, we have, by definition, that:

$$v(\mathbf{q}) = \begin{cases} \dfrac{4\pi}{|\mathbf{q}|^2}, & \text{if} \quad \mathbf{q} \neq 0 \\ 0, & \text{if} \quad \mathbf{q} = 0. \end{cases} \tag{2.6}$$

The repulsive Coulomb interaction, and consequently, the correlated motion of the electrons, lead to a decrease in the energy of the system. In turn, the kinetic energy increases to maintain the total energy of the system constant. This interplay between the two terms of Eq. (2.5) gives rise to interesting physical phenomena, and can be qualitatively represented by a single parameter.

Let us assume that each electron occupies an average volume r_s^3. Following the uncertainty principle, the minimum kinetic energy per particle will be of order $\mathcal{O}(1/r_s^2)$ [17]. In contrast, the Coulomb energy is of order $\mathcal{O}(1/r_s)$, assuming that each particle interacts predominantly only with its nearest neighbors. The ratio of the two energy scales

defines the density parameter r_s. Physically, r_s is the radius of the spherical volume containing one electron on average. We have thus identified the electron average distance and, therefore, the electron density as the relevant parameter controlling the relative strength of electron–electron interactions.

Supplementarily, it is essential and advisable to change the notation of Eq. (2.5) into second quantization form,

$$\hat{H} = \frac{1}{r_s^2}\sum_{\mathbf{k},\sigma}\epsilon_{\mathbf{k}}\alpha^{\dagger}_{\mathbf{k}\sigma}\alpha_{\mathbf{k}\sigma} + \frac{1}{2r_s\Omega}\sum_{\mathbf{k},\mathbf{k}'}\sum_{\mathbf{q}\neq 0}\sum_{\sigma,\sigma'} v(\mathbf{q})\alpha^{\dagger}_{\mathbf{k}+\mathbf{q},\sigma}\alpha^{\dagger}_{\mathbf{k}'-\mathbf{q},\sigma'}\alpha_{\mathbf{k}',\sigma'}\alpha_{\mathbf{k},\sigma}, \tag{2.7}$$

as it significantly facilitates theoretical applications to the many-body problem. Here, $\alpha^{\dagger}_{\mathbf{k}\sigma}$, $\alpha_{\mathbf{k}\sigma}$ are the usual fermionic creation and annihilation operators that create, destroy a particle on a state $|\mathbf{k}\rangle$ with spin σ, respectively.

As seen from Eq. (2.7), neglecting the electron-electron interaction would be justifiable in the limit of high density, corresponding to $r_s \ll 1$. However, this assumption doesn't hold in conventional metals where r_s is typically of order $\mathcal{O}(1)$, and therefore potential and kinetic energy are of the same order. Hence, one needs to address the full complexity of the Hamiltonian (2.7).

2.2 The computational approach

For numerical calculations, the finite-size uniform electron gas is considered, since the limited computational memory and power allow us to perform calculations for electrons of the order $\mathcal{O}(10^2 - 10^3)$. The N-electron UEG is confined in a simulation-cell with a Hamiltonian that reads:

$$\hat{H} = -\frac{1}{2}\sum_{i=1}^{N}\nabla_i^2 + \frac{1}{2}\sum_{i\neq j}^{N}\hat{v}_{ij} + \frac{1}{2}v_M, \tag{2.8}$$

where i,j are electron indices, v_M is the Madelung constant and the two-electron interaction is given by,

$$\hat{v}_{ij} = \frac{1}{\Omega}\sum_{\mathbf{G}}\frac{4\pi}{\mathbf{G}^2}e^{i\mathbf{G}\cdot(\mathbf{r}_i-\mathbf{r}_j)}, \tag{2.9}$$

with Ω referring to the volume of the real-space simulation cell. The calculations can be carried out, employing a simple cubic (sc), body-centered cubic (bcc) or a face-centered cubic (fcc) reciprocal-space unit cell. The corresponding reciprocal lattice vectors $\mathbf{G}$ are defind as:

$$\mathbf{G} = \frac{2\pi}{L} \begin{pmatrix} l \\ m \\ n \end{pmatrix}, \tag{2.10}$$

where l, m and n are integer numbers and L is the real-space box length such that $L^3 = \Omega$. Since our goal is to obtain results that could resemble the bulk medium, we have to increase the volume of the simulation cell. In parallel, the number of electrons should be increased with the same rate as Ω, so that the density of the particles remains constant. To achieve that, we note the relation between r_s, N, and Ω:

$$\Omega = \frac{4\pi}{3} r_s^3 N. \tag{2.11}$$

Returning to Eq. (2.8), the Madelung constant, v_M, stands for the uniform distribution of the electron charge density in space, specifically the $\mathbf{q} = 0$ component in the $\mathbf{q}$-sum. Since we are still far from reaching the TDL, this term-linear to N in Eq. (2.4)-cannot be neglected, as discussed earlier. This feature emerges from the finite size of our simulation cell and vanishes as we approach the TDL. It is noted that v_M is uniquely defined for a system of N electrons in a volume Ω. Subsequently, for the finite-size UEG we can write:

$$v(\mathbf{G}) = \begin{cases} \dfrac{4\pi}{|\mathbf{G}|^2}, & \text{if} \quad \mathbf{G} \neq 0 \\ v_M, & \text{if} \quad \mathbf{G} = 0. \end{cases} \tag{2.12}$$

In our calculations, we will systematically increase the size of our simulation box, by increasing the number of electrons, to approach the TDL. As we are dealing with a supercell, there is only one k-point in the $1st$ B.Z. in reciprocal space, specifically the $k = 0$ point. This calculation procedure is commonly referred to as the Γ-point calculation.

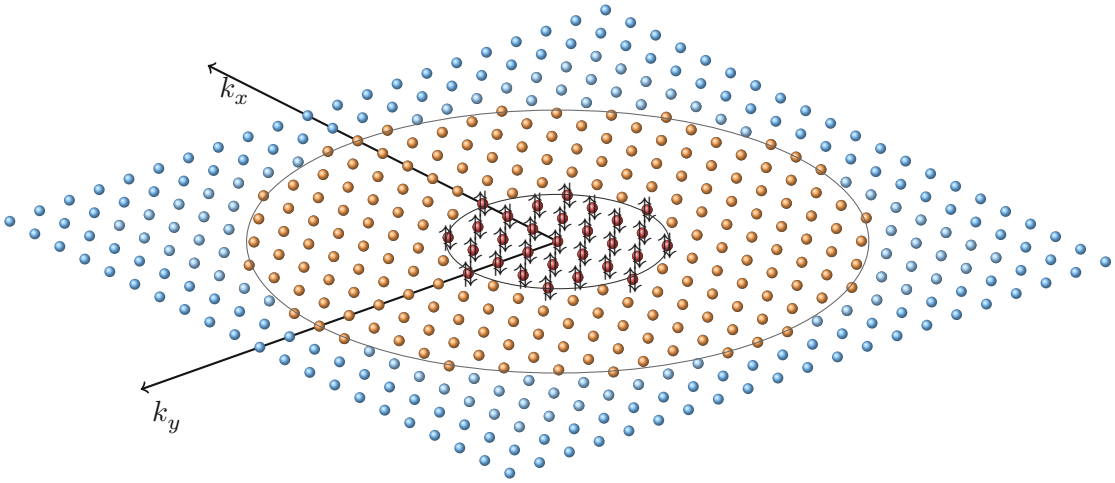

Figure 2.1: *2D schematic illustration of the reciprocal grid employed for computational calculations. The red points indicate states occupied by electrons, while the yellow points represent unoccupied or virtual states. The cyan points denote the set of augmented virtual states. The inner circle designates the Fermi "surface", and the outer one marks the kinetic energy cutoff.*

In the current thesis, we will restrict ourselves to the paramagnetic UEG. In this scenario, each quantized reciprocal lattice vector, as expressed in Eq. (2.10), is occupied by two electrons with opposite spins. Furthermore, the symmetry of the reciprocal unit cell can determine closed-shell configurations, resulting in specific "magic numbers". For instance, in the sc lattice we come across closed-shell electron configurations with sets of 2, 14, 38, 54, 66, 114, and so on. Due to the finiteness of the number of electrons, the occupied states delineate a polyhedron in reciprocal space. In the TDL, as the states become denser, they will tend towards the well-known Fermi sphere.

In relation to unoccupied or virtual states, their number, for our computational requirements, is determined by a kinetic energy cutoff of the form $E_{\text{cut}} = k_{\text{cut}}^2/2$, where k_{cut} is the cutoff momentum. The manifold beyond this cutoff comprises the augmented virtual states, representing an infinite number of states with momenta exceeding k_{cut}

in magnitude. Their significance will be discussed later in this chapter. Fig. (2.1) provides an illustration of the aforementioned discussion.

2.3 Hartree-Fock insights into the UEG

The purpose of this section is to apply the Hartree-Fock method to approximately calculate the ground-state energy of the UEG described by the Hamiltonian (2.7) and discuss some important features. An intrinsic property of a homogeneous system, such as the Jellium model, is the invariance of its physical quantities under spatial translations. This symmetry, in combination with the imposition of periodic boundary conditions (Born-von Karman conditions) on the one-body wave functions of the system, allows for the study in the plane wave basis set, with corresponding normalized wave functions:

$$\psi_{\mathbf{k}_p}(\mathbf{r}) = \frac{1}{\sqrt{\Omega}} e^{i\mathbf{k}_p\cdot\mathbf{r}}. \tag{2.13}$$

It can be easily demonstrated for the given system that each family of N plane waves, in the aforementioned form, comprises a solution to Eq. (1.10), with corresponding eigenvalues:

$$\mathcal{E}_{k_p} = \frac{k_p^2}{2} - \frac{1}{\Omega}\sum_{\substack{k_r\leq k_F \\ r\neq p}} v(k_p - k_r) = \frac{k_p^2}{2} - \frac{1}{\Omega}\sum_{\substack{k_r\leq k_F \\ r\neq p}} \frac{4\pi}{|k_p - k_r|^2}, \tag{2.14}$$

In the thermodynamic limit, the discrete set of $|k\rangle$ states is transformed into a continuum, leading to an analytic calculation for the dispersion relation in Eq. (2.14), which reads,

$$\mathcal{E}_{k_p} = \frac{k_p^2}{2} - \frac{2k_F}{\pi} F\Big(\frac{k_p}{k_F}\Big), \tag{2.15}$$

where

$$F(x) = \frac{1}{2} + \frac{1-x^2}{4x}\ln\Big|\frac{1+x}{1-x}\Big|, \quad x = k_p/k_F, \tag{2.16}$$

is a monotonically non-increasing function of x with values $F(0) = 1$ and $F(1) = 1/2$. Additionally, the Fermi wavevector is given by,

$$k_F = \frac{1}{0.521 r_s}. \tag{2.17}$$

From Eq. (2.15) we observe that the energy dispersion for single-electron states in the Hartree-Fock approximation is significantly modified compared to the free electron energy, as outlined in Fig. 2.2(a). Specifically, the occupied bandwidth, i.e. the spread between the minimum and maximum energies in the dispersion relation, increases. This characteristic is attributed to the influence of the exchange term within the Hartree-Fock approximation. As k varies from 0 to k_F the lowest eigenvalues ϵ_p, extend by $2k_F/\pi$, while its highest reach is reduced by $k_F/2 - k_F/\pi$. Moreover, it is noteworthy to mention that the bandwidth is proportional to the density of the system under study. In particular, the lower the density, the larger the bandwidth, affecting both the lower and upper bounds of the energy spectrum.

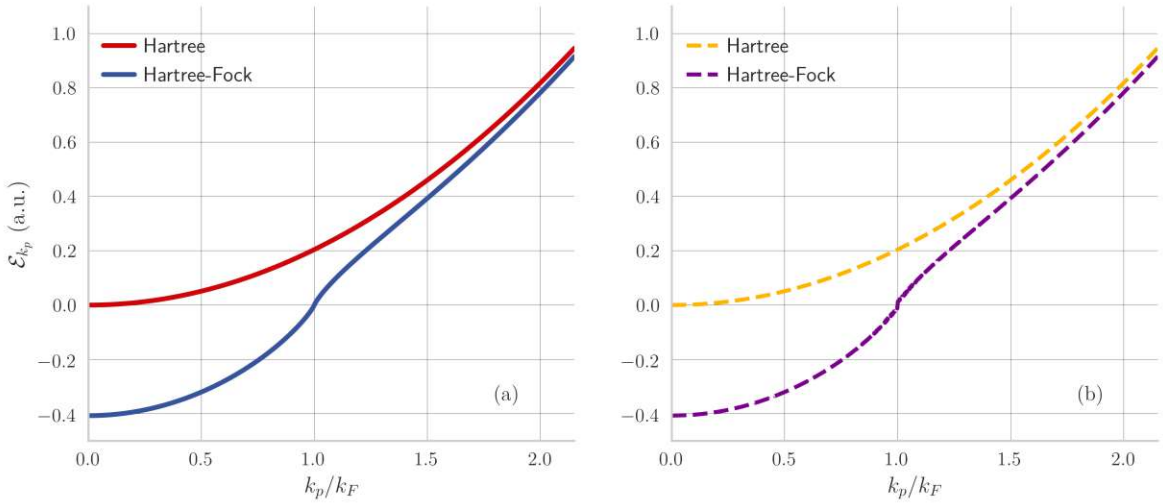

Figure 2.2: *(a) Analytical results for the energy dispersion of single-electron states in the UEG within the Hartree-Fock approximation are compared to the free electron gas. (b) Computational results are presented for a system using 20.502 electrons and 102.831 plane waves. Both sets of results were obtained at a density parameter of* $r_s = 3\,(a.u.)$.

Returning to Eq. (2.14), the singularity that arises for $k_p = k_r$ is integrable in the TDL. While we can overcome this singularity analytically, computationally, it is denoted in the occupied states given by Eq. (2.18), through the Madelung constant υ_M, and is

strongly related to the system size. Implementation details for this technique can be found in Ref. [18]. Illustratively, we mention that for 20.502 and 99.114 electrons at a density parameter of $r_s = 3$ a.u. the corresponding Madelung constants are 0.0214 and 0.0127, indicating the slow convergence towards zero [19].

Utilizing Eq. (2.18) and (2.19), we observe in Fig. 2.2(b) that we obtain identical results to the analytical ones depicted in Fig. 2.2(a). The Hartree-Fock eigenvalues for occupied and virtual states are given by,

$$\mathcal{E}_{k_p} = \frac{k_p^2}{2} - \frac{1}{\Omega} \sum_{\substack{k_r < k_F \\ r \neq p}} v(k_p - k_r) - v_M, \quad k_p \leq k_F, \tag{2.18}$$

$$\mathcal{E}_{k_p} = \frac{k_p^2}{2} - \frac{1}{\Omega} \sum_{k_r < k_F} v(k_p - k_r), \quad k_p > k_F, \tag{2.19}$$

respectively. From Eq. (2.15), we can easily calculate the ground state energy per electron of the UEG within the Hartree-Fock approximation, which is:

$$\frac{E}{N} = \left(\frac{1.105}{r_s^2} - \frac{0.458}{r_s} \right) \text{a.u.} . \tag{2.20}$$

As we observe, the second term in Eq. (2.20) is negative, which contradicts the classical expectation of a positive electrostatic interaction between electrons, as depicted in Eq. (2.5). This paradox is a consequence of a purely quantum phenomenon, specifically concerning electrons with identical spin. The correlated motions, imposed by Pauli's exclusion principle, overcome the electrostatic interaction, reducing the energy and ultimately forming a stable system. Moreover, the exchange term is comparable to the kinetic one, for conventional metals, where r_s is typically of the order $\mathcal{O}(1)$, indicating that the exchange interactions cannot be overlooked in estimating the electronic energy of such systems.

Furthermore, the slope of the $F(x)$ function in Eq. (2.15) diverges logarithmically at the Fermi surface ($k = k_F$). As a consequence, every physical quantity linked to the Hartree-Fock eigenenergies appears problematic. These results are attributed not only to the long-range nature of the Coulomb interaction but also to the fact that Hartree-Fock is a mean-field theory — each electron is subjected to the mean-field created by

all other electrons. Thus, one should take into account the electronic correlations by incorporating the fields of electrons other than the two at positions $\mathbf{r}$ and $\mathbf{r}'$. To this end, post-Hartree-Fock methods can be employed to obtain meaningful results and improve their accuracy.

2.4 Beyond the Hartree-Fock approximation: MP2 theory.

The MP2 theory constitutes the second step following a Hartree-Fock calculation, providing access to the correlation effects of a physical system. Furthermore, in the specific case of metallic systems, it serves as a prototype for divergent theories, contributing to our understanding of the reasons behind the failure at every level of perturbation theory in such systems. Recapitulating the energy expressions from the theory section [Eq. (1.19)] we have [20]:

$$E_c^{\mathrm{MP2}} = \sum_{ij}^{\mathrm{occ.}} \sum_{ab}^{\mathrm{vir.}} \left[\underbrace{\frac{2\,\langle ij|ab\rangle\,\langle ab|ij\rangle}{\epsilon_i + \epsilon_j - \epsilon_a - \epsilon_b}}_{\text{direct}} - \underbrace{\frac{\langle ij|ab\rangle\,\langle ba|ij\rangle}{\epsilon_i + \epsilon_j - \epsilon_a - \epsilon_b}}_{\text{exchange}} \right], \tag{2.21}$$

where the algebraic expressions of the so-called direct and exchange terms in Eq. (2.21) can be represented diagrammatically by the following Goldstone diagrams:

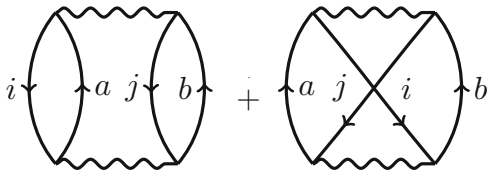

For the case of the UEG, the single-particle states are plane waves, characterized by wave vectors $\mathbf{k}$. Thus, we can change our notation by substituting the occupied states i and j with the plane wave states $\mathbf{k}_i$ and $\mathbf{k}_j$, both located within the Fermi sphere. Additionally, by setting $\mathbf{q} = \mathbf{k}_a - \mathbf{k}_i$, the virtual or unoccupied states a and b are replaced by the plane wave states $\mathbf{k}_i + \mathbf{q}$ and $\mathbf{k}_j - \mathbf{q}$, respectively, lying outside the

Fermi sphere. In the TDL, utilizing Hartree eigenenergies, the two terms of Eq. (2.21) take the form [21]:

$$E_c^{\mathrm{dMP2}} = -\frac{3N}{16\pi^5}\int d^3q \int d^3k_i \int d^3k_j \frac{\alpha(\mathbf{k}_i,\mathbf{k}_j,\mathbf{q})}{q^4\, D(\mathbf{k}_i,\mathbf{k}_j,\mathbf{q})}, \tag{2.22}$$

$$E_c^{\mathrm{xMP2}} = \frac{3N}{32\pi^5}\int d^3q \int d^3k_i \int d^3k_j \frac{\alpha(\mathbf{k}_i,\mathbf{k}_j,\mathbf{q})}{q^2\,(\mathbf{k}_i+\mathbf{q}-\mathbf{k}_j)^2\, D(\mathbf{k}_i,\mathbf{k}_j,\mathbf{q})}, \tag{2.23}$$

where we defined the corresponding matrix elements as,

$$\langle ab|ij\rangle = v_{ij}^{ab} = v(\mathbf{q})\delta_{\mathbf{k}_a-\mathbf{k}_i,\mathbf{k}_j-\mathbf{k}_b}, \tag{2.24}$$

$$\langle ba|ij\rangle = v_{ij}^{ba} = v(\mathbf{k}_j-\mathbf{k}_a) = v(\mathbf{k}_j-\mathbf{k}_i-\mathbf{q})\delta_{\mathbf{k}_j-\mathbf{k}_a,\mathbf{k}_b-\mathbf{k}_i}. \tag{2.25}$$

Moreover, the momenta are expressed in terms of the Fermi wavevector and $\alpha(\mathbf{k}_i,\mathbf{k}_j,\mathbf{q})$ is given by,

$$\alpha(\mathbf{k}_i,\mathbf{k}_j,\mathbf{q}) = \theta(\mathbf{k}_i)\theta(\mathbf{k}_j)[1-\theta(\mathbf{k}_i+\mathbf{q})][1-\theta(\mathbf{k}_j-\mathbf{q})], \tag{2.26}$$

where $\theta(x)$s are the unit step functions defining the integration regions. As observed, the major contribution of the integrands in Eq. (2.22) and (2.23) can be found at small $\mathbf{q}$ values, also known as long-range or long wavelength limit. Consequently, for the energy denominator $D(\mathbf{k}_i,\mathbf{k}_j,\mathbf{q})$, it can easily be shown that the leading term at this limit is linear to q, namely,

$$D(\mathbf{k}_i,\mathbf{k}_j,\mathbf{q}) = \mathbf{q}\cdot(\mathbf{q}+\mathbf{k}_i-\mathbf{k}_j) \underset{q\to 0}{\overset{\lim}{\approx}} \mathbf{q}\cdot(\mathbf{k}_i-\mathbf{k}_j). \tag{2.27}$$

Due to the limits of the integration regions, $\mathbf{k}_i$ and $\mathbf{k}_j$ lie in opposite hemispheres, as dictated by momentum conservation, and within a spherical shell of thickness proportional to q around the Fermi surface. Therefore, by substituting Eq. (2.27) into Eq. (2.22), the volume integration over the two shells containing the mentioned occupied states will contribute a factor q^2. The latter, in combination with the additional q^2 term arising from the volume element of the $\mathbf{q}$ integration, cancels the two singular Coulomb terms, each scaling as q^{-2}. Eventually, the integration of the remaining q^{-1} term in Eq. (2.22) results in a logarithmic divergence, also known as the *infrared catastrophe*, of the corresponding correlation energy.

In relation to Eq. (2.23), the difference between the exchange and direct terms is found in the Coulomb matrix elements. More specifically, the singularity that appears in Eq. (2.25) at $\mathbf{q} = \mathbf{k}_j - \mathbf{k}_i$ is integrable [22]. At the long wavelength limit, the integrand behaves proportionally to q, yielding a convergent correlation energy for the exchange term.

In the case of Hartree-Fock eigenenergies given by Eq. (2.15), the energy denominator $D(\mathbf{k}_i, \mathbf{k}_j, \mathbf{q})$ is modified as:[2]

$$D(\mathbf{k}_i, \mathbf{k}_j, \mathbf{q}) \approx \mathbf{q} \cdot (\mathbf{k}_j - \mathbf{k}_i) \ln q + \mathcal{O}(q) + \mathcal{O}(q^2) \underset{q \to 0}{\overset{\lim}{\approx}} \mathbf{q} \cdot (\mathbf{k}_j - \mathbf{k}_i) \ln q. \tag{2.28}$$

Following the same argumentation as before and substituting Eq. (2.28) into Eq. (2.22) and (2.23), it can be shown that the two integrands take the form $(q \ln q)^{-1}$ and $q/\ln q$, respectively. Consequently, the correlation energy diverges as $\ln(\ln q)$ for the direct term at the long-range limit, while the exchange term, similar to the Hartree case, leads to a convergent result. We observe that, while the presence of a larger bandwidth in the Hartree-Fock eigenenergies leads to a "shifted" energy denominator, it doesn't cancel out the divergence of the direct term, but rather, it merely weakens it.

At the other end of the spectrum lies the short-range or short wavelength limit, represented by large $\mathbf{q}$ values. In both Hartree and Hartree-Fock eigenenergies, the integrands in Eq. (2.22) and (2.23) scale as q^{-4}, respectively. The significance of this behavior will be discussed later in this chapter.

To numerically observe the analytical behaviors of the integrands and correlation energies discussed earlier, we utilize the finite UEG system introduced in Section (2.2). For meaningful results, it is customary to start with a finite electron number and then carefully approach the thermodynamic limit. The latter ensures control over the grid spacing of the allowed wavevectors, which is essential to our goal of obtaining a denser grid in the region around the Fermi surface. The emerged infinitesimal spacing gives rise to the small $\mathbf{q}$ values that cause the limiting behaviors at the long wavelength limit.

[2] To avoid presenting a tedious mathematical analysis, we urge the reader to consult reference [23].

Additionally, as pointed out earlier, the number of virtual or unoccupied states is determined by a kinetic energy cutoff. The finite basis set, comprised of plane-waves in this case, stretches out into k-space around the Γ-point, as illustrated in Fig. (2.1). To ensure the intrinsic accuracy of the basis set completeness and to better capture the short wavelength limit, we systematically increase the cutoff until consistent and convergent results are achieved.

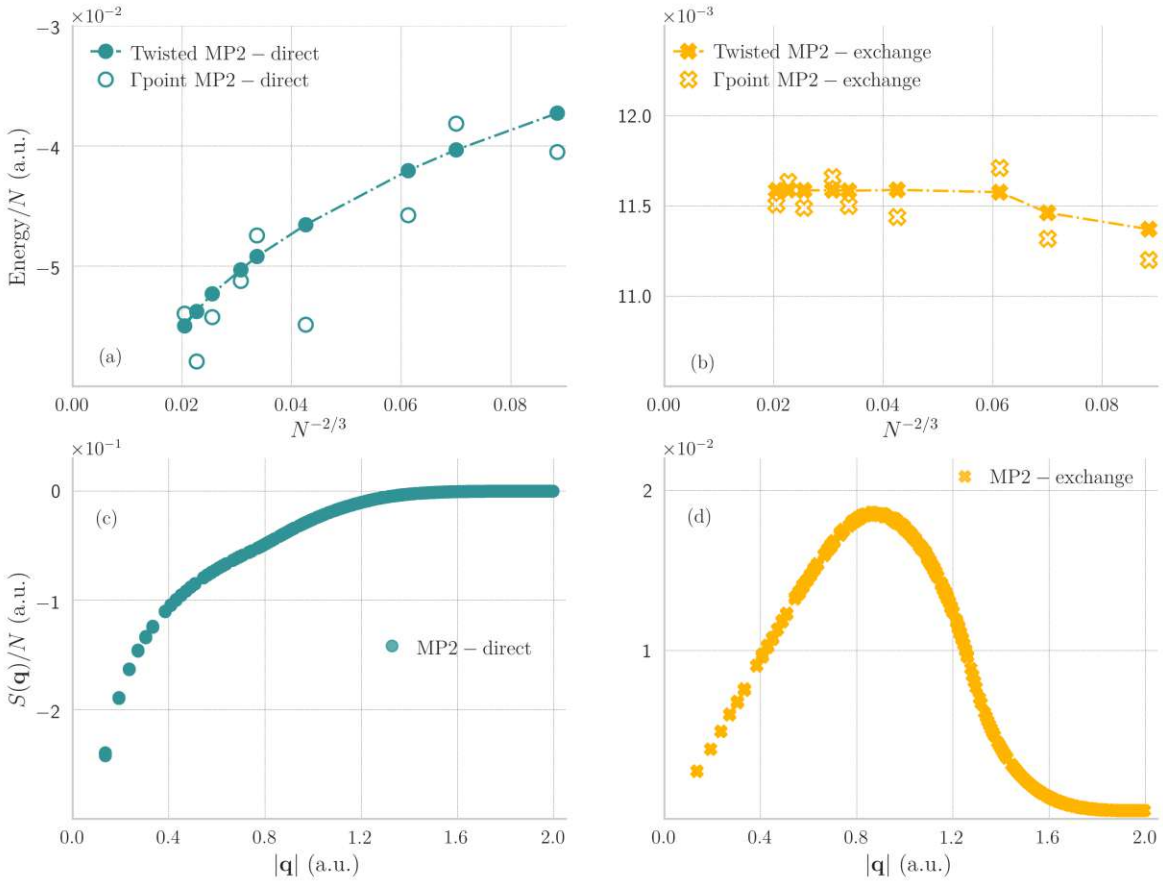

Figure 2.3: *(a)-(b) MP2 direct and exchange correlation energies retrieved as $N^{-2/3}$ for a set of electrons. Twist-averaged and Γpoint calculations are presented. (c)-(d) Twist-averaged direct and exchange MP2 transition structure factors.*

Fig. (2.3) presents results for sets of finite-N electron systems with finite-M plane waves constructed in this manner. Specifically, calculations for direct and exchange MP2 correlation energies were performed for closed shell configurations involving 38, 54, 66, 114, 162, 188, 246, 294, and 342 electrons. Meanwhile, the virtual states manifold consisted of 15-20 plane waves per occupied orbital, at a density of $r_s = 3$ a.u. The results are shown in Fig. (2.3) (a) and (b). Moreover, at the same density, the evaluated function resulting from the volume integrations over the states $\mathbf{k}_i$ and $\mathbf{k}_j$ is depicted in Fig. (2.3) (c) and (d) for 874 electrons and nearly 4.800 plane waves.[3] This conclusively demonstrates that this approach successfully captures the expected divergence and convergence of the direct and exchange terms, while the corresponding numerical behaviors can serve as a guide for other divergent or convergent post-Hartree-Fock theories.

2.5 Coupled-cluster doubles applied to the UEG

Since its introduction for the study of nuclear physics phenomena and later for electron correlations in atoms and molecules, coupled-cluster theory has successfully gained a foothold in solid-state physics. Beyond doubt, CC theories can capture electronic correlation effects to a greater extent compared to MBPT, as they include, by construction, an infinite resummation of perturbative terms. Furthermore, the accuracy of the employed CC theory goes hand in hand, not only with the level of the imposed truncation, but also by the specific system under study. For example, coupled-cluster with singles and doubles excitations (CCSD), which is the lowest in the hierarchy of CC theories applicable to extended systems, and CCSD(T), can be adequately applied to semiconductors and insulators, accurately predicting their properties, such as cohesive energies, lattice constants, bulk moduli, band structures, band gaps, and phase transition diagrams [24, 25, 26, 27, 28, 29]. However, they fall short in metallic systems;

[3] Later, we will associate the evaluated function with the concept of the *transition* structure factor and discuss its importance.

CCSD calculations can differ significantly from experimental findings, and CCSD(T) is inapplicable due to an infrared catastrophe similar to MP2 theory [11].

As we seek to have a deeper understanding of the different levels within CC theory, our goal is to develop sophisticated numerical approaches and avoid unnecessary efforts in approximations or methods that may prove insufficient. To that end, we present the key concepts of CC theories, particularly CCSD theory, where else but on the UEG.

Initially, due to the model's symmetry and the imposition of a specific momentum originating from the $\hat{T}_2$ contributions to $\hat{T}_1$ equations, single excitations are absent. This absence leads to the equivalence of coupled cluster singles and doubles (CCSD) with coupled cluster doubles (CCD) in the UEG. Specifically, employing a Hartree-Fock reference and given that the plane-waves are eigenstates of the Fock operator, thereby orthogonal, the overlap between the occupied and virtual manifold is zero.[4] Recalling the single excitation CCSD equations from Eq. (1.42), we find that the off-diagonal parts f_i^a are zero. Consequently, the first approximation in computing the t_i^a as:

$$t_i^{a\ (1)} = \frac{f_i^a}{\epsilon_i - \epsilon_a}, \tag{2.29}$$

results in zero. This, in turn, deductively leads to the vanishing of the $\hat{T}_1$ contributions to the CCSD $\hat{T}_2$ equations.

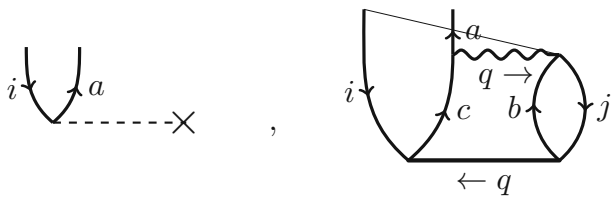

Figure 2.4: *f_i^a and $t_{ij}^{cb} v_{cb}^{aj}$ contributions from the CCSD $\hat{T}_1$ equations.*

In return, $\hat{T}_2$ contributions carry a q momentum transfer, defined as $\mathbf{q} = \mathbf{k}_j - \mathbf{k}_b$. Applied to the second diagram in Fig. (2.4), by momentum conservation assertions, we

[4] This conclusion can also be drawn by applying Brillouin's theorem.

arrive at the conclusion that a, a virtual orbital, must be equal to the occupied orbital i, resulting in a proof of contradiction since we are calculating the coefficients t_i^a of single-particle excitations. Evidently, the $\hat{T}_2$ contributions to CCSD $\hat{T}_1$ equations will also vanish, leading to the absence of single excitations in CCSD theory. Therefore, the doubles amplitude equation (1.43) is reduced to:

$$\begin{aligned}
\underbrace{(\epsilon_i + \epsilon_j - \epsilon_a - \epsilon_b)}_{\Delta_{ij}^{ab}} t_{ij}^{ab} = \overbrace{\underbrace{v_{ij}^{ab}}_{\text{MP2}} + \underbrace{2v_{ic}^{ak} t_{kj}^{cb} + 2t_{ik}^{ac} v_{cj}^{kb}}_{\text{linear rings}} + \underbrace{P\, 2t_{ik}^{ac} v_{cd}^{kl} t_{lj}^{db}}_{\text{quadratic ring}}}^{\text{rCCD}} - \underbrace{P\, v_{ic}^{ak} t_{kj}^{bc}}_{\text{crossed-ring}} \\
+ \overbrace{\underbrace{v_{cd}^{ab} t_{ij}^{cd}}_{\text{pp-ladder}} + \underbrace{v_{ij}^{kl} t_{kl}^{ab}}_{\text{hh-ladder}} - \underbrace{P\,(t_{ik}^{cb} v_{cj}^{ak} + t_{ik}^{ac} v_{cj}^{bk})}_{\text{ph-ladders}}}^{\text{ladders}} \\
- \underbrace{P\, t_{ij}^{cb} w_{dc}^{lk} t_{lk}^{da}}_{\lambda_{ik}} + \underbrace{P\, t_{kj}^{ab} w_{dc}^{lk} t_{li}^{dc}}_{\lambda_{ac}} - \underbrace{P\, t_{il}^{ac} v_{cd}^{kl} t_{kj}^{db}}_{\text{Q1}} \\
- \underbrace{P\, t_{il}^{da} v_{dc}^{lk} t_{kj}^{cb}}_{\text{Q2}} + \underbrace{P\, \frac{1}{2}\, t_{il}^{db} v_{cd}^{lk} t_{kj}^{ac}}_{\text{Q3}} \\
- \underbrace{P\, \frac{1}{2}\, t_{il}^{ad} w_{dc}^{lk} t_{kj}^{bc}}_{\text{Q4}} + \underbrace{P\, \frac{1}{2}\, t_{il}^{da} v_{dc}^{lk} t_{kj}^{bc}}_{\text{Q5}} \\
+ \underbrace{P\, \frac{1}{2}\, t_{il}^{da} v_{cd}^{lk} t_{kj}^{cb}}_{\text{Q6}} + \underbrace{t_{kl}^{ab} v_{cd}^{kl} t_{ij}^{cd}}_{\text{Q7}},
\end{aligned} \tag{2.30}$$

where $P\{\dots\}_{ij}^{ab} = \{\dots\}_{ij}^{ab} + \{\dots\}_{ji}^{ba}$, and $w_{ij}^{ab} = 2\langle ab|ij\rangle - \langle ab|ji\rangle$ are the two-electron Coulomb integrals given by Eq. (2.25). The amplitudes t_{ij}^{ab} are obtained by iteratively solving the CCD amplitude equation in Eq. (2.30). The convergence of the latter is facilitated by employing the direct inversion of the iterative subspace (DIIS) [30]. Furthermore, owing to momentum symmetry, amplitude storage is reduced by a factor of M, where M represents the number of plane waves. The computational cost scales as $\mathcal{O}(M^4)$, primarily due to the most expensive term, which is the particle-particle ladder. After retrieving the converged t_{ij}^{ab} amplitudes, the correlation energy is calculated by the expression:

$$E_c^{\text{CCD}} = \sum_{ijab} v_{ab}^{ij} (2t_{ij}^{ab} - t_{ji}^{ab}), \tag{2.31}$$

which is diagrammatically depicted as,

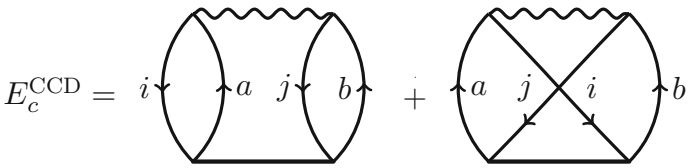

It is important to note that in the UEG t_{ij}^{ab} inherits the momentum conservation, similar to the Coulomb matrix elements in Eq. (2.25), and we can write:

$$t_{ij}(\mathbf{q}) = t_{ij}^{ab}\delta_{\mathbf{q},\mathbf{k}_j-\mathbf{k}_b}\delta_{\mathbf{q},\mathbf{k}_a-\mathbf{k}_i}. \tag{2.32}$$

Moreover, we define the quantity $S(\mathbf{q})$, known as the *transition* structure factor [31],[5] which offers insight into the dependence of the correlation energy on the interelectronic interaction distance. The transition structure factor is computed using the converged t_{ij}^{ab} amplitudes, and its definition is given by:

$$S^{\mathrm{CCD}}(\mathbf{q}) = \sum_{ijab} \frac{\delta v_{ij}^{ab}}{\delta v(\mathbf{q})} \left(2t_{ij}^{ab} - t_{ji}^{ab}\right), \tag{2.33}$$

which is diagrammatically illustrated as,

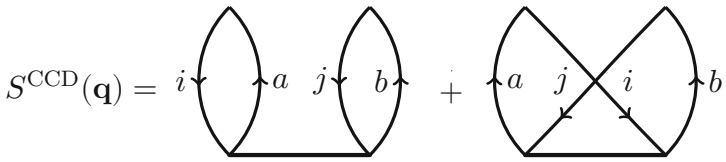

Numerical studies of the transition structure factor in both the long and short wavelength limits can provide valuable insights into the behavior and characteristics of the theory under consideration. For instance, they can indicate whether the employed theory diverges or converges in the long wavelength limit and how it behaves based on the studied system.

[5]The term *transition* reflects the procedures of truncating the employed theory and projecting the Hamiltonian onto the Hilbert space of doubly excited determinants. It is not correlated with the electronic structure factor, which is the Fourier transform of the pair correlation function (see Appendix A). To obtain the electronic structure factor in the coupled-cluster regime, one has to employ Λ-CC theory.

Conversely, such studies can also offer valuable information about the scaling of various theories in the short-range limit. For example, Fig. (2.3) (c)-(d) show the divergence and convergence of the transition structure factors corresponding to direct and exchange MP2 terms. In this case, the transition structure factor aligns with the limiting behaviors of the integrands, excluding the Coulomb potential, in Eq. (2.22) and Eq. (2.23) after integrating over states $\mathbf{k}_i$ and $\mathbf{k}_j$.

With the converged t_{ij}^{ab} amplitudes, one can also conduct a diagrammatic decomposition of each individual term appearing in the doubles amplitude equation. This allows for the examination of each term, leading to valuable conclusions about their behaviors in both the long and short wavelength limits.

In Fig. (2.5), we present a flowchart depicting the procedure followed to recursively solve the CCD amplitude equation and obtain the converged amplitudes.

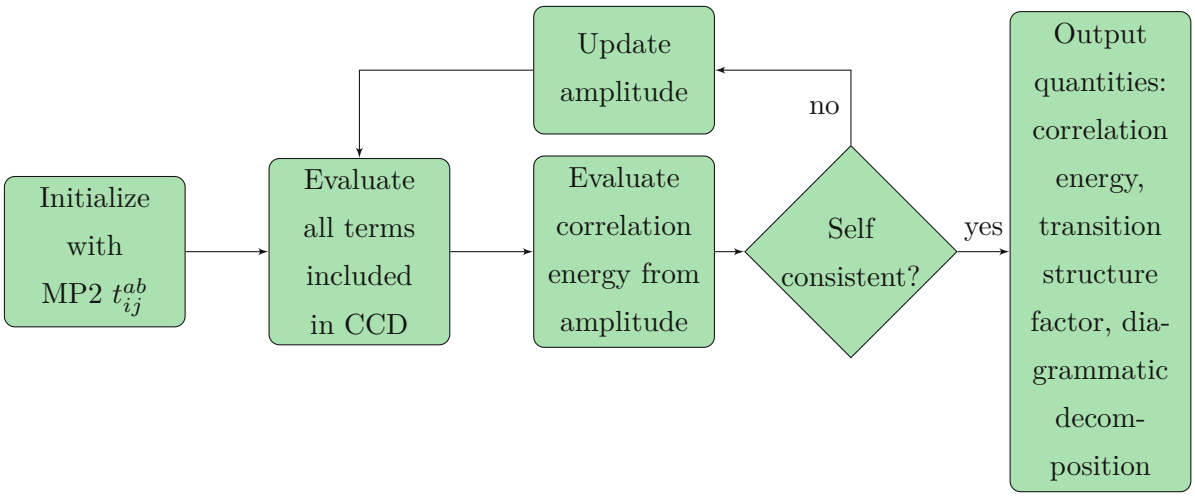

Figure 2.5: *Flowchart of solving CCD amplitude equations on the UEG model.*

Finally, in Fig.(2.6) we demonstrate a diagrammatic illustration of all the terms included in Eq. (2.30). The names assigned to these diagrams will be referenced in the next two chapters.

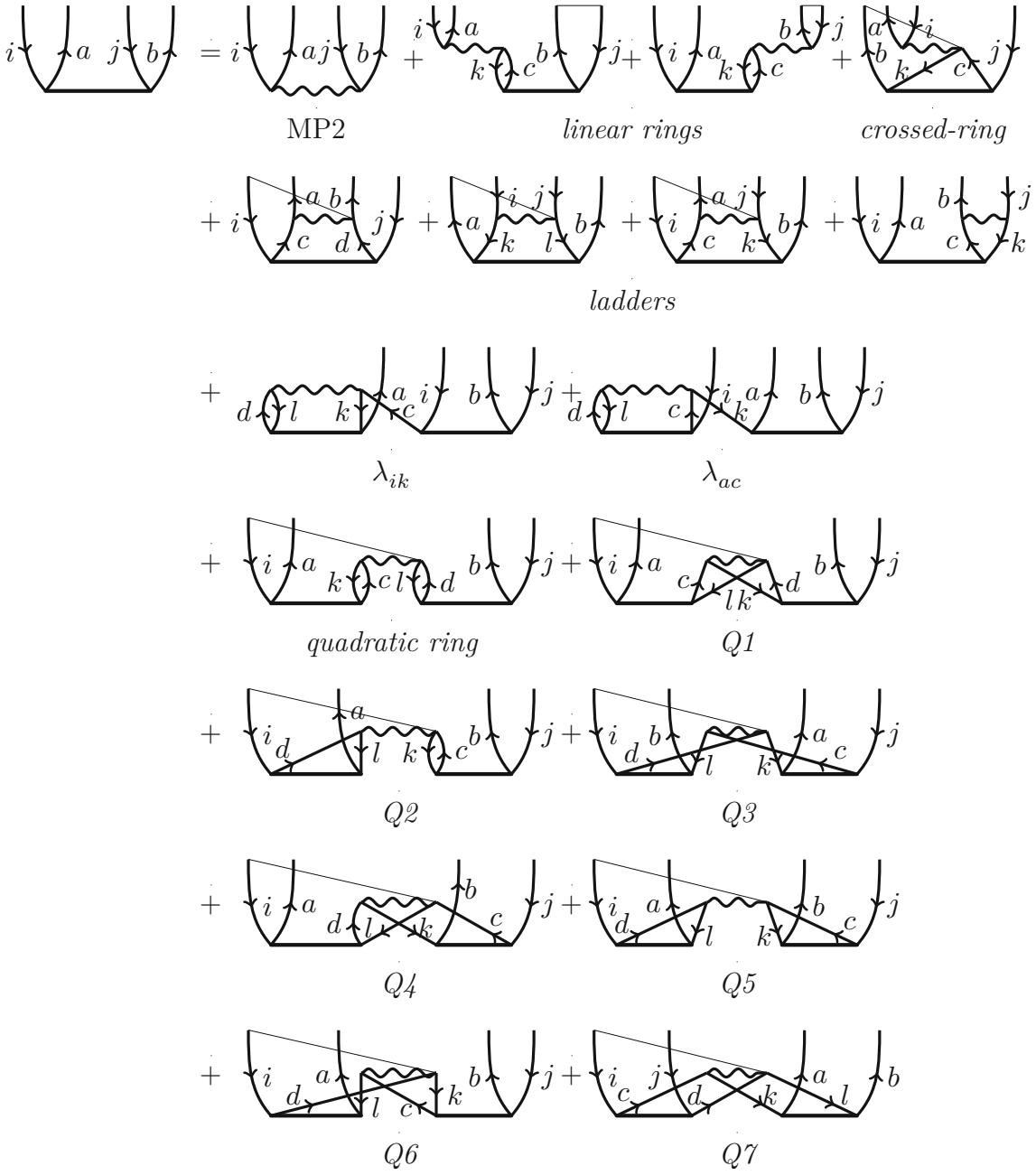

Figure 2.6: *Illustrations in Goldstone diagrams of the terms in Eq. (2.30).*

2.5.1 Thermodynamic limit and finite-size effects

To prevent electronic structure theories from becoming part of the ash heap of history and to guarantee that their findings and predictions align with reality and experimental observations, the properties of the systems under study must be estimated in the thermodynamic limit (TDL). The TDL is approached when $N \to \infty$ and $\Omega \to \infty$ simultaneously and at the same rate, with N representing the number of particles in the simulation supercell and Ω denoting its volume. This approach ensures that the density is kept constant.

Modeling, though, a bulk medium with a finite simulation cell and a fixed number of electrons introduces finite-size errors, affecting the accuracy of the calculation of the HF and correlation energy. These errors are defined as the differences between the results obtained from the thermodynamic limit and those from the finite simulation cell. In Hartree-Fock and post-Hartree-Fock simulations, the resulting finite-size errors often prove to be more significant than statistical and other systematic errors.

Unfortunately, the convergence of calculated properties of interest to the TDL is slow, due to the polynomial scaling of the computational complexity of most post-HF methods with respect to system size, and it can easily surpass the available computational resources, even in modern supercomputer clusters. For instance, a CCD calculation on the UEG model with approximately 1.000 electrons and 10.000 plane waves typically requires around 250 GB of memory. To that end, efforts have been made in developing wavefunction methods with reduced computational cost, aiming to overcome finite-size errors, effectively address long-range correlation effects, and facilitate the treatment of larger supercells in a computationally efficient manner.

On the other hand, considering that reaching the TDL computationally is a pipe dream, various strategies have been developed to address these errors. These approaches often include extrapolation methods, transition structure factor interpolation techniques, and twist-averaging [32, 33, 34, 31]. However, no single established protocol has yet been clearly defined.

To proceed, we present another definition of the electronic correlation energy at the CCD level, which is given by:

$$E_c^{\mathrm{CCD}} = \sum_{\mathbf{q}\neq 0} S^{\mathrm{CCD}}(\mathbf{q})\, v(\mathbf{q}). \tag{2.34}$$

Since the Fourier transform of the Coulomb potential diverges at $\mathbf{q} = 0$, it is numerically necessary to disregard this contribution to the sum. In the thermodynamic limit the sum in Eq. (2.34) is replaced by an integral over q. Therefore, finite-size errors in the calculation of properties of periodic systems originate from two sources [35]:

1. quadrature errors in the summation over $\mathbf{q}$.
2. the slow convergence of properties with respect to the employed supercell size.

More precisely, the latter are related to finite-size errors that arise in the calculation of the Hartree-Fock eigenenergies. As we have already seen, the exchange energy exhibits a singularity at $\mathbf{k}_i = \mathbf{k}_j$, which is integrable in the thermodynamic limit. In contrast, computationally, this singularity is replaced by the Madelung constant, which converges slowly to zero with respect to the system size. Since we employ Hartree-Fock eigenenergies in our numerical coupled-cluster calculations, these errors are inherited by the amplitudes, consequently affecting the transition structure factor and correlation energy.

Significant insights into the convergence of finite-size errors to the TDL can be obtained by analyzing the transition structure factor. For instance, Bishop and Lührmann showed analytically that the electronic structure factor obtained in the Random Phase Approximation (RPA), applied on the metallic UEG, has a linear slope ($\sim q$) at the long wavelength limit [36].[6] Without providing any proof, we point out that this linear behavior will also be present in the CCD transition structure factor.[7] This scaling in $S(\mathbf{q})$ affects energy extrapolations to the TDL. Specifically, given that the minimum distance of two wavevectors in reciprocal space is $2\pi/L$, we conclude that the finite-size errors of the correlation energy will decay as $N^{-2/3}$ in the thermodynamic limit [36].[8]

[6] The long-range behavior qualitatively differs between metals and insulators, where for the latter $S(\mathbf{q}) \sim q^2$.

[7] The close relationship between the RPA and CCD at the long wavelength will be studied and provided in the next chapter.

[8] For an insulator, where $S(\mathbf{q}) \sim q^2$, the decay of finite-size effects in the correlation energy in the TDL is N^{-1}.

Another valuable technique employed to reduce the impact of finite-size effects is twist-averaging, utilized to minimize the fluctuations in the calculated physical quantities at a given system size. Each k-point in the grid is displaced by a small amount $\mathbf{k}_s$, referred to as *offset* or *twist angle* [37]. This offset effectively breaks the degeneracy of the plane waves, whose wavevectors define the reciprocal grid and create the closed-shell filling effects. Subsequently, we average over all possible offsets to obtain the averaged physical quantity. This process results in a computational cost that scales linearly with the number, N_s, of twist angles used. However, increasing the system size can improve finite-size effects and reduce the scaling. We will exclusively address the method of twist averaging applied to the correlation energy and transition structure factor, with their averaged expressions is given by,

$$\langle E_c \rangle = \frac{1}{N_s} \sum_{k_s}^{N_s} E_c^{k_s} = \frac{1}{N_s} \sum_{k_s}^{N_s} \sum_{\mathbf{q}\tilde{i}\tilde{j}} v(\mathbf{q}) [2t_{\tilde{i}\tilde{j}}(\mathbf{q}) - t_{\tilde{j}\tilde{i}}(\mathbf{q})], \tag{2.35}$$

and

$$\langle S(\mathbf{q}) \rangle = \frac{1}{N_s} \sum_{k_s}^{N_s} S^{k_s}(\mathbf{q}). \tag{2.36}$$

respectively. Since the momentum transfer is defined as $\mathbf{q} = \mathbf{k}_a - \mathbf{k}_i$, it is not affected by the offset, while the influence on orbitals i and j is designated as $\tilde{i}$ and $\tilde{j}$. In conclusion, twist-averaging can resolve some finite-size errors that are present at a finite-N system size, resulting in a smoother convergence and allowing for improved extrapolations to the thermodynamic limit.

Finally, we discuss results obtained using the twist-averaging technique. In Fig. (2.3) (a)-(b), Γ-point calculations are shown, illustrating the presence of finite-size effects for the direct and exchange MP2 correlation energies, respectively. Furthermore, by running calculations for 40 different offsets, we observe an improvement over the numerical results, as the expected divergent and convergent behavior of the aforementioned energies is depicted more clearly.

Additionally, in Fig. (2.7)(a) and (b) Γpoint and twist-averaging transition structure factor are illustrated. These results were obtained by using 100 different offsets and averaging following Eq. (2.36). We observe that for small r_s (in our case $r_s = 2$ a.u.),

and 114 electrons, a minimum appears, indicating that the theory under study is convergent. Still, though, we are far from drawing significant conclusions about the convergence in the TDL. Artificially, by increasing the r_s, we reduce the spacing between the k-points, resulting in capturing sooner the long wavelength limit behavior, as depicted in Fig. (2.7)(b). Through interpolation between $q = 0$ and q_{min} for the structure factor, we are in a position to examine how finite-size effects in the correlation energy converge as the system approaches the TDL. This method accounts for the missing long-range electronic correlation effects and enables a finite-size correction.

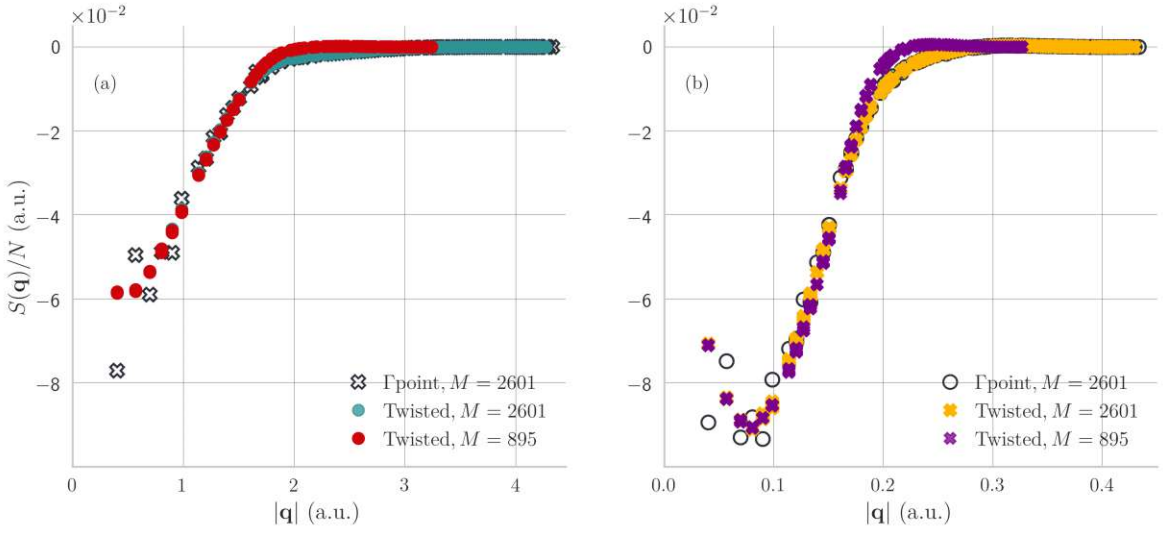

Figure 2.7: *CCD results for Γpoint and twist-averaging transition structure factors are presented for 114 electrons at (a) $r_s = 2$ a.u. and (b) $r_s = 20$ a.u. In the legend the numbers of employed basis sets for each method are specified.*

2.5.2 Complete basis set limit and the cusp condition

Electronic correlation is characterized, mostly, as a short-range phenomenon, given that the Coulomb potential—its origin—becomes dominant at small interelectronic distances. Consequently, in addition to their fermionic nature, the Coulombic interac-

tions between electrons also shape the form of the wavefunction at short interelectronic separations.

Specifically, at the coalescence points of electrons, a derivative discontinuity, referred to as a *cusp*, must emerge to counteract the singularity of the Coulomb potential through a divergence in the kinetic energy. It was Kato, in 1957, who demonstrated the continuity of the wavefunction throughout configuration space for the non-relativistic Hamiltonian [38, 39]. Moreover, he showed that the first-order partial derivative of the wavefunction is also continuous, except at the singular points of the Coulomb potential. This demonstration laid the foundation for Kato's cusp condition, which, in the case of singlet coupled electrons, is equivalent to:

$$\left.\frac{\partial \Psi}{\partial r_{ij}}\right|_{r_{ij}\to 0} = \frac{1}{2}\Psi(r_{ij}\to 0). \tag{2.37}$$

It is evident from the aforementioned that an accurate description of the wavefunction at short interelectronic distances will capture, to a large extent, the correlation energy of any physical system under consideration. Similarly to the case of approaching the thermodynamic limit, one must now take into account the limit of the complete basis set to achieve highly accurate results. Due to limited computational resources, calculations of post-Hartree-Fock methods are performed with a finite number of basis set functions. The size of the unoccupied or virtual basis set manifold, as we have seen in the case of the UEG,[9] is determined by truncation based on a kinetic energy cutoff, introducing a basis set incompleteness error (BSIE) in all calculated quantities.[10] Accessing the augmented virtual manifold will eventually reduce the BSIE, leading to more accurate calculations.

Post-Hartree-Fock methods, such as coupled-cluster and Møller-Plesset perturbation theory, rely on expanding the N-electron wavefunction in a basis of Slater determinants. However, these expansions are not suitable for accurately describing the electronic cusp, except for very large one-electron basis sets. Consequently, the convergence of

[9] The study of the UEG has advanced significantly due to QMC techniques that operate at the complete basis set limit.

[10] For the efficient implementation of correlated methods, it is crucial to choose an optimal number of orbitals that minimizes the basis set incompleteness error.

any physical property calculated by these methods toward the complete basis set limit is extremely slow.

On the other hand, the correlation cusp is present in all electronic wave functions. Consequently, every correlated wave function method suffers from this convergence problem. Its universal nature and the specific functional form of the correlation cusp, though, make the convergence with basis size both smooth and predictable. These characteristics enable the development of extrapolation techniques, which eventually remove the remaining basis set incompleteness error. In the case of plane wave basis set calculations, both analytic and numerical results from perturbation theory suggest the following expression [40]:

$$E_c(N_\mathrm{v}) = E_c(\mathrm{CBS}) + \frac{a}{N_\mathrm{v}}, \tag{2.38}$$

where $E_c(N_\mathrm{v})$ represents the correlation energy calculated in a truncated basis set, $E_c(\mathrm{CBS})$ is the complete basis set (CBS) limit, and a is a parameter determined through fitting. Theories that conform to this power-law convergence also comply with the cusp condition, thereby influencing the depth of the pair correlation function.

Without proof, a consequence of the linear cusp condition is a q^{-4} behavior of the transition structure factor at the short wavelength limit. As observed in Fig. (2.7)(a) and (b), increasing the number of plane waves alters the slope of the tail of the transition structure factor. A thorough analysis will provide meaningful insights about the behavior of theories and individual perturbative terms at this limit and their influence on the *transition* pair correlation function [41]. Further discussion will be presented in Chapter 4.

Caught between Scylla and Charybdis, between the thermodynamic and complete basis set limits, a debate has occurred regarding the optimal extrapolation order—whether it is more effective to first extrapolate to the TDL and subsequently to the CBS limit, or vice versa. In our correlation energies coupled-cluster calculations, we employ finite basis sets of size N_v and extrapolate to the complete basis set (CBS) limit using Eq. (2.38). Following this, we expand our system sizes and perform an extrapolation to the thermodynamic limit (TDL) using a $N^{-2/3}$ power-law.

Lastly, Fig. (2.8) illustrates the Hartree-Fock and the first-order wavefunction for the spin-singlet 2-electron UEG system, following the methodology in [42]. As expected,

the Hartree-Fock wavefunction, depicted by a flat line, lacks an electron-electron cusp, since it cannot capture Coulomb correlation as a mean field theory.

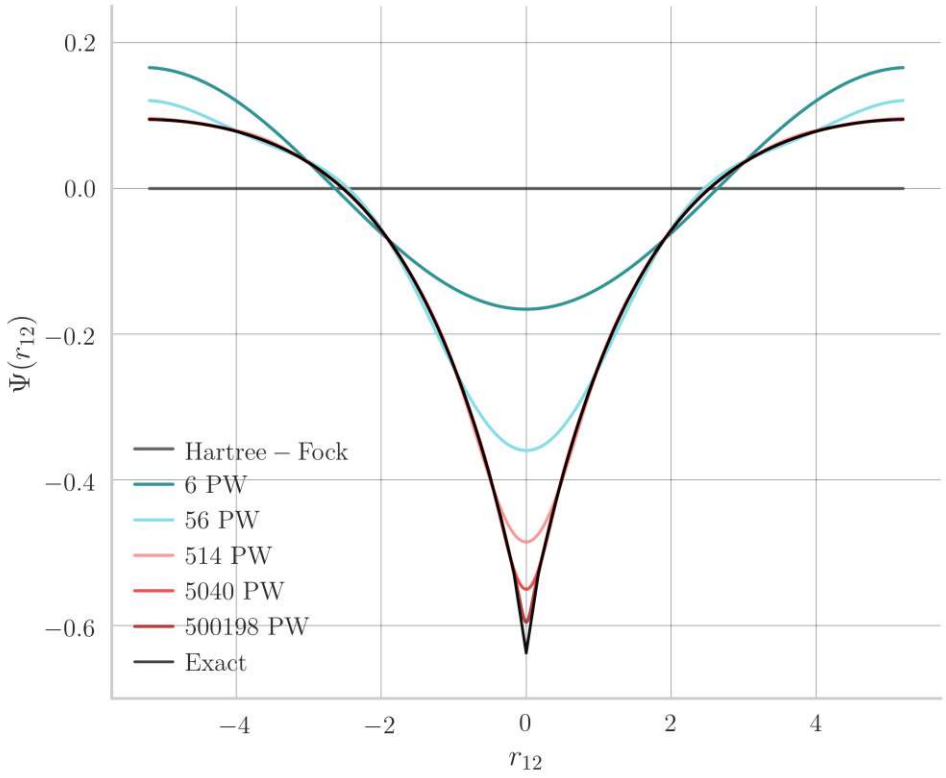

Figure 2.8: *First-order wavefunction, plotted with respect to the interelectronic distance r_{12}, for the two electron UEG at $r_s = 3$ a.u. and increasing plane wave basis set, up to a total basis of 500.198 plane waves. In this configuration, one electron is fixed at the center of the cubic box, while the other moves in a diagonal line through the cube and the coalescence point.*

Furthermore, as observed, the slow convergence, with respect to the number of plane waves,[11] is rooted in the linear r_{12} shape of the MP1 wavefunction in the vicinity of the coalescence point. Notably, a considerable number of virtual orbitals is practically required to capture significant contributions from short-range phenomena.

[11] Plane waves are spatially delocalized orbitals and their use is not suitable to exploit short-range electronic correlation.

Chapter 3

Averting the Infrared Catastrophe in the Gold Standard of Quantum Chemistry

The following chapter is a modification of the publication found in [43].

The scope of this chapter is to clarify the reasons behind the limitations of coupled-cluster theories, when applied to zero-gap systems, and to introduce a new method that, effectively, addresses these challenges. As we briefly discussed previously, coupled-cluster theories can be used to compute *ab initio* electronic correlation energies of real materials with systematically improvable accuracy. Nonetheless, the widely used coupled-cluster singles and doubles plus perturbative triples [CCSD(T)] method cannot be deployed as a panacea, since it is only applicable to insulating materials. Especially in the case of zero-gap materials, the truncation of the underlying many-body perturbation expansion leads, unluckily, to an infrared catastrophe. In order to tackle

this challenge, we present a novel perturbative triples formalism, denoted as (cT), which yields convergent correlation energies in metallic systems. Additionally, the computed correlation energies for the three-dimensional uniform electron gas at metallic densities are in good agreement with, the highly accurate, quantum Monte Carlo results. At the same time, the newly proposed method retains all desirable properties of CCSD(T), such as its accuracy for insulating systems, as well as its low computational cost ($\mathcal{O}(N^7)$),[1] compared to the full inclusion of the triples in CCSDT ($\mathcal{O}(N^8)$) [44]. Ultimately, this paves the way for *ab initio* calculations of real metals with chemical accuracy.

3.1 Metallic systems: the stalemate of ab initio methods

Over the past decades, theoretical and computational frameworks have jointly advanced. However, when it comes to calculating the properties of specific physical systems and understanding physical processes and phenomena, we still find ourselves in a deadlock. To that end, *ab initio* methods that achieve systematically improvable accuracy for metallic systems are urgently needed to study and comprehend chemical reactions on metal surfaces or to compute the thermodynamic stability of materials. Currently available exchange and correlation energy density functionals often fall short of achieving the desired level of accuracy compared to experiment. A prominent failure includes the incorrect prediction of molecular adsorption sites on metal surfaces [45]. As an alternative, more accurate quantum Monte Carlo (QMC) calculations, albeit computationally more expensive than density functional theory (DFT), can be applied to metals [46, 47]. However, even diffusion QMC (DMC) calculations exhibit a strong dependence on the fixed node approximation [48]. In contrast to QMC and DFT, many-electron perturbation theories offer a conceptually different approach to solve the many-electron problem with high accuracy. Coupled-cluster (CC) theory, in particular, provides a systematically improvable ansatz to the many-electron wave function

[1] N denotes a measure of the system size.

by employing a series of higher order particle-hole excitation operators. While systems exhibiting strong correlation, such as stretched covalent bonds, require high-order excitation operators or multireference approaches, single reference systems can already be accurately described using low orders [49]. Specifically, at the truncation level of single, double and perturbative triple particle-hole excitation operators, CCSD(T) theory predicts atomization and reaction energies with an accuracy of approximately 1 kcal/mol for a wide class of single-reference molecules [49]. As a result, CCSD(T) is often referred to as the "gold standard" of molecular quantum chemistry. This also motivated recent applications of coupled-cluster theory to study solids [50, 51, 52, 53, 35, 54], leading to highly accurate predictions of, for example, pressure-temperature phase diagrams [55]. However, it is important to note that such calculations require a careful convergence with respect to the employed basis sets and system sizes–tasks that are considerably more complicated than those at lower levels of theory [51, 35, 56].

Moreover, metallic systems still constitute a major challenge for currently available CC theories. Although CCSD can be applied to metallic systems, recent results indicate that CCSD fails in achieving chemical accuracy in metals, which is expected and agrees with findings for molecules and insulating solids [57, 58]. The inclusion of the perturbative triples correction (T), though, is not possible due to the so-called infrared catastrophe resulting from the truncation of the many-electron perturbation expansion [11]. The infrared catastrophe leads to a divergence of the CCSD(T) correlation energy per electron for metals as simulation cell sizes increase, also known as the thermodynamic limit (TDL). While a full non-perturbative inclusion of the triple excitation operator in the CC method is convergent, it is computationally too expensive and can only be applied to few relatively small systems [59]. In the following, we will present a modification to the perturbative triples theory that is applicable to metals while retaining all desirable properties, including accuracy for insulating systems and low computational cost compared to a full inclusion of the triples.

3.2 Setting the stage

Singularities and divergences have always been a headache for physicists. Specifically, in the contexts of electronic structure calculations and perturbation theories, here denoted as (X), the so-called infrared catastrophe originates from the truncation of the many-electron perturbation expansion in conjunction with the long-range nature of the Coulomb interaction. Throughout our analysis we make use of the following three quantities: the correlation energy $E_{\mathrm{c}}^{(X)}$, the electronic transition structure factor $S^{(X)}(\mathbf{q})$ and the quantity $T_i^{(X)}(\mathbf{q})$. With these arrows in our quiver, we attempt to understand, identify and even resolve the infrared catastrophe problem in CCSD(T) theory. We start by defining the correlation energy as:

$$E_{\mathrm{c}}^{(X)} = \sum_{\mathbf{q}} v(\mathbf{q}) \underbrace{\left[\frac{\delta v_{ij}^{ab}}{\delta v(\mathbf{q})} \left(2t_{ij}^{ab} - t_{ji}^{ab} \right)_{(X)} \right]}_{:= S^{(X)}(\mathbf{q})} . \tag{3.1}$$

The indices i, j and a, b indicate occupied and virtual spatial orbitals, respectively. Einstein summation convention applies to repeated indices throughout this chapter. We will first focus on second-order perturbation theory, direct ring CC doubles (rCCD) theory, which is closely related to the random-phase approximation (RPA), as well as CC doubles theory (CCD). We again note that, due to the symmetry of the uniform electron gas (UEG) Hamiltonian, single excitations are absent. Furthermore, in the UEG, the one-electron orbitals are plane waves with wave vectors $\mathbf{k}_i$, $\mathbf{k}_j$ and $\mathbf{k}_a$, $\mathbf{k}_b$. This allows us to write the two-electron repulsion integral as,

$$v_{ij}^{ab} = v(\mathbf{q}) \delta_{\mathbf{k}_a - \mathbf{k}_i, \mathbf{k}_j - \mathbf{k}_b}, \qquad \text{with} \quad v(\mathbf{q}) = \frac{4\pi}{\Omega \left| \mathbf{q} \right|^2}, \tag{3.2}$$

and its functional derivative, enabling a concise notation, can be expressed as,

$$\frac{\delta v_{ij}^{ab}}{\delta v(\mathbf{q})} = \delta_{\mathbf{q}, \mathbf{k}_j - \mathbf{k}_b} \delta_{\mathbf{q}, \mathbf{k}_a - \mathbf{k}_i} . \tag{3.3}$$

Here, $v(\mathbf{q})$ is the Fourier transform of the electronic Coulomb repulsion, $\mathbf{q} = \mathbf{k}_a - \mathbf{k}_i$ denotes the momentum transfer vector, and Ω is the volume of the simulation cell. In contrast, the amplitudes t_{ij}^{ab} are obtained by solving the amplitude equations of

the employed many-electron perturbation theory, either recursively or in a one-shot manner.

Moreover, Eq. (3.1) introduces the electronic transition structure factor $S(\mathbf{q})$, providing an insight into the dependence of the correlation energy on the interelectronic interaction distance. An additional quantity of significance for the present analysis is given by,

$$T_i^{(X)}(\mathbf{q}) = \left[\frac{\delta v_{ij}^{ab}}{\delta v(\mathbf{q})} t_{ij}^{ab}{}_{(X)} \right]. \tag{3.4}$$

Similar to the structure factor, $T_i^{(X)}(\mathbf{q})$ depends on the momentum transfer vector $\mathbf{q}$.

3.3 Infrared catastrophe in MP2: the point of inception

Having introduced the most important quantities needed for our analysis, we now turn to the case of second-order perturbation theory, which is a classical textbook example for the infrared catastrophe. In particular, we focus on second-order Møller-Plesset perturbation theory (MP2), which employs the Hartree-Fock (HF) Hamiltonian as the unperturbed reference system [60].

The MP2 correlation energy is given by Eq. (3.1), where the amplitudes are initialized as $t_{ij}^{ab} = v_{ij}^{ab}/\Delta_{ab}^{ij}$, and $\Delta_{ab}^{ij} = \varepsilon_i + \varepsilon_j - \varepsilon_a - \varepsilon_b$. In the case of the UEG and zero-gap systems, the correlation energy exhibits a divergence due to the summation over elements in the amplitudes with both the occupied and virtual orbitals, i and a, lying in proximity to the Fermi surface. The rate of divergence is $\log(|\mathbf{q}|)$ [21] and $\log[\log(|\mathbf{q}|)]$ [23] for Hartree and HF orbital energies, respectively. Here, $|\mathbf{q}|$ represents the lower spherical cutoff radius in the analytical integration over $\mathbf{q}$. For the remainder of our analysis, we exclusively use HF orbital energies.

Unfortunately, the comparison between analytic and numerical results is slightly complicated, given that the slow approach of the energy denominator Δ_{ab}^{ij} towards the analytic behavior of $\lim_{|\mathbf{q}|\to 0} \Delta_{ab}^{ij} \propto |\mathbf{q}| \log(|\mathbf{q}|)$ is intrinsically linked to the size of the

studied system. However, our numerical findings for t_{ij}^{ab} presented in Fig. 3.1(a) agree reasonably well with the analytic result of $\propto |\mathbf{q}|^{-3}/\log(|\mathbf{q}|)$. Finally, the infrared catastrophe is also evident in the MP2 electronic transition structure factor, $S^{\mathrm{MP2}}(\mathbf{q})$, due to its singularity at $|\mathbf{q}| = 0$. This observation can readily be inferred from the plot for MP2 theory, illustrated in Fig. 3.3.

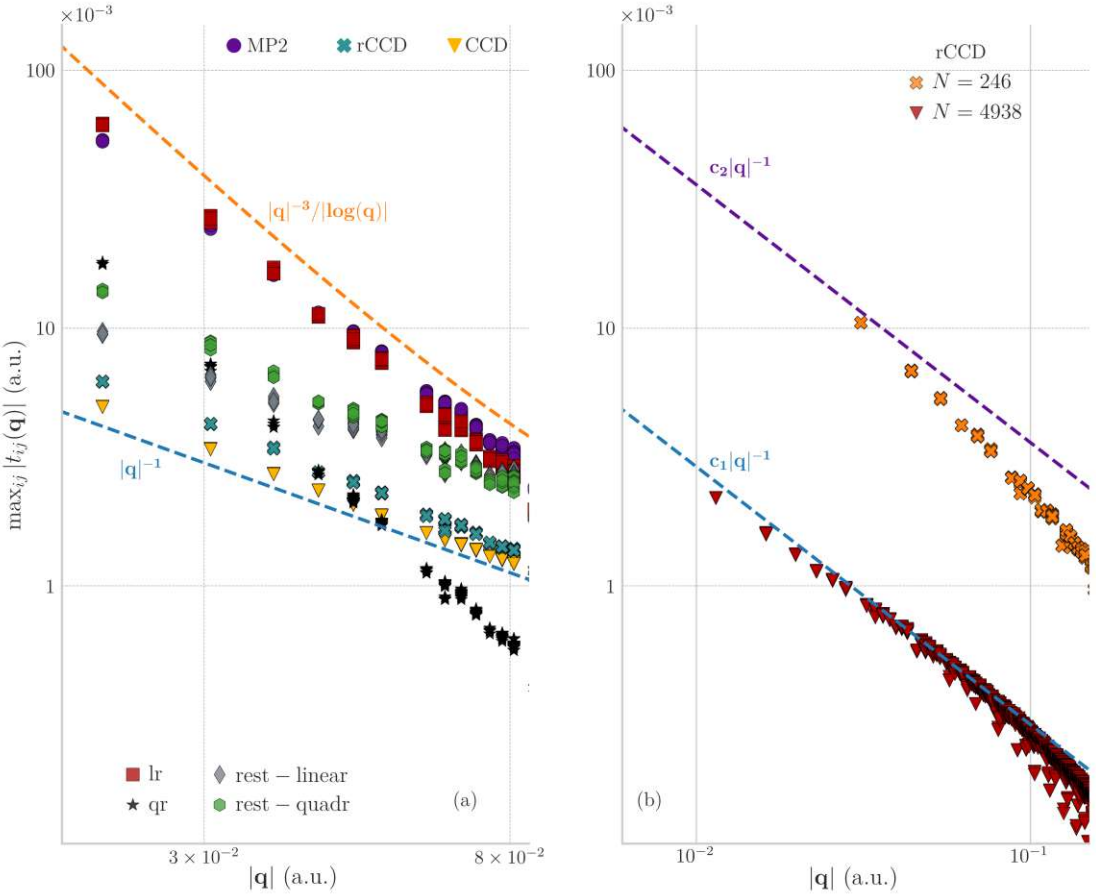

Figure 3.1: *Results for the maximum t-amplitude element on an absolute scale for a given momentum* $\mathbf{q}$*: (a)* $t_{ij}(\mathbf{q})$ *calculated at different levels of theory and diagrammatic contributions, listed as rest-linear and rest-quadratic, for* 730 *electrons with* 6254 *spatial orbitals,* 40 *twists and* $r_s = 20$ *a.u. (b) rCCD* $t_{ij}(\mathbf{q})$ *for two different systems sizes and roughly 18 spatial orbitals per occupied illustrating the expected theoretical divergence of* $1/\mathbf{q}$ *at the long wavelength limit.*

3.4 The ring summation: a remedy with a price

As already demonstrated by Macke in 1950 [61], and later, in 1957, by Gell-Mann and Brueckner [62], the divergence in second-order perturbation theory can be averted by including carefully selected higher-order contributions of the many-electron perturbation expansion, corresponding to ring diagrams. Algebraically, this can be implemented by solving the ring-coupled-cluster amplitude equation,

$$t_{ij}^{ab} = \left(v_{ij}^{ab} + 2v_{ic}^{ak}t_{kj}^{cb} + 2t_{ik}^{ac}v_{cj}^{kb} + 4t_{ik}^{ac}v_{cd}^{kl}t_{lj}^{db}\right)/\Delta_{ab}^{ij}, \tag{3.5}$$

which is formally equivalent to solving the Casida equations [63]. The Eq. (3.5) is illustrated diagrammatically as:

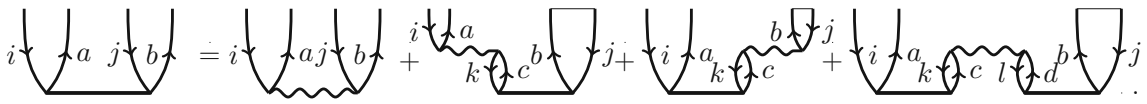

For the ring-coupled-cluster correlation energy to converge in the long wavelength limit, the first term on the right-hand side of Eq. (3.5), which is equivalent to MP2 theory, needs to be partially canceled by the additional linear ring (lr) and quadratic ring (qr) terms in the amplitudes.

We now address the question: *How do the terms on the right-hand side in Eq. (3.5) cancel each other in the limit* $|\mathbf{q}| \to 0$*?* To this end, we rewrite Eq. (3.5) in the following way

$$t_{ij}^{\mathrm{rCCD}}(\mathbf{q}) = v(\mathbf{q})\Bigg[1 + 2\sum_{k} t_{kj}^{\mathrm{rCCD}}(\mathbf{q}) + 2\sum_{k} t_{ik}^{\mathrm{rCCD}}(\mathbf{q}) + 4\sum_{kl} t_{il}^{\mathrm{rCCD}}(\mathbf{q})t_{kj}^{\mathrm{rCCD}}(\mathbf{q})\Bigg]/\Delta_{ab}^{ij}, \tag{3.6}$$

which is feasible because of momentum conservation and the fact that ring diagrams couple the same momenta $\mathbf{q}$. As was shown by Freeman in Ref. [8], and later by Emrich and Zabolitzky in Ref. [64], who followed a different formalism, the solution of the above equation in the long wavelength limit, briefly presented in Appendix B,

leads to,

$$\lim_{|\mathbf{q}|\to 0} T_i^{\mathrm{rCCD}}(\mathbf{q}) = -\frac{1}{2}. \tag{3.7}$$

Consequently, the terms in the parenthesis in Eq.(3.6) vanish such that [8],

$$\lim_{|\mathbf{q}|\to 0} t_{ij}^{\mathrm{rCCD}}(\mathbf{q}) \propto -\frac{1}{|\mathbf{q}|}\,. \tag{3.8}$$

We note that amplitudes diverging as $|\mathbf{q}|^{-1}$, result in convergent correlation energies and vanishing $S(\mathbf{q})$'s for small $|\mathbf{q}|$ values. The above findings are consistent for both Hartree and Hartree-Fock orbital energies. Numerical results for $t_{ij}^{\mathrm{rCCD}}(\mathbf{q})$ are presented in Fig. 3.1(a) and 3.1(b). Specifically, the largest t-amplitude element is depicted on an absolute scale for a given momentum $\mathbf{q}$. In both figures, the amplitudes diverge with the analytically known behavior of $|\mathbf{q}|^{-1}$ in the long wavelength limit. Unfortunately, this behavior sets in only for very large electron numbers, as a consequence of the finite size error.

Furthermore, in Fig. 3.4(a) and 3.4(b), numerical results are illustrated, confirming Eq. (3.7). One can observe that the minimum value of $T_i(\mathbf{q})$ converges slowly with respect to the system size, towards the theoretically expected value of -0.5.

We complement the above discussion by studying numerically the rCCD transition structure factor and its individual diagrammatic contributions [41] given by,

$$S^{\mathrm{rCCD}}(\mathbf{q}) = S^{\mathrm{MP2}}(\mathbf{q}) + S^{\mathrm{lr}}(\mathbf{q}) + S^{\mathrm{qr}}(\mathbf{q}). \tag{3.9}$$

Diagrammatically, Eq. (3.9) is displayed as, The calculated contributions to $S(\mathbf{q})$ are

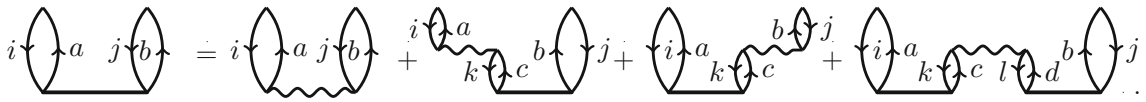

depicted in Fig. 3.3. Although the individual contributions diverge, the total rCCD transition structure factor converges towards zero in the long wavelength limit ($\mathbf{q} \to 0$), as indicated by Fig. 3.2(a) and 3.2(b). We arrive at the first important insight of our analysis. *The singularity at $|\mathbf{q}| = 0$ in $S^{MP2}(\mathbf{q})$ is canceled by one-half of the linear ring terms, whereas the singularity of the quadratic ring term is canceled by the "other" half of the linear term.*

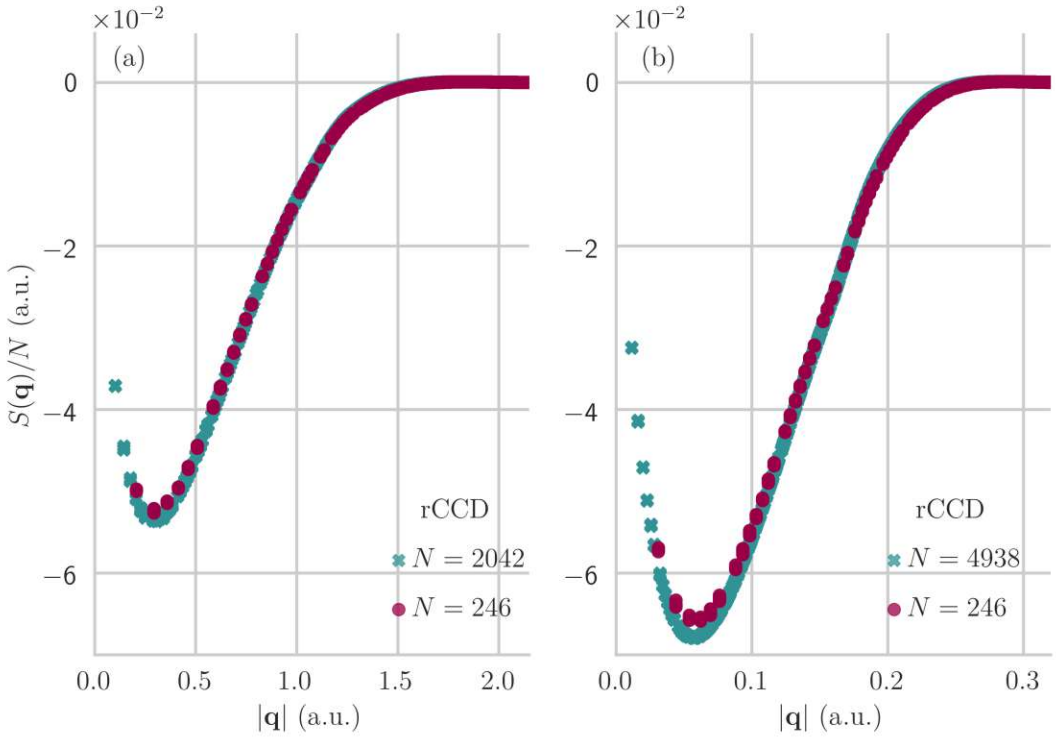

Figure 3.2: *rCCD transition structure factors for different densities and numbers of electrons. (a) $r_s = 3$ (a.u) and (b) $r_s = 20$ (a.u). In both densities, roughly 18 virtual spatial orbitals per occupied were used, with 100 twists for the small systems and 40 twists for the bigger ones. This illustrates that the discussed behavior of the structure factor not only holds for $r_s = 20$, but is also true for the important range of values between 1 and 5. However, at lower densities, the minimum of the structure factor is already observable for smaller system sizes. This was the reason for choosing a rather high value of r_s in our analysis.*

It is important to note that the leading-order behavior of $S^{\mathrm{rCCD}}(\mathbf{q})$ in the long wavelength limit is $S^{\mathrm{rCCD}}(\mathbf{q}) \propto |\mathbf{q}|$. This was shown by Bishop and Lührmann [65], and a more detailed discussion can be found in Ref. [66]. For simulation cells with finite electron numbers, this results in a finite size error scaling of $N^{-2/3}$, where N is the number of electrons. In passing, we mention that, insulating systems have a different

leading order behavior around $\mathbf{q} \approx 0$ given by $S^{\mathrm{rCCD}}(\mathbf{q}) \propto |\mathbf{q}|^2$, implying a finite size error scaling of N^{-1} [67, 68].

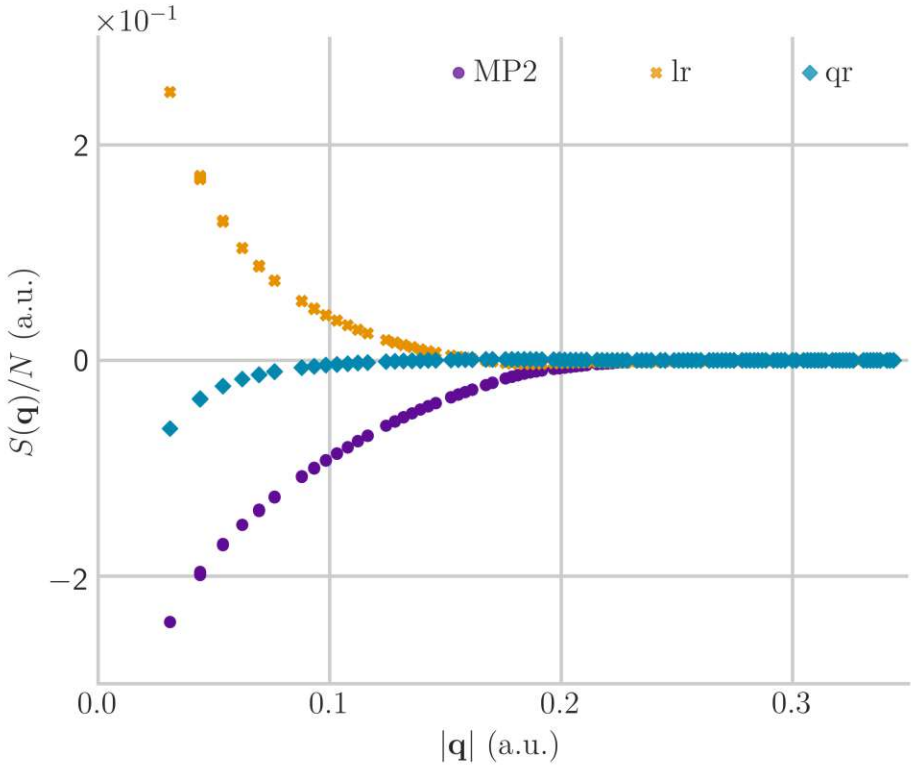

Figure 3.3: *Diagrammatic contributions of MP2, linear ring (lr) and quadratic ring (qr) to the rCCD transition structure factor in the UEG. Results were obtained using* 246 *electrons with* 2178 *spatial orbitals,* 266 *twists and* $r_s = 20$ *a.u.*

Although rCCD cures the MP2 divergence and correctly captures non-local long-range correlation effects, which are not included in popular DFT functionals using the LDA and GGA, it may be inadequate for accurately describing systems where mid and short-range correlations play a significant role. For this reason, achieving the desired level of accuracy, especially for metallic systems, requires including not only the full terms in the doubles excitations subspace but also higher-order terms. However, the price one has to pay is a higher computational cost.

3.5 Hotter but still cold: the coupled-cluster doubles method

In addition to ring diagrams, CCD theory includes further terms, linear and quadratic in $t_{ij}^{\mathrm{CCD}}(\mathbf{q})$ as it was shown in Eq. (2.30). This intricate coupling of different diagrammatic contributions makes an analytic solution impossible, even for the simple UEG model. Note that the contributions of the linear terms are even identical to those from third-order perturbation theory, if $t_{ij}^{\mathrm{CCD}}(\mathbf{q})$ is replaced by $v_{ij}^{ab}/\Delta_{ab}^{ij}$. As discussed by Mattuck [21] for any finite-order perturbation theory, ring terms yield the most divergent contributions at small $|\mathbf{q}|$ values. We stress that the dominance of the ring terms originates from the "piling-up of factors $1/q^2$," as the greatest piling-up occurs for the ring terms when only a single momentum transfer is involved [62]. Therefore, this dominance prevails irrespectively of the usage of $t_{ij}^{\mathrm{CCD}}(\mathbf{q})$ instead of $v_{ij}^{ab}/\Delta_{ab}^{ij}$ at small $|\mathbf{q}|$. Consequently, it follows, in agreement with the work of Emrich and Zabolitzky [64], that for the long wavelength limit: (i) in the CCD amplitude equations the most divergent contributions are the ones given in Eq. (3.6), and (ii) these ring contributions to the CCD amplitudes must therefore cancel each other precisely as for the rCCD amplitude equations. This leads us to one pivotal conclusion of the present study:

$$\lim_{|\mathbf{q}|\to 0} T_i^{\mathrm{CCD}}(\mathbf{q}) = \lim_{|\mathbf{q}|\to 0} T_i^{\mathrm{rCCD}}(\mathbf{q}) = -\frac{1}{2}. \tag{3.10}$$

We corroborate the above paragraph with numerical results for the individual contributions to $t_{ij}^{\mathrm{CCD}}(\mathbf{q})$. Fig. 3.1(a) depicts that the lr and qr contributions diverge as $\propto |\mathbf{q}|^{-3}/\log(q)$. Contrary to the previous section, where rCCD amplitudes were employed, the lr and qr contributions are now evaluated using CCD amplitudes. Moreover, it is shown that the remaining linear and quadratic contributions to the CCD amplitudes, denoted as rest-linear and rest-quadr, respectively, diverge with a weaker power for $\mathbf{q} \to 0$.

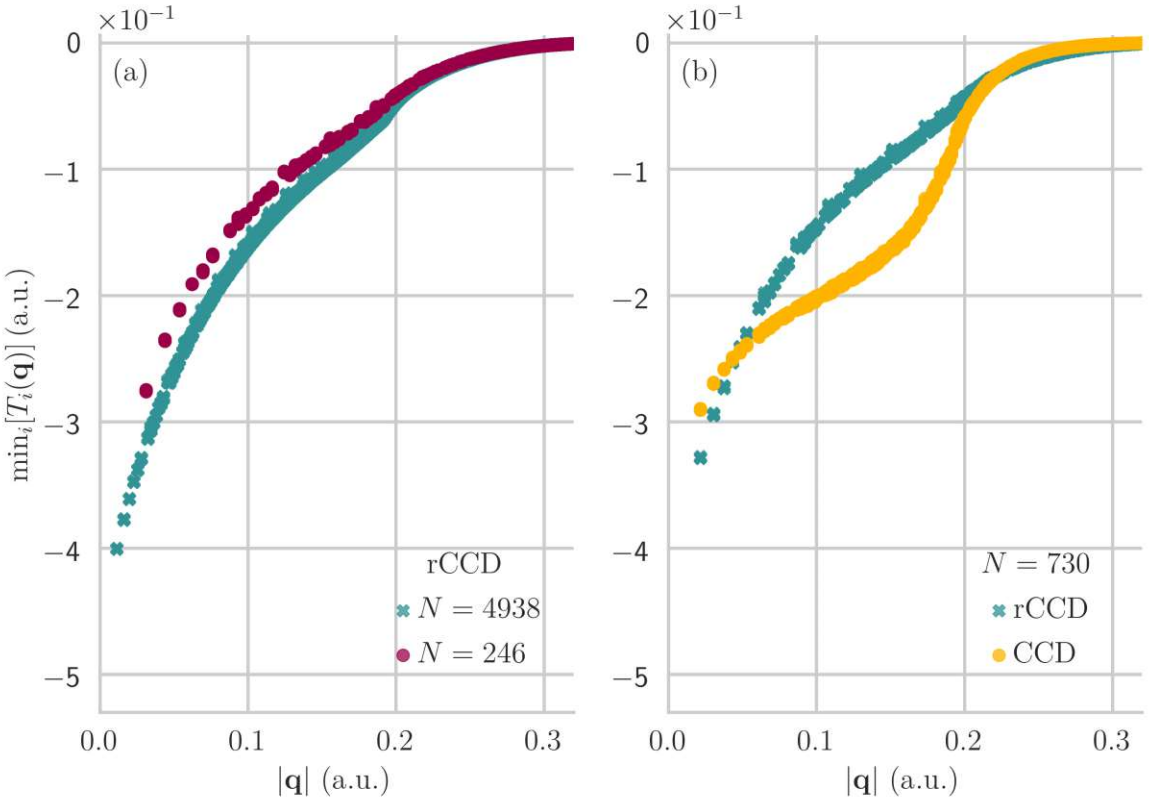

Figure 3.4: *Numerical results for the UEG showing the slow convergence of the minimum value of the quantity $T_i(\mathbf{q})$ for a given momentum transfer $\mathbf{q}$. (a) rCCD results for two different number of electrons (b) rCCD and CCD results for $N = 730$. The calculations were performed for $r_s = 20$ a.u., and roughly 18 virtual spatial orbitals per occupied were used.*

This underpins the conclusions drawn above that, in the long wavelength limit: (i) the ring contributions to CCD amplitudes dominate, and (ii) the ring terms cancel each other precisely as in rCCD. Furthermore, we observe that $t_{ij}^{\mathrm{CCD}}(\mathbf{q}) \propto |\mathbf{q}|^{-1}$, resulting in a transition structure factor $S^{\mathrm{CCD}}(\mathbf{q})$ depicted in Fig. 3.5, that also approaches zero linearly as the limit of $\mathbf{q} \to 0$.

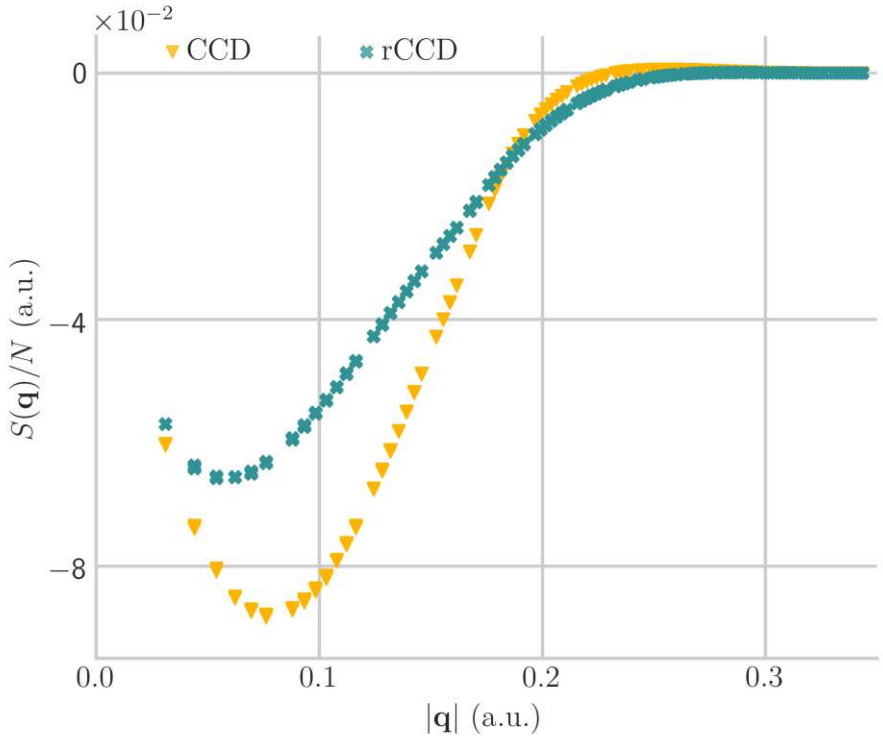

Figure 3.5: *rCCD and CCD transition structure factors for the UEG. The calculations were performed for 246 electrons with 2178 spatial orbitals, 266 twists for rCCD, 166 twists for CCD and* $r_s = 20\,$*a.u.*

3.6 Triple particle-hole excitation operators

We now turn to CC theories that approximate the triple particle-hole excitation operator in a perturbative manner. In these cases, the post-CCSD correlation energy and transition structure factor contributions are given by:

$$E_{\mathrm{c}}^{(J)} = \sum_{\mathbf{q}} v(\mathbf{q}) \underbrace{\left[\frac{\delta W_{ijk}^{abc}}{\delta v(\mathbf{q})} \left(A_{abc}^{ijk} \right)_{(J)} \right]}_{:= S^{(J)}(\mathbf{q})} . \tag{3.11}$$

Here, (J) refers to the employed approximation. In the case of (T), we have:

$$A^{ijk}_{abc} = \frac{\bar{W}^{ijk}_{abc}}{\Delta^{ijk}_{abc}}, \quad \text{with} \quad \bar{W}^{ijk}_{abc} = \frac{4}{3}W^{ijk}_{abc} - 2W^{ijk}_{acb} + \frac{2}{3}W^{ijk}_{bca}. \tag{3.12}$$

The quantity Δ^{ijk}_{abc} refers to the difference in HF orbital energies between the occupied and unoccupied states, labeled with the indices i, j, k and a, b, c, respectively. Moreover, W^{abc}_{ijk} is defined as:

$$W^{abc}_{ijk} = P^{abc}_{ijk}\left(t^{ae}_{ij}v^{bc}_{ek} - t^{ab}_{im}v^{mc}_{jk}\right), \tag{3.13}$$

where the diagrammatic illustration of the terms inside the parentheses of Eq. (3.13) is presented below:

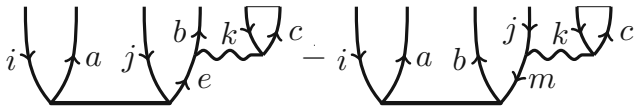

The permutation operator P^{abc}_{ijk} is defined as:

$$P^{abc}_{ijk}W^{abc}_{ijk} = W^{abc}_{ijk} + W^{acb}_{ikj} + W^{cab}_{kij} + W^{cba}_{kji} + W^{bca}_{jki} + W^{bac}_{jik}. \tag{3.14}$$

We employ the following functional derivative to provide a concise notation for defining the structure factor:

$$\frac{\delta W^{abc}_{ijk}}{\delta v(\mathbf{q})} = P^{abc}_{ijk}\left(t^{ae}_{ij}\delta_{\mathbf{q},\mathbf{k}_k-\mathbf{k}_c} - t^{ab}_{im}\delta_{\mathbf{q},\mathbf{k}_k-\mathbf{k}_c}\right), \tag{3.15}$$

where using Eq. (4.6) and Eq. (3.15), we obtain the diagrammatic illustration of the (T) structure factor[2]:

$$S^{(T)}(\mathbf{q}) \approx P^{abc}_{ijk}$$

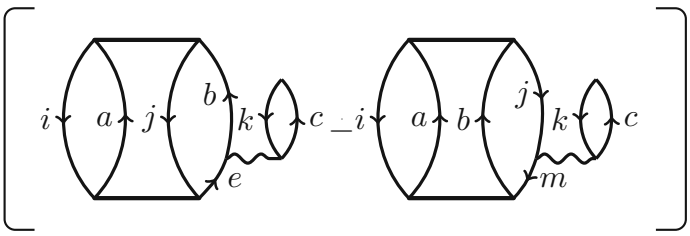

[2]For brevity, we have omitted the crossed contractions between the two terms.

The corresponding results are depicted in Fig. 3.6. We observe that $S^{(\mathrm{T})}(\mathbf{q})$ shares many similarities with $S^{\mathrm{MP2}}(\mathbf{q})$, shown in Fig. (3.3). Both $S(\mathbf{q})$'s exhibit a singularity at the long wavelength limit and yield correlation energies per electron that diverge as the system size increases. The *"Achilles' heel"* in applying (T) to metallic systems lies in the infrared catastrophe caused by the unscreened Coulomb interactions, included in the approximation to A^{ijk}_{abc} [11]. The pathogeny of this effect is illustrated in the red, dashed frames below:

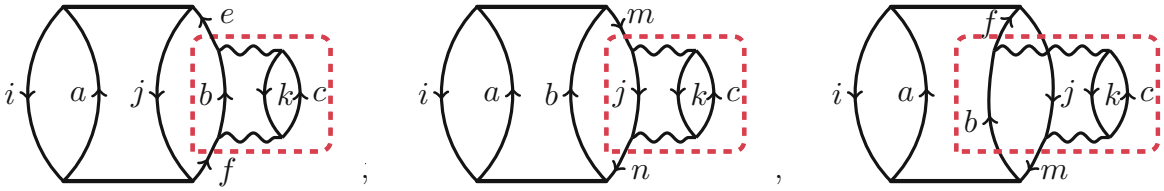

In the remaining of this section, we introduce a novel correlation energy expression that yields convergent energies for the UEG at the level of triple particle-hole excitation operators without depending on any *ad hoc* parameters. We refer to the method as (cT) because it includes the *complete* set of terms present in the triples amplitude equations in a noniterative manner. Naturally, the coupling of triples amplitudes with each other is disregarded. Thus, in (cT) we use the following approximation to $A^{ijk}_{abc} = \bar{M}^{ijk}_{abc}/\Delta^{ijk}_{abc}$, where

$$M^{ijk}_{abc} = P^{abc}_{ijk}\left(t^{ae}_{ij}v^{bc}_{ek} + 2t^{ae}_{ij}v^{bm}_{ef}t^{fc}_{mk} + \ldots\right). \tag{3.16}$$

Similarly to before, the terms inside the parentheses of Eq. (3.16) are represented as:

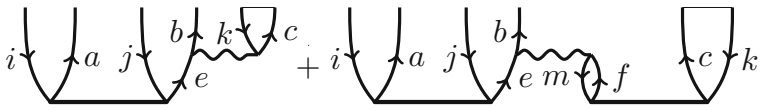

For brevity we show only a selection of terms that exhibit a divergent behavior as $\mathbf{q}$ approaches 0. Note that the (T) and (cT) approximation to A^{ijk}_{abc} agree for all terms which are linear in t^{ab}_{ij}. To cancel the divergence in (T), (cT) includes additional ring terms such as the second term in Eq. (3.16), and the above diagrammatic illustration.

For these terms, it follows that:

$$v_{ek}^{bc} + 2v_{ef}^{bm} t_{mk}^{fc} = v_{ek}^{bc} \left[1 + 2T_m(\mathbf{q}')\right], \quad \text{with} \quad \mathbf{q}' = \mathbf{k}_k - \mathbf{k}_c. \tag{3.17}$$

Note that as $\mathbf{q}' \to 0 : 1 + 2T_m(\mathbf{q}') = 0$. This is formally identical to the results for the cancellation of the divergence between the linear ring and the MP2 terms in the long wavelength limit. We stress that (cT) also includes additional *rest* terms that are not related to the divergence of (T), similar to the MP2 and CCD levels of theory.

In addition to $S^{(\mathrm{T})}(\mathbf{q})$, we introduce $S^{(\mathrm{cT})}(\mathbf{q})$. A partial diagrammatic representation of it, using Eq. (4.6), Eq. (3.15), and Eq. (3.16) is:

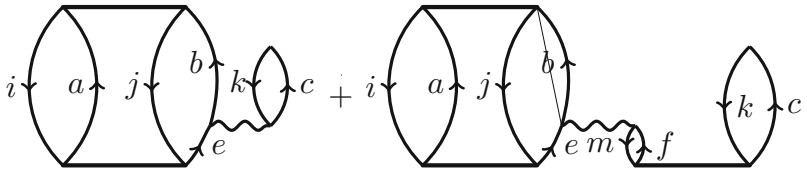

As supporting numerical evidence, Fig. 3.6 depicts $S^{(\mathrm{cT})}(\mathbf{q})$, which exhibits a qualitatively different behavior than $S^{(\mathrm{T})}(\mathbf{q})$ and indicates convergence in the long wavelength limit. Furthermore, $S^{(\mathrm{cT})\text{-ring}}(\mathbf{q})$ is shown to cancel the divergence of $S^{(\mathrm{T})}(\mathbf{q})$. For completeness, Fig. 3.6 also depicts $S^{(\mathrm{cT})\text{-rest}}(\mathbf{q})$, which includes all contributions to Eq. (3.16) that are not included in (T) or (cT)-ring, e.g., exchangelike terms. Our findings show that $S^{(\mathrm{cT})\text{-rest}}(\mathbf{q})$ converges to zero as $\mathbf{q} \to 0$. This demonstrates that the (cT) correlation energy expression averts the infrared catastrophe of the (T) approximation for the UEG without requiring an iterative solution of the triple amplitudes, as recently proposed in Ref. [69].

We summarize by presenting the complete (cT) equations, complementing Eq. (3.16). In addition, we provide the equations for (T), (cT)-ring, (cT)-rest as employed in the calculations. The following equation is applied across these methods:

$$M_{abc}^{ijk} = P_{ijk}^{abc} \left(t_{ij}^{ae} J_{ek}^{(X)bc} - t_{im}^{ab} J_{jk}^{(\mathrm{X})mc} \right), \tag{3.18}$$

with different definitions for $J^{(\mathrm{X})}$ where X denotes (T), (cT), (cT)-ring, and (cT)-rest as specified below. We note that $J^{(\mathrm{cT})\text{-rest}}$ is defined implicitly via,

$$J^{(\mathrm{T})} + J^{(\mathrm{cT})\text{-ring}} + J^{(\mathrm{cT})\text{-rest}} = J^{(\mathrm{cT})}. \tag{3.19}$$

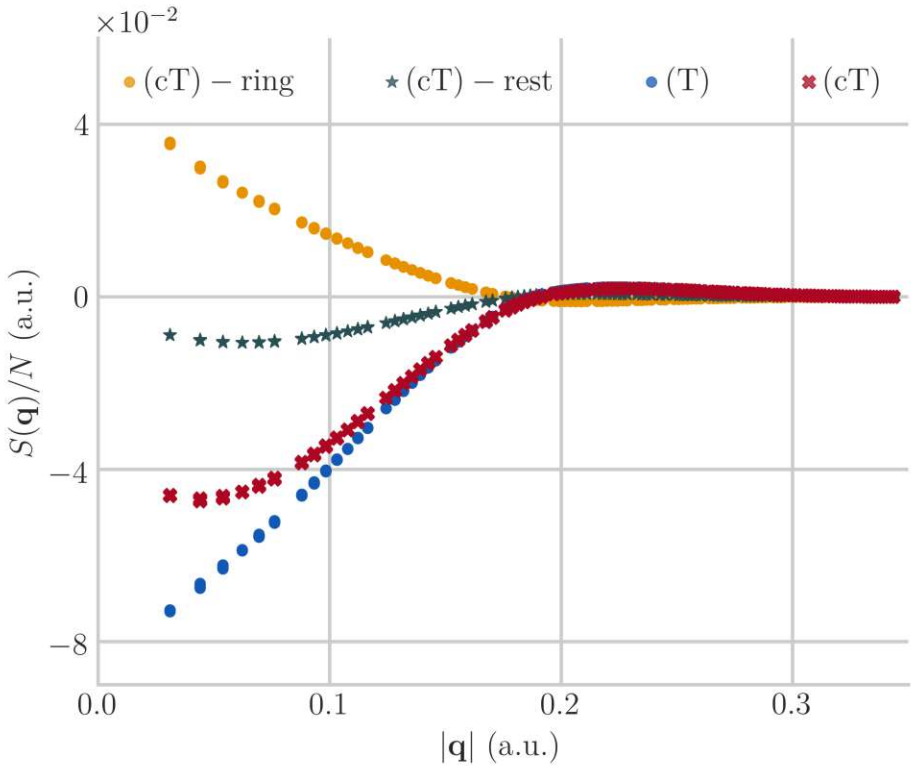

Figure 3.6: *UEG transition structure factor contributions of (T), (cT), (cT)-ring and (cT)-rest for 246 electrons with 2178 spatial orbitals, 166 twists and* $r_s = 20$ *a.u.*

The (T) method

In the (T) method, we use the following intermediates:

$$J^{bc}_{ek} = v^{bc}_{ek}, \tag{3.20}$$

$$J^{mc}_{jk} = v^{mc}_{jk}, \tag{3.21}$$

with the corresponding diagrammatic illustration having already being presented below Eq. (3.13).

The (cT)-ring terms

For the (cT)-ring terms, the following intermediates are employed:

$$J_{ek}^{bc} = 2v_{ef}^{bm} t_{mk}^{fc}, \tag{3.22}$$

$$J_{jk}^{mc} = 2v_{jf}^{mn} t_{nk}^{fc}, \tag{3.23}$$

where in combination with Eq. (3.18) we obtain the following diagrammatic depiction:

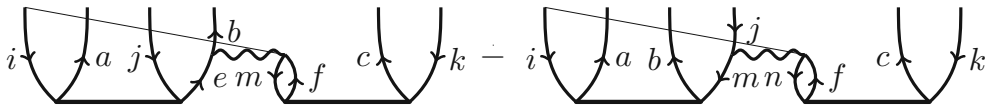

Finally, we conclude with,

The (cT) method

In the (cT) method, we utilize the following intermediates [12]:

$$\begin{aligned} J_{ek}^{bc} = {} & v_{ek}^{bc} + v_{ef}^{ab} t_k^f - (\chi_{ke}^{\prime mb} t_m^c + t_m^b \chi_{ek}^{\prime mc} + I_e^m t_{mk}^{bc}) \\ & + \left(2\chi_{ef}^{bm} t_{km}^{cf} - \chi_{ef}^{bm} t_{km}^{fc} - \chi_{fe}^{bm} t_{mk}^{fc} - t_{km}^{fb} \chi_{fe}^{cm}\right) + t_{mn}^{cb} \chi_{ke}^{mn}, \end{aligned} \tag{3.24}$$

$$\begin{aligned} J_{jk}^{mc} = {} & v_{jk}^{mc} - v_{jk}^{mn} t_n^c + \left(\chi_{jf}^{\prime\prime mc} t_k^f + t_j^f \chi_{fk}^{\prime\prime mc}\right) \\ & + \left(2\chi_{jf}^{mn} t_{kn}^{cf} - \chi_{jf}^{mn} t_{kn}^{fc} - \chi_{jf}^{nm} t_{nk}^{fc} - t_{nj}^{cf} \chi_{kf}^{nm}\right) + t_{kj}^{ef} \chi_{ef}^{cm}, \end{aligned} \tag{3.25}$$

$$\chi_{ke}^{\prime mb} = v_{ke}^{mb} - \frac{1}{2} v_{ke}^{mn} t_n^b + t_k^f \chi_{ef}^{\prime bm}, \tag{3.26}$$

$$\chi_{ef}^{\prime bm} = v_{ef}^{bm} - \frac{1}{2} t_n^b v_{ef}^{nm}, \tag{3.27}$$

$$\chi_{ek}^{\prime mc} = v_{ek}^{mc} - \frac{1}{2} v_{ek}^{mn} t_n^c + \chi_{fe}^{\prime cm} t_k^f, \tag{3.28}$$

$$I_c^m = f_c^m + \left(2v_{cf}^{mn} t_n^f - v_{fc}^{mn} t_n^f\right), \tag{3.29}$$

$$\chi_{ef}^{bm} = \chi_{ef}^{\prime bm} - \frac{1}{2} t_n^b v_{ef}^{nm}, \tag{3.30}$$

$$\chi_{ke}^{mn} = v_{ke}^{mn} + t_k^f v_{fe}^{mn}, \tag{3.31}$$

$$\chi_{jf}^{\prime\prime mc} = v_{jf}^{mc} - v_{jf}^{mn} t_n^c + \frac{1}{2} t_j^g \chi_{fg}^{cm}, \tag{3.32}$$

$$\chi_{fk}^{\prime\prime mc} = v_{fk}^{mc} - v_{fk}^{mn} t_n^c + \frac{1}{2} \chi_{gf}^{cm} t_k^g. \tag{3.33}$$

We note that providing a complete diagrammatic representation of the (cT) terms is tedious and unnecessary for the purposes of the present study.

3.7 Computational details

In this section, we provide details about the calculations performed on the UEG, a set of molecules, and metallic lithium. Furthermore, we present the numerical procedures employed to minimize errors arising from basis set incompleteness, and finite-size effects.

3.7.1 On the UEG calculations

All UEG calculations were conducted using *cc4ueg* [19]. For the structure factor results of MP2, rCCD, CCD, (T), and (cT) methods, approximately 18 virtual per occupied orbitals were used, with a total of 246 electrons. We selected a radius of $r_s = 20$ a.u. for our analysis, since the HF bandgap becomes smaller at lower densities, resulting to a minimum that appears at smaller system sizes. Nevertheless, as we have already demonstrated, the same behavior holds in the range of metallic densities between 1 a.u.-5 a.u.

To deduce the power-law behavior of the largest element of the t-amplitudes, and the minimum value of the $T_i(\mathbf{q})$ quantity for rCCD and CCD methods, we used 730 electrons, 18 virtual orbitals per occupied, and $r_s = 20$ a.u. as parameters. For bigger system sizes, the calculations were conducted only for rCCD theory.

Lastly, the system sizes employed for MP2, rCCD, CCD, (T), and (cT) correlation energies range from $N = 38$ electrons to 342 electrons and $r_s = 3$ a.u. All presented correlation energies have been extrapolated to the complete basis set (CBS) limit [70].

The numerical procedure for the decomposed contributions to rCCD and CCD methods follows the description outlined in Ref. [71]. Furthermore, we use twist averaging which helps to reduce the fluctuations owing to discretization errors within the finite simulation cell [35, 72, 73]. For small system sizes, 100-266 twists were used, while for the bigger system sizes, 40 twists were employed, as finite-size effects become less important approaching the thermodynamic limit.

3.7.2 On the molecular test set calculations

For these molecular calculations the Hartree–Fock ground state was obtained with the NWChem package [74] and interfaced to cc4s [75] as described in Ref. [76]. The testset used in this study was previously introduced in [56], where the Hartree–Fock and CCSD energies for the given molecules can be found. The geometries are available in the work of Knizia et al. [77].

3.7.3 On the metallic lithium calculations

To validate our theory, we consider metallic body-centered cubic (BCC) lithium. All calculations were performed using the Vienna Ab initio Simulation Package (VASP) [78] for HF and MP2 energies, as well as cc4s code [75] for coupled cluster energies. VASP is based on periodic boundary conditions and makes use of the projector augmented-wave (PAW) formalism [79]. We consider one valence electron per Li atom, using the PAW POTCAR file labeled as `Li_GW` and a plane-wave cutoff parameter of `ENCUT` = 141 eV.

For efficient coupled cluster calculations, a compression of the unoccupied HF manifold is achieved using natural orbitals (NOs) evaluated at the MP2 level of theory [80], while a low-rank decomposition is employed to compress the Coulomb integrals as described in Ref. [81].

Table 3.1: *CCSD+FPC energies with respect to the number of natural orbitals per occupied of Fig. 3.7(c).*

CCSD+FPC (Ha/atom)	#NOs/occupied
-0.026315	11
-0.026382	15
-0.026397	19
-0.026398	25

Both schemes introduce a controllable error which is kept well below 10^{-2} mHa for the low-rank decomposition of the Coulomb integrals, as it is shown in Tab.3.1. The basis-set error of the CCSD correlation contribution, as introduced by the restricted number of NOs, is converged to sub-mHa accuracy using a recently proposed focal-point correction scheme (here denoted as FPC) [56], as can be also observed in Fig. 3.7(c). For the (T) and (cT) correlation contributions, a relatively small number of 5 NOs per occupied orbital is used, corrected by an $1/N_{NO}$ extrapolation from 5 to 10 NOs using a simulation cell containing 26 Li atoms. This is sufficient, since the basis-set dependence of both (T) and (cT) is weak.

Furthermore, the core-valence contribution to the correlation energy is estimated by an all-electron PAW POTCAR file labeled as `Li_AE_GW`. In this case three electrons per Li atom are considered as valence electrons. Since the $1s^2$ HF orbitals are located about $-63\,\text{eV}$ below the Fermi level, we consider the MP2 method sufficient for this task. Here, a plane-wave cutoff of `ENCUT` $= 543\,\text{eV}$ is used. The individual contributions to the atomization energy of bulk bcc lithium are reported in the results section.

Fig. 3.7(a) and (b) depict the thermodynamic limit extrapolation of the HF and CCSD correlation energies of bulk bcc lithium. The corresponding numerical data is summarized in Tab.3.2. We observe that fitting the computed energies using the extrapolation law $(N_k N_{\text{atoms}})^{-2/3}$ enables a precise extrapolation. Here, N_k denotes the number of k-points used to sample the first Brillouin zone. We note that Brillouin zone sampling with more than one k-point is not yet supported in cc4s. Therefore all post-HF calculations employ $N_k = 1$ and large supercells with geometries given in Appendix C. However, twist-averaging is used to reduce the fluctuations due to discretization errors

of the finite simulation cells. The geometries and atomic structures of these cells are also given in Appendix(reference). The employed power law for the extrapolation to the limit $N \to \infty$ is well justified by the linear behaviour of the CCSD structure factor in the long wave length limit. However, this also implies that the system sizes included in such an extrapolation must be sufficiently large to sample short wavevectors in reciprocal space, where the structure factor approaches $\mathbf{q} \to 0$ linearly.

Table 3.2: *Total energies of the plots (a) and (b) of Fig. 3.7.*

$N_k N_{\text{atoms}}$	HF (Ha/atom)
216	-0.08344
343	-0.08280
512	-0.08237
729	-0.08210

$N_k N_{\text{atoms}}$	CCSD (Ha/atom)
26	-0.02463
44	-0.02633
68	-0.02727
128	-0.02841

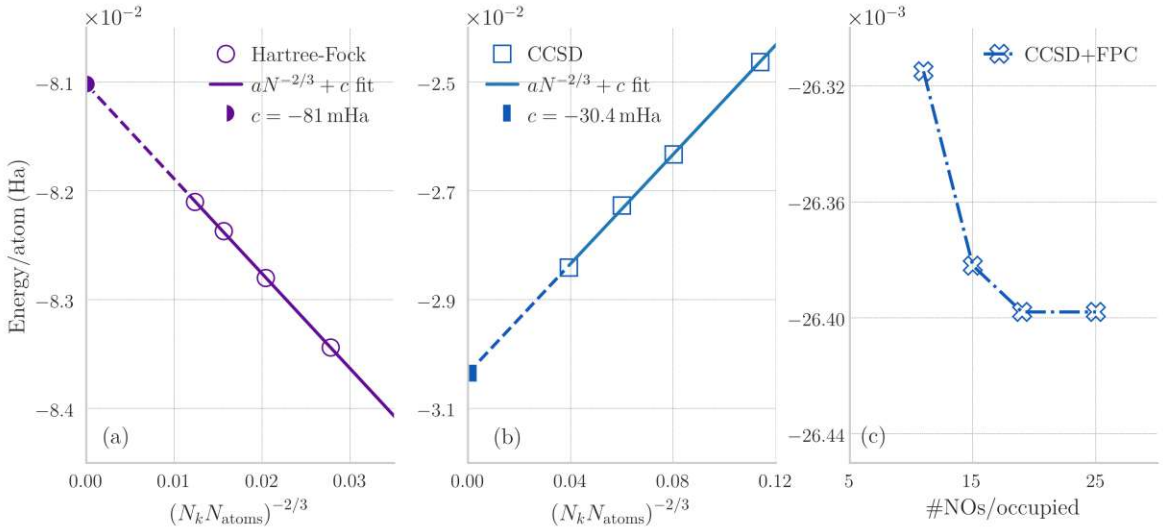

Figure 3.7: *(a) Thermodynamic limit convergence of the HF energy per atom. (b) Thermodynamic limit convergence of the CCSD correlation energy per atom. (c) Basis-set convergence of the CCSD correlation energy per atom using a simulation cell with 44 Li atoms and focal point correction.*

The extrapolation of the (cT) correlation energy contribution for lithium shown in Fig. 3.8(b) and (c), employs an $(N_{\text{atoms}})^{-2/3}$ fit and system sizes of 128 and 208 atoms. We observe, however, that the (cT) correlation energies obtained for smaller systems deviate from the employed extrapolation law. For this reason, we performed the analysis discussed in the Subs. 3.7.1 to estimate the remaining uncertainty in the thermodynamic limit extrapolation of the (cT) energy for bulk lithium. The computational data are given in Tab. 3.5.

3.8 Numerical results

We now turn to the discussion of numerical results for correlation energies obtained for electron gas simulation cells with various electron numbers at different levels of theory. Fig. 3.8(a) and (b) display the behavior of the correlation energy per electron as a function of $N^{-2/3}$ for MP2, rCCD, CCD, (T), and (cT).

The infrared catastrophe in MP2 theory becomes visible on approach to the TDL ($N \to \infty$) in Fig. 3.8(a). In contrast, rCCD and CCD correlation energies deviate considerably from the MP2 counterpart, converging as $N^{-2/3}$ to the TDL. In an analogous way, Fig. 3.8(b) verifies that the (T) correlation energy contribution also diverges as we move to the TDL, while its counterpart, (cT), exhibits a behavior that more closely resembles that of rCCD and CCD theories.

Table 3.3 summarizes correlation energies obtained from CCD, CCD(T), and CCD(cT) methods, compared to i-FCIQMC, DMC, and CCDT (CCD with full triple excitations) results. The energies were extrapolated to the CBS limit, and the systems were parameterized by a range of Wigner-Seitz radii ($r_s = 1, 2, 3, 5, 10$ a.u.) and $N = 14, 54$ electrons. We first discuss the results obtained for the 14-electron system. In this case, i-FCIQMC can be viewed as an exact reference, whereas CCDT serves as a reference for any approximate triples theory. The CCDT results from Ref. [59] are in good agreement with i-FCIQMC in the high density limit but differ at low densities. Higher levels of CC theory are needed to capture all important correlation effects as r_s increases [59]. CCD(T) and CCD(cT) correlation estimates are in good agreement with CCDT. We note that the agreement between CCD(T) and CCDT is fortuitous and only valid for small N, as can be seen from the divergence of CCD(T) as a function of N in Fig. 3.8(b).

We now discuss the results obtained for the 54-electron system summarized in Table 3.3. Here, we compare to DMC reference results. In this case, CCD(T) is fortuitously close to DMC, even at relatively low densities corresponding to $r_s = 10$ a.u. As can be seen from Fig. 3.8(a) and (b), this agreement is due to error cancellation between two effects. On the one hand, (T) overestimates long range correlation effects. On the other hand, higher-order cluster operators are missing in CCD(T), which underestimates correlation effects at lower densities. This error cancellation fails for larger electron numbers. CCD(cT) averts the infrared catastrophe and obtains accurate correlation energy results, compared to DMC, for all densities up to $r_s = 5$ a.u. Only at lower densities CCD(cT) starts to deviate significantly from DMC, due to the neglect of higher-order cluster operators.

Table 3.3: *CBS limit correlation energies per electron of the UEG in mHa. r_s is given in atomic units.*

	14 electrons				54 electrons			
Method	$r_s = 1$	$r_s = 2$	$r_s = 3$	$r_s = 5$	$r_s = 1$	$r_s = 2$	$r_s = 5$	$r_s = 10$
CCD	-36.7	-29.2	-24.2	-18.1	-38.4	-30.2	-18.5	-11.3
CCD(T)	-37.9	-31.5	-27.1	-21.4	-39.9	-33.1	-22.6	-15.0
CCD(cT)	-37.8	-31.3	-26.9	-21.1	-39.8	-32.8	-22.1	-14.5
CCDT [59]	-37.9	-31.5	-27.0	-21.2				
i-FCIQMC [82]	-38.0	-31.8	—	-21.9				
DMC [83]					-39.0	-32.6	-22.8	-15.6

As an important test, we apply CCSD(cT) theory to a set of molecules. Table 3.4 summarizes correlation energy contributions obtained using different triple particle-hole excitation approximations. In our benchmark, we use a set of 26 different molecules that provide access to 23 different closed-shell reaction energies. As a reference, we use energies from a converged CCSDT calculation. The standard deviation of the reaction energy for the 23 reactions is 0.9 kJ/mol for both CCSD(T) and CCSD(cT) (the maximum error is 2.1 and 3.3 kJ/mol for CCSD(T) and CCSD(cT), respectively). This illustrates that both CCSD(T) and CCSD(cT) are very accurate approximations for the full CCSDT energy.

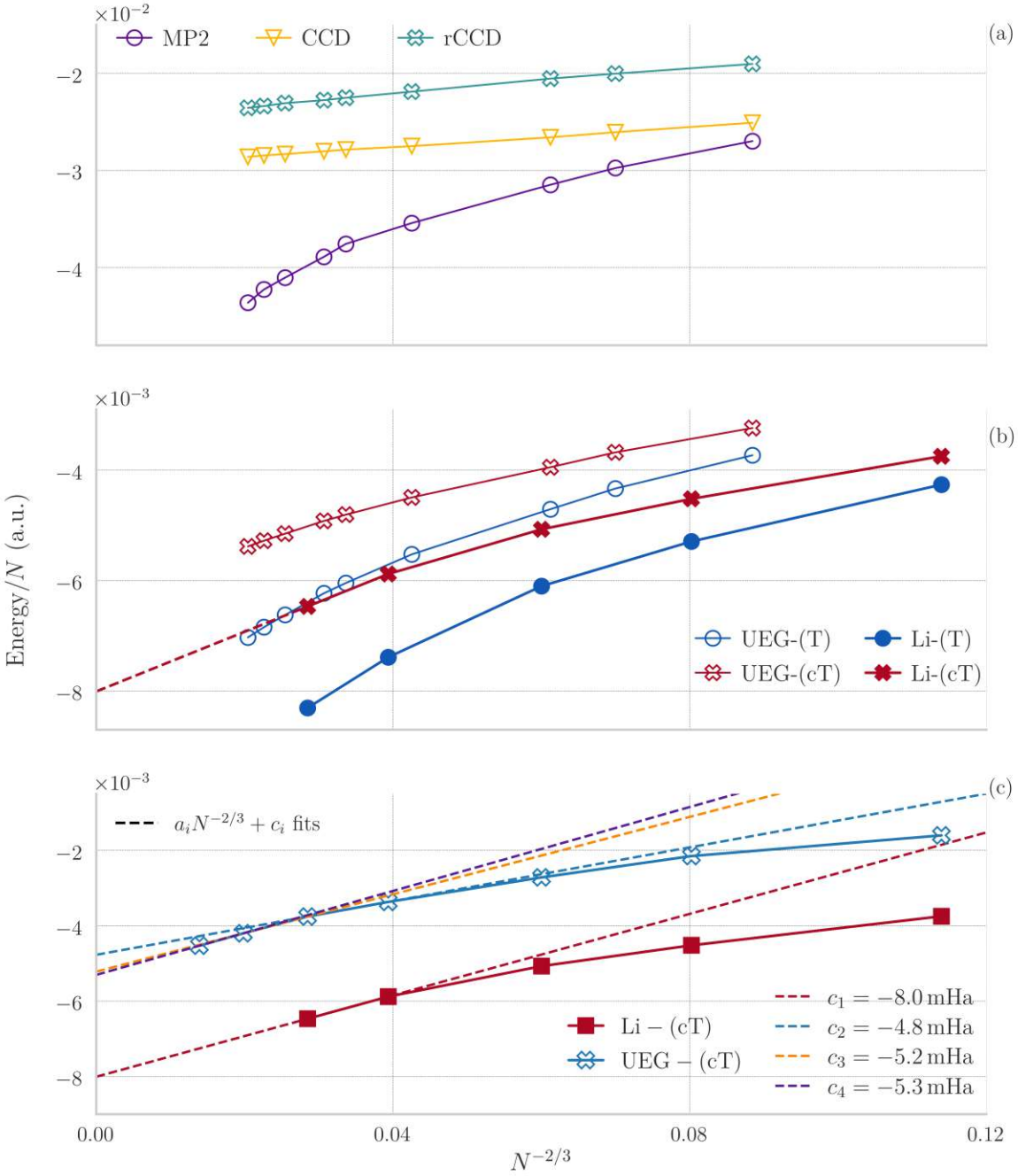

Figure 3.8: *Correlation energies for (a) UEG and MP2, rCCD, and CCD methods. (b) (T) and (cT) for UEG and metallic lithium. (c) TDL exctrapolation of (cT) for the UEG and metallic lithium, showing the remaining uncertainty in our estimate.*

Table 3.4: *Triple particle-hole excitation correlation energy contributions calculated with an aug-cc-pVTZ basis set. (T) and (cT) are computed using a one-shot approach, as has been previously described. The energy for the full T, given in the last column, is evaluated by* $E_T = E(CCSDT) - E(CCSD)$*. All energies in atomic units.*

Molecules	(T)	(cT)	T
C2H2	-0.01709	-0.01575	-0.01709
C2H4	-0.01550	-0.01440	-0.01588
CH3Cl	-0.01657	-0.01537	-0.01728
CH3OH	-0.01587	-0.01471	-0.01613
CH3SH	-0.01663	-0.01547	-0.01745
CH4	-0.00653	-0.00616	-0.00693
CO	-0.01789	-0.01642	-0.01800
CO2	-0.03031	-0.02769	-0.03001
CS2	-0.03663	-0.03330	-0.03702
Cl2	-0.01952	-0.01802	-0.02046
ClF	-0.01867	-0.01727	-0.01924
F2	-0.01966	-0.01818	-0.01967
H2	0.00000	0.00000	0.00000
H2O	-0.00867	-0.00805	-0.00874
H2O2	-0.02022	-0.01861	-0.02018
H2S	-0.00867	-0.00814	-0.00941
HCHO	-0.01757	-0.01620	-0.01771
HCN	-0.01889	-0.01732	-0.01867
HCOOH	-0.02799	-0.02569	-0.02795
HCl	-0.00876	-0.00816	-0.00933
HF	-0.00755	-0.00702	-0.00758
HNCO	-0.03044	-0.02783	-0.03027
N2	-0.01981	-0.01810	-0.01944
N2H4	-0.01760	-0.01627	-0.01776
NH3	-0.00833	-0.00777	-0.00854
SO2	-0.03679	-0.03346	-0.03645

Moreover, we present results for the lithium bcc metal. We find that CCSD(cT) predicts a cohesive energy of 60.1 mHa/atom in excellent agreement with the experimental estimate of 60.9 mHa/atom corrected for zero-point vibrations [84]. Our estimate includes a HF, CCSD, (cT) and core-valence MP2 contribution of 20.5, 30.4, 8, and 1.2 mHa/atom, respectively. The computational details have already been discussed previously. Fig. 3.8(b) and (c) depicts the (cT) correlation energy convergence. Although our CCSD estimate of the cohesion energy is in good agreement with results from Ref. [69], we note that our triples estimate is about 3 mHa/atom larger. Tab. 3.5 summarizes the numerical data of (cT) correlation energies for the UEG at a density corresponding to r_s=3.2 for a range of electron numbers. This density and the employed basis set sizes are identical to those used in the calculations for lithium. Our findings indicate that the difference between thermodynamic limit extrapolations employing the $(N)^{-2/3}$ fits and system sizes corresponding to 358-610 electrons and 128-208 electrons deviates by less than 0.5 mHa/electron, as it is depicted in Fig. 3.8(c). Furthermore, the extrapolated estimates using 358-610 electrons and 208-358 electrons correspond to -5.2 mHa/electron and -5.3 mHa/electron, deviating by less than 0.1 mHa/electron. From this, we assess that the remaining uncertainty in our estimate of the (cT) contribution to the lithium cohesive energy, obtained from extrapolations using 128 and 208 atoms, is below 1 mHa/atom.

Table 3.5: *Correlation energies contributions at the level of (cT) to the UEG and the atomization energy of Li as depicted in Fig. 3.8(c). All energies in mHa per electron.*

N_{elect}	UEG-(cT)	Li-(cT)
26	-1.60	-3.75
44	-2.15	-4.52
68	-2.72	-5.07
128	-3.37	-5.88
208	-3.76	-6.47
358	-4.20	—
610	-4.53	—

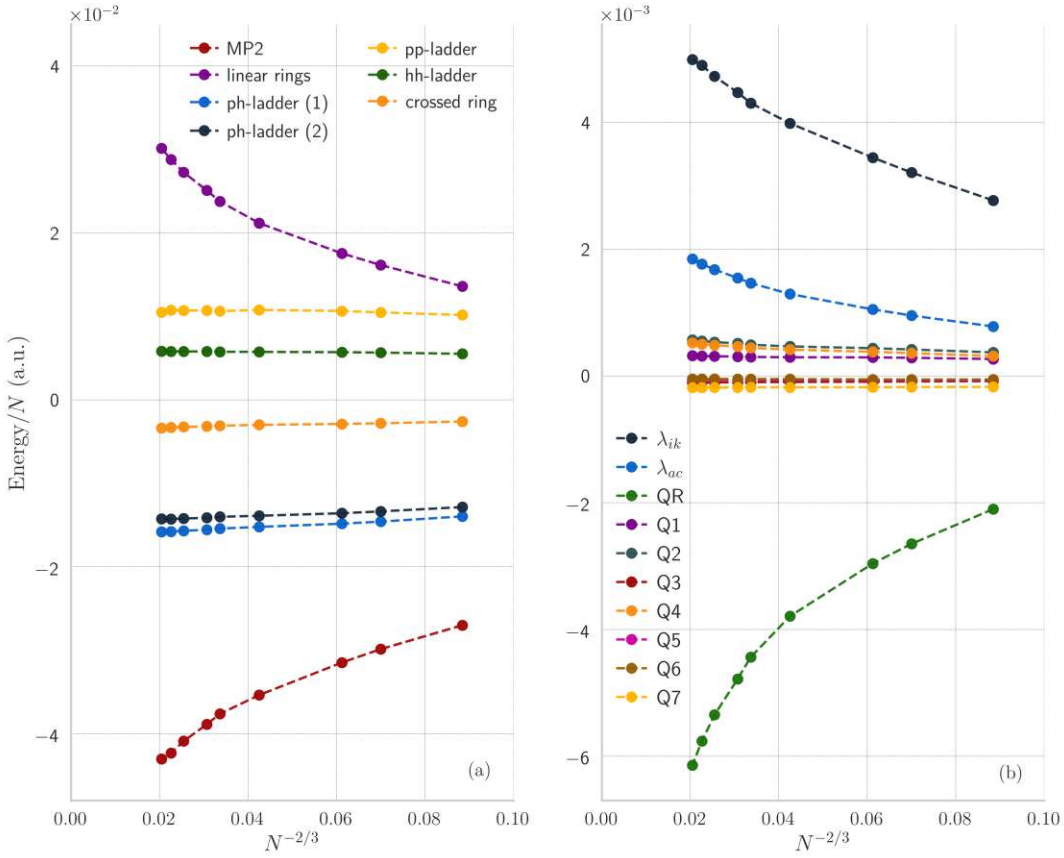

Figure 3.9: *Decomposed correlation energies of the terms appear in CCD amplitude equation (2.30) on approach to the TDL with electron numbers $N = 38 - 342$, $r_s = 3$ a.u., and extrapolated to the CBS limit. (a) Linear and (b) quadratic terms in t.*

Finally, we present a full decomposition of the correlation energy and transition structure factor contributions for all terms at the CCD level of theory. As observed in Fig. 3.9(a) and Fig. 3.10(a), the only terms yielding divergent energies, while approaching the TDL, and transition structure factors are the MP2 and linear ring terms. In contrast, the remaining terms, linear in t, already exhibit convergent energies for increasing system sizes, resembling behaviors similar to rCCD and CCD as shown in Fig. 3.8(a). The convergent behavior of the correlation energies can be further confirmed by the transition structure factors results, shown in Fig. 3.10(b).

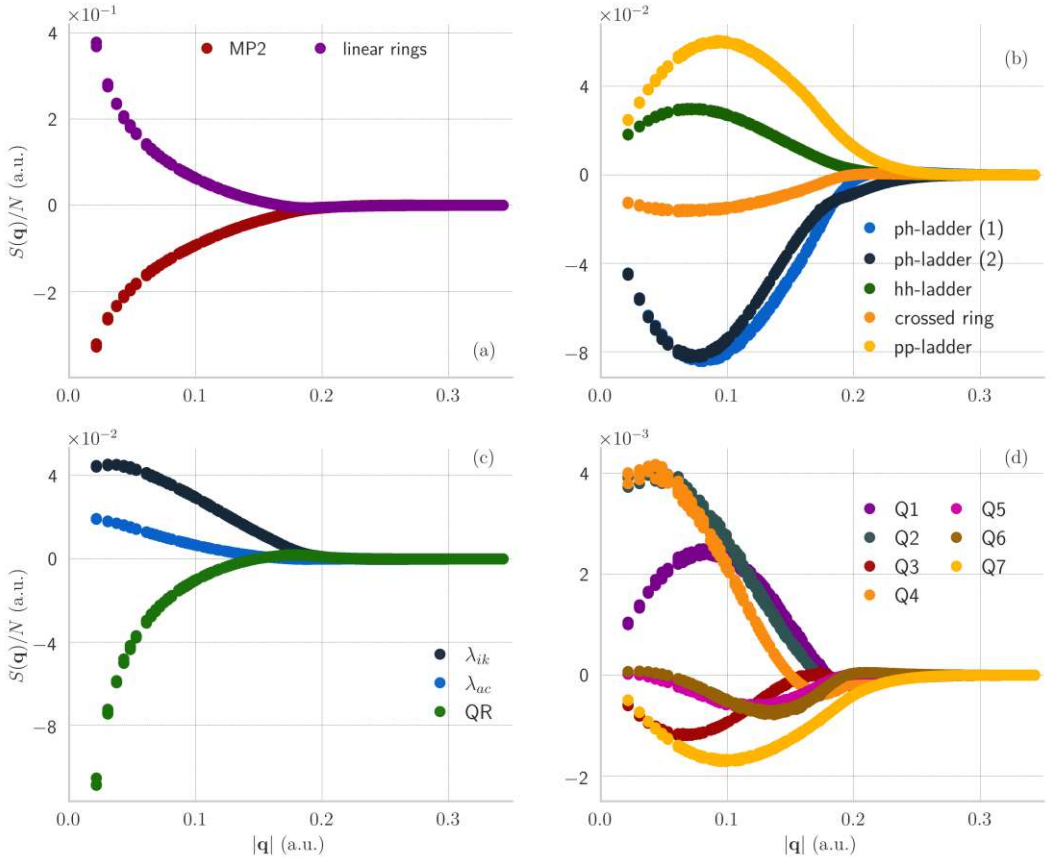

Figure 3.10: *Decomposed transition structure factors of the terms appear in CCD amplitude equation (2.30) for $N = 730$, $r_s = 20$ a.u., and 6.254 spatial orbitals. (a) and (b) linear terms in t. (c) and (d) quadratic terms in t.*

Regarding the quadratic terms in t, the quadratic ring behaves similarly to MP2 and the linear ring terms. In addition, we note that L_{ik} and L_{ac} seem also to diverge in the long wavelength limit. However, this artifact appears due to the slow convergence of these two terms in the TDL. Performing calculations for larger system sizes confirms that these terms yield convergent transition structure factors, as depicted in Fig. 3.10(c), leading to convergent correlation energies. The remaining quadratic terms in t demonstrate, in Fig. 3.8(b) and Fig. 3.10(d), a convergent behavior of energies and transition structure factors. This aligns with our findings that the rings are the only

terms with the leading-order contribution to the CCD correlation energy in the long wavelength limit. Consequently, this results in identical convergence as $\mathbf{q}$ approaches 0, between rCCD and CCD methods.

3.9 Summary and conclusions

In this chapter, we introduced a highly accurate and computationally efficient theory, denoted as CCSD(cT), which paves the way for achieving chemical accuracy in *ab initio* calculations of real metals. Initially, guided by the infrared catastrophe of the MP2 correlation energy, when applied to these systems, we conducted a thorough analysis by decomposing the correlation energies, transition structure factors, and amplitudes at the CCD level of theory.

For the uniform electron gas (UEG) model, a combination of analytical proofs and numerical indications has led us to the conclusion that the divergence in second-order perturbation theory can be averted by carefully including higher-order contributions from the many-electron perturbation expansion, specifically corresponding to ring diagrams. These ring-type diagrams, also included in the widely-used RPA, exhibit the leading-order contribution in the long-wavelength limit, compared to the other non-diverging terms in the CCD theory. This inclusion results in convergent correlation energies in both rCCD and CCD methods.

Based on these findings, we numerically demonstrated the divergence of the CCD(T) method when applied to the UEG. Subsequently, from the aforementioned analysis, it was straightforward to identify terms present in a full inclusion of triple excitations that are essential for averting the infrared catastrophe of the CCD(T) approximation. The CCD(cT) method, which incorporates these terms in a perturbative manner, yields convergent correlation energies when applied to the UEG.

When applied to molecular systems, CCSD(cT) retains all the desirable properties of CCSD(T), such as high chemical accuracy and low computational cost ($\mathcal{O}(N^7)$), compared to the full inclusion of triples in CCSDT ($\mathcal{O}(N^8)$). We conducted signifi-

cant tests, comparing CCD(cT) with CCDT, i-FCIQMC, and DMC results at metallic densities, where CCD(T) exhibits good agreement.

Finally, we utilized the CCSD(cT) method to calculate the cohesive energy of metallic lithium, finding excellent agreement with experimental estimates. Although our approach focused on paramagnetic systems, it can be generalized to ferromagnetic systems using an unrestricted formalism.

Several far-reaching conclusions emerge from this work. Since, the RPA in the electron gas is formally identical to CCSD in the long-wavelength limit, embedding CCSD into the RPA presents a promising approach for metals [85, 86]. Furthermore, our work could explain (part of) the discrepancies observed between DMC and CCSD(T) interaction energies of large molecules [87].

Chapter 4

Unveiling coupled-cluster theories convergence on approach to the complete basis set limit

The following chapter is a modification of the work in preparation found in [88].

The ongoing and final chapter is dedicated to investigating the convergence of coupled-cluster correlation energies and related quantities with respect to the employed basis set size for the uniform electron gas. Our aim is to gain a better understanding of the basis set incompleteness error (BSIE). To this end, coupled-cluster doubles (CCD) theory is applied to the three dimensional uniform electron gas for a range of densities, basis set sizes and electron numbers. We provide a thorough analysis of individual, diagrammatically decomposed contributions to the amplitudes at the CCD theory level. In particular, numerical results indicate that only two terms from the amplitude equations contribute to the asymptotic large momentum behavior of the transition structure

factor, corresponding to the cusp region at short interelectronic distances or short-range regime. However, due to the coupling present in the amplitude equations, all decomposed correlation energy contributions exhibit the same asymptotic convergence behavior toward the complete basis set limit. These findings offer an additional rationale for the success of a recently proposed correction to the basis set incompleteness error of coupled-cluster theory. Finally, we examine the BSIE in the coupled-cluster doubles plus perturbative triples [CCD(T)] method, as well as in the newly proposed coupled-cluster doubles plus complete perturbative triples [CCD(cT)] method.

4.1 CBS limit: a vital component for achieving chemical accuracy

Coupled-cluster (CC) theories find wide application in molecular quantum chemistry and are becoming increasingly popular for studying solid state systems. They approximate the true many-electron wavefunction in a systematically improvable manner by employing an exponential ansatz with a series of higher-order particle-hole excitation operators. While systems exhibiting strong electronic correlation effects require high-order excitation operators, those with strong single-reference character can be well described using low-order excitation operators [49]. Specifically, at the truncation level of single, double, and perturbative triple particle–hole excitation operators, CCSD(T) theory predicts atomization and reaction energies for a large number of molecules with an accuracy of approximately 1 kcal/mol [49]. Although the computational cost of CCSD(T) theory is significantly higher than that of the more widely used approximate density functional theory (DFT) calculations, recent methodological developments enable the study of relatively complex systems, such as, molecules adsorbed on surfaces [89, 90, 91, 92, 93, 94, 86, 95, 96]. However, achieving high accuracy compared to the experiment is only possible if the ansatz is fully converged with respect to all computational parameters that model the true physical system. These parameters include the number of atoms used to model an infinitely large periodic crystal and the truncation parameter of the basis set. Any truncation of the employed

one-electron basis set introduces a basis set incompleteness error (BSIE) in CC and related theories.

This chapter aims to conduct a detailed investigation of the BSIE in CCSD and CCSD(T) methods using a plane wave basis set. For a better understanding of the corresponding BSIE, we employ the uniform electron gas (UEG) model Hamiltonian, which includes a kinetic energy operator, an electronic Coulomb interaction and a constant background potential to preserve charge neutrality. The UEG model depends only on parameters with well defined physical interpretations: (i) the electronic density, (ii) the number of electrons and the cell shape, and (iii) a momentum cutoff defining the employed basis set. The electronic density controls the relative importance of the kinetic energy operator compared to the Coulomb interaction. In this manner, one can continuously transform the system from a weakly correlated system at high densities to a strongly correlated system at low densities. The number of electrons and the cell shape used to model the electron gas at a fixed density allow for the investigation of finite size effects [11, 43]. Because of the translational symmetry of the UEG model Hamiltonian, the mean-field orbital solutions correspond to plane waves characterized by a wavevector. The momentum cutoff enables a systematic truncation of the employed plane wave basis, making the UEG ideally suited for studying BSIEs of electronic structure theories [82, 97, 98].

In this chapter, our primary focus is on the BSIEs introduced by large cutoff momenta compared to the Fermi momentum of the UEG. While the Fermi sphere defines a complete plane wave basis set necessary for representing the mean-field ground state wave function, a considerably larger basis set is required for the representation of correlated wave functions. Specifically, at the point where two electrons coalesce, the exact correlated wave function exhibits a cusp [99, 100, 101]. Consequently, a large number of one-electron orbitals are needed to describe this feature with sufficient accuracy. In addition to increasing the one-electron basis set, it is also possible to account for the cusp in the wavefunction and derived properties directly by adding basis functions explicitly depending on two electronic coordinates. Various techniques have been developed to accelerate the slow convergence to the complete basis set limit, including explicitly correlated methods [102, 103, 40, 104, 105], transcorrelated meth-

ods [106, 107, 108, 109, 110], or basis-set extrapolation techniques [111]. These methods are primarily used for molecular calculations.

Recently, a finite basis set correction for the coupled cluster singles and doubles method, based on a diagrammatic decomposition of the correlation energy was proposed [56]. The findings in [56] revealed that the finite basis set error is dominated by two contributions to the CCSD correlation energies—specifically, the second-order energy and a term referred to as the particle-particle ladder (PPL) term [41]. In Ref. [56] we examined the accuracy of various approximate corrections to the basis set incompleteness error in the particle-particle ladder term. Here, we present a more detailed analysis of the correlation energy contributions that can be obtained from a diagrammatic decomposition of the CCSD correlation energy. We also investigate other related quantities as functions of the basis set size, electron number, and electronic density. This investigation enables us to determine the next-to-leading-order contributions to the basis set error in the UEG.

Our diagrammatic decomposition approach is partly motivated by prominent examples that sum up particular contributions in the perturbation series to infinite order. Famous examples include the resummation of ring-type contributions, as demonstrated in the random phase approximation (RPA) [112], and ladder theory (LT) [113, 114], which contains PPL contributions. Interestingly, CCSD already contains all diagrams appearing in RPA *and* LT, as well as many further contributions beyond that. This feature alone makes CCSD intriguing as both, RPA and LT, are known to have prominent failures. The RPA lacks an accurate description of short-range electronic correlation. In medium density systems, the pair-correlation function becomes negative for vanishing interelectronic distances [115]. On the other hand, the RPA is known for providing an accurate description in the long-range regime [62]. In contrast, short-range electron correlation can be properly described by LT [116]. However, in the particular case of systems with long-range Coulomb interactions, LT was found to be unsatisfactory [117].

4.2 Adjusting theoretical features at the CBS limit

4.2.1 A Uniform Electron Gas revision

In this section, we will recapitulate the essential theoretical elements presented in the preceding chapters, which will be utilized for our study. Our analysis is restricted to the Uniform Electron Gas (UEG) model, as outlined in Secs. (2.1) and (2.2), with N electrons enclosed in a finite cubic simulation cell under periodic boundary conditions. The volume of the simulation box is determined by the electron number N and the density parameter r_s [118].

As previously mentioned for the UEG, plane waves–see Eq. (2.13)–are solutions of the Hartree-Fock Hamiltonian, where the wave vectors denote reciprocal lattice vectors of the simulation cell. We specifically consider the paramagnetic case, where each spatial orbital is occupied by two electrons with opposite spins. Therefore, the number of occupied states, denoted as N_o, is half the total number of electrons N. Additionally, throughout this study, we employ Hartree atomic units. The expressions for the corresponding HF eigenenergies for the occupied and unoccupied orbitals can be found in Eqs. (2.18) and (2.19), respectively. The two-electron Coulomb integrals appearing in these equations are given by:

$$v_{rs}^{pq} = v(\mathbf{q})\delta_{\mathbf{k}_r-\mathbf{k}_p,\mathbf{k}_q-\mathbf{k}_s} = \frac{4\pi}{\Omega \mathbf{q}^2}\,\delta_{\mathbf{k}_r-\mathbf{k}_p,\mathbf{k}_q-\mathbf{k}_s}, \tag{4.1}$$

where $\mathbf{q} = \mathbf{k}_p - \mathbf{k}_r$ is the momentum transfer vector. At $\mathbf{q} = 0$ the Coulomb interaction exhibits a singularity. However, this singularity is integrable and various techniques exist to resolve it (see Ref. [119] and references therein). In this work we employ the regularization as described by Frazer et al. [18]. An important characteristic of the UEG is the conservation of momentum. As evident from Eq. (4.1), Coulomb integrals are non-zero only if the momentum transferred by the left indices of the tensor v_{rs}^{pq} is identical to the negative momentum of the indices on the right.

For sufficiently large densities, as employed in this work, the Hartree-Fock (HF) orbital energies are strictly ordered based on the length of the corresponding wave vector.

Throughout this chapter, we use the following index labels:

i, j, k, ...	occupied states,
a, b, c, ...	virtual states in finite basis,
α, β, γ, ...	virtual states beyond finite basis set
	referred to as *augmented virtual states*.

The separation between occupied and unoccupied orbitals is denoted by the Fermi wave vector, k_F, representing the momentum of the occupied orbital with the highest eigenenergy. In the UEG, owing to the symmetry of the model, the sphere of radius k_F that contains all the occupied states is referred to as Fermi sphere.

The amount of virtual states, labeled as N_v, is determined by a plane-wave cutoff momentum k_cut, typically much larger than k_F. The number of virtual states N_v, found between the spheres with radii k_cut and k_F is proportional to k_cut^3 [82]. It's important to emphasize that in the UEG, the orbitals remain unchanged if the number of virtual orbitals is altered (cf. the generalized Brillouin condition in explicit correlated methods [40]).

We refer to the infinite number of plane waves with momentum exceeding k_cut in magnitude as *augmented virtual states*. These states are considered theoretically only to better understand and investigate BSIEs of central quantities and various contributions to the correlation energy. Consequently, contributions such as Coulomb integrals appear, involving one state from the virtual states in the finite basis and another state from the augmented basis set, denoted as $v_{ij}^{a\beta}$. For a given choice of a and i, momentum conservation dictates that the number of non-zero choices for β and consequently j is less than the number of occupied states N_o. Thus, these contributions will be negligible in the limit of an infinitely large basis set. For an illustration of the aforementioned discussion, the reader can refer to Fig. 2.1.

4.2.2 Coupled-cluster doubles theory

In this work we employ a Hartree-Fock single-reference coupled-cluster theory to approximate electronic correlation effects. As we have already explained, since all single

excitations are zero [71] in the UEG, the lowest non-zero order coupled-cluster ansatz is CCD, only including double excitations. The corresponding amplitudes t_{ij}^{ab}, are obtained from the following amplitude equation:

$$\begin{aligned}
\underbrace{(\epsilon_i + \epsilon_j - \epsilon_a - \epsilon_b)}_{\Delta_{ij}^{ab}} t_{ij}^{ab} = {} & \underbrace{v_{ij}^{ab}}_{\text{MP2}} + \underbrace{2v_{ic}^{ak}t_{kj}^{cb} + 2t_{ik}^{ac}v_{cj}^{kb}}_{\text{linear rings}} + \underbrace{P\, 2t_{ik}^{ac}v_{cd}^{kl}t_{lj}^{db}}_{\text{quadratic ring}} - \underbrace{P\, v_{ic}^{ak}t_{kj}^{bc}}_{\text{crossed-ring}} \\
& + \underbrace{v_{ab}^{cd}t_{ij}^{cd}}_{\text{pp-ladder}} + \underbrace{v_{ij}^{kl}t_{kl}^{ab}}_{\text{hh-ladder}} \underbrace{- P\,(t_{ik}^{ac}v_{cj}^{bk} + t_{ik}^{cb}v_{cj}^{ak})}_{\text{ph-ladders}} \\
& \underbrace{- P\, t_{ij}^{cb}w_{dc}^{lk}t_{lk}^{da}}_{\lambda_{ik}} \underbrace{+ P\, t_{kj}^{ab}w_{dc}^{lk}t_{li}^{dc}}_{\lambda_{ac}} \underbrace{- P\, t_{il}^{ac}v_{cd}^{kl}t_{kj}^{db}}_{\text{Q1}} \\
& \underbrace{- P\, t_{il}^{da}v_{dc}^{lk}t_{kj}^{cb}}_{\text{Q2}} \underbrace{+ P\, \frac{1}{2}\, t_{il}^{db}v_{cd}^{lk}t_{kj}^{ac}}_{\text{Q3}} \\
& \underbrace{- P\, \frac{1}{2}\, t_{il}^{ad}w_{dc}^{lk}t_{kj}^{bc}}_{\text{Q4}} \underbrace{+ P\, \frac{1}{2}\, t_{il}^{da}v_{dc}^{lk}t_{kj}^{bc}}_{\text{Q5}} \\
& \underbrace{+ P\, \frac{1}{2}\, t_{il}^{da}v_{cd}^{lk}t_{kj}^{cb}}_{\text{Q6}} + \underbrace{t_{kl}^{ab}v_{cd}^{kl}t_{ij}^{cd}}_{\text{Q7}},
\end{aligned} \tag{4.2}$$

with $P\{\dots\}_{ij}^{ab} = \{\dots\}_{ij}^{ab} + \{\dots\}_{ji}^{ba}$. The two-electron Coulomb integrals w_{ij}^{ab} are defined as $w_{ij}^{ab} = 2v_{ij}^{ab} - v_{ji}^{ab}$. Regarding the terms in Eq. (4.2) containing these integrals, we will label the first term as *direct-(d)* and the second as *exchange-(ex)*, denoted, for instance, as $Q4(d)$ and $Q4(ex)$. The Δ_{ij}^{ab} (and later Δ_{ijk}^{abc}) terms involve the HF eigenenergies and are defined as:

$$\Delta_{i\dots}^{a\dots} = \varepsilon_i - \varepsilon_a + \dots\ . \tag{4.3}$$

The amplitude equation is solved iteratively until a self-consistent solution for the amplitudes t_{ij}^{ab} is found. The converged amplitudes can then be used to evaluate the energy contribution beyond the HF energy, the so-called correlation energy:

$$E_{\mathrm{c}}^{\mathrm{D}}(t) = \sum_{ijab} v_{ab}^{ij}\left(2t_{ij}^{ab} - t_{ji}^{ab}\right). \tag{4.4}$$

We want to point out the well-known connection between second-order (MP2), third-order (MP3), and fourth-order (MP4) Møller–Plesset perturbation theory, and CCSD.

Using only the first term on the right-hand-side of Eq. (4.2), one retrieves the MP2 amplitudes, denoted by:

$$t^{(1)}{}_{ij}^{ab} = \frac{v_{ij}^{ab}}{\Delta_{ij}^{ab}}. \tag{4.5}$$

Evaluating Eq. (4.4) with these amplitudes one obtains the MP2 correlation energy. We stress that for the UEG each element of the MP2 amplitudes is entirely described by the HF eigenenergies and the Coulomb integral. Consequently, the elements of $t^{(1)}{}_{ij}^{ab}$ will remain unchanged as the basis set size increases. The equation for the MP3 amplitudes $t^{(2)}$ can also be inferred directly from Eq. (4.2) by substituting $t^{(2)}$ for t on the left-hand-side and $t^{(1)}$ for t for all contributions on the right-hand-side that are linear in t, while disregarding the terms that are quadratic. Evaluating Eq. (4.4) with $t^{(2)}$ yields the MP3 correlation energy. To obtain part of the MP4 correlation energy, one can follow the same procedure by considering the terms that are quadratic in t and disregarding the linear in t terms. It's important to note that the MP2, MP3 and MP4 correlation energies per electron diverge in the thermodynamic limit $N \to \infty$ [11]. However, in the present case, we employ a simulation cell with a finite number of electrons, where finite order perturbation theories also yield finite correlation energies.

4.2.3 Triple particle-hole excitations

The natural extension of CCSD would be the full inclusion of triple particle-hole excitation operators, denoted as CCSDT. This requires the solution of the corresponding amplitude equations for t_{ijk}^{abc}. However, the storage requirements of these additional terms is $N_\mathrm{o}^3 N_\mathrm{v}^3$, which makes the approach impractical for larger system sizes. Hence, approximate CCSDT models have been investigated early on [120, 121, 122, 123]. In today's calculations, one of the most widely used methods is the CCSD(T) [124] approach. In the previous chapter, a modified variant, known as the CCSD(cT) method [125], has been proposed. This approximation includes additional terms beyond the CCSD(T) method, providing a non-diverging description of zero-gap materials in the thermodynamic limit. As single excitations are absent in the UEG system, we introduce the CCD(T) and CCD(cT) method. The correlation energy beyond E_c^D for these methods

is given by:

$$E_{\mathrm{c}}^{(\mathrm{T})} = \sum_{ijk} \sum_{abc} \left(\overline{W}_{ijk}^{abc} + \overline{W}_{ikj}^{acb} + \overline{W}_{kji}^{cba} + \overline{W}_{jik}^{bac} + \overline{W}_{jki}^{bca} + \overline{W}_{kij}^{cab} \right) A_{abc}^{ijk}, \tag{4.6}$$

with

$$W_{ijk}^{abc} = \sum_{e} t_{ij}^{ae} v_{ek}^{bc} - \sum_{m} t_{im}^{ab} v_{jk}^{mc}, \tag{4.7}$$

where we define for any six-index quantity x_{ijk}^{abc}:

$$\overline{x}_{ijk}^{abc} = 8x_{ijk}^{abc} - 4x_{ijk}^{acb} - 4x_{ijk}^{cba} - 4x_{ijk}^{bac} + 2x_{ijk}^{bca} + 2x_{ijk}^{cab}. \tag{4.8}$$

Furthermore, the quantity A for the (T) model is given by:

$$A_{abc}^{ijk} = \frac{W_{abc}^{ijk}}{\Delta_{abc}^{ijk}}. \tag{4.9}$$

In (cT), A_{abc}^{ijk} contains further terms beyond those defined in Eq. (4.7). The full set of equations for this method is given in Ref. [125]. Here, we provide the terms excluding all singles contributions. Instead of W_{ijk}^{abc} as defined in Eq. (4.7), $W_{ijk}^{'abc}$ is used to construct A_{abc}^{ijk}, which is defined as:

$$W_{abc}^{'ijk} = \sum_{e} t_{ij}^{ae} J_{ek}^{bc} - \sum_{m} t_{im}^{ab} J_{jk}^{mc}, \tag{4.10}$$

with

$$J_{ek}^{bc} = v_{ek}^{bc} + \sum_{mn} t_{mn}^{cb} v_{ke}^{mn} + \sum_{mf} \left(2v_{ef}^{bm} t_{km}^{cf} - v_{ef}^{bm} t_{km}^{fc} - v_{fe}^{bm} t_{mk}^{fc} - t_{km}^{fb} v_{fe}^{cm} \right), \tag{4.11}$$

$$J_{jk}^{mc} = v_{jk}^{mc} + \sum_{ef} t_{kj}^{ef} v_{ef}^{cm} + \sum_{nf} \left(2v_{jf}^{mn} t_{kn}^{cf} - v_{jf}^{mn} t_{kn}^{fc} - v_{jf}^{nm} t_{nk}^{fc} - t_{nj}^{cf} v_{kf}^{nm} \right). \tag{4.12}$$

We emphasize that the large benefit of both approaches is the inclusion of triply excited clusters without storing an intermediate quantity of the size $N_{\mathrm{v}}^3 N_{\mathrm{o}}^3$. Nevertheless, the memory footprint of (cT) is roughly doubled compared to the (T) approach. This is because J_{ek}^{bc} is typically computed once and stored in memory. The computational cost for the evaluation of J_{ek}^{bc} and J_{jk}^{mc} is negligible compared to the contractions in Eqs. (4.7) and (4.10). Still, the total number of operations in (cT) is approximately twice that of the operations in a (T) calculation. In (T), we need to evaluate Eq. (4.7), which represents the rate determining contraction scaling as $\mathcal{O}(N^7)$. On the other hand, for (cT), one has to evaluate both the contractions in Eq. (4.7) and that in Eq. (4.10).

4.2.4 Static structure factor

The static structure factor holds a pivotal role in periodic electronic structure theory [68]. In coupled-cluster approaches, a related quantity, known as the transition structure factor S, has been utilized in recent works [67, 35, 66]. The structure factor is directly linked to the correlation energy contribution at a specific momentum transfer q, as expressed by the following equation:

$$E_{\mathrm{c}} = \sum_{q} v(q) S(q). \tag{4.13}$$

For energy expressions in the form of Eq. (4.4), the transition structure factor can be written as:

$$S(q) = \sum_{ijab} \left(2t_{ij}^{ab} - t_{ji}^{ab}\right) \delta_{q,k_a-k_i} \delta_{q,k_j-k_b}, \tag{4.14}$$

where the amplitudes t_{ij}^{ab} have been obtained from calculations with a finite virtual basis set. In passing we note that the Fourier transform of $S(q)$ leads to the so-called transition pair-correlation function.

4.3 Computational details

All UEG MP2, CCD, CCD(T), and CCD(cT) calculations were conducted using a recently developed code [19]. This code fully employs the momentum conservation of the Coulomb integrals and amplitudes, resulting in a reduction of the storage requirements for CCD calculations from N^4 to N^3. Additionally, the number of operations in the CCD equations decreases from N^6 to N^4. Fully converged CCD amplitudes are obtained by solving the amplitudes equation [Eq. (4.2)] iteratively. We found an energy criteria of 10^{-8} a.u. sufficient for the analysis performed here.

We emphasize that the presented results exhibit only a weak dependence on the number of electrons in the unit cell. A larger electron number reduces the so-called finite-size error with respect to the thermodynamic limit. This error does not strongly interfere with the investigated BSIE. Importantly, the power-laws of the BSIE discussed here are fundamental and independent of the electron number. For the CCD analysis, we will work with a density of $r_{\mathrm{s}} = 5\,\mathrm{a.u.}$ with 54 electrons, while for the analysis of the

triple excitations, with 14 electrons. The influence of the electron number and density will be further analyzed in Sec. (4.4.3) and (4.5.3).

4.4 Large-momentum limit results for various CCD theories

We will now discuss the results obtained at the (approximate) CCD theory level. Before analyzing the decomposed CCD results, we will briefly revisit the cusp condition and its relevance to the current work.

The basis set incompleteness error (BSIE) originates from truncating the number of virtual states. In the Uniform Electron Gas (UEG) system, virtual states with high kinetic energy exhibit momentum values much larger than the Fermi sphere radius, which defines the set of occupied orbitals. This implies that for the two virtual indices in Eq. (4.5), $\mathbf{q} \approx \mathbf{k}_\alpha \approx -\mathbf{k}_\beta$. In this limit, the denominator of Eq. (4.5) is dominated by the kinetic energy contribution of the virtual states, and $\Delta_{ij}^{\alpha\beta} \propto q^2$, where q always represents $|\mathbf{q}|$. The Coulomb integral $v_{ij}^{\alpha\beta}$ becomes proportional to q^{-2}, leading to an asymptotic behavior of $t_{ij}^{\alpha\beta} \propto q^{-4}$. It is straightforward to assign a transfer momentum $\mathbf{q}$ to a Coulomb integral $v_{ij}^{\alpha\beta}$ [see Eq. (4.1)], and therefore, to an amplitude $t_{ij}^{\alpha\beta}$. This power-law behavior of the amplitudes is consistent across MP2, CCD$^{(1)}$, and CCD theory, carrying significant implications for the BSIE of corresponding correlation energies and related quantities.

Considering the definition of the transition structure factor in Eq. (4.14), it is directly evident that $S_{k_c}(q) \propto q^{-4}$ in the large-momentum limit. This results as a consequence of the linear cusp condition at electron-electron coalescence [99, 126]. Furthermore, utilizing Eq. (4.13), we can evaluate the basis set incompleteness error of a contribution to the correlation energy as a function of any arbitrarily large momentum k_c as:

$$\begin{aligned} \Delta E_{\mathrm{c}} &= \sum_{q} v(q) S_\infty(q) - \sum_{q<2k_c} v(q) S_{k_c}(q) \\ &\approx \int_{k_c}^{\infty} dq\, 4\pi q^2 \frac{4\pi}{\Omega q^2} S_\infty(q), \end{aligned} \tag{4.15}$$

where $S_\infty(q)$ correctly captures the asymptotic behavior of the contributions using an infinite basis set. Here, we employ isotropy and the fact that we can write the sum in Eq. (4.13) as an integral in the limit of large momentum transfer q. As indicated by Eq. (4.15), the energy contribution converges as q^{-3}, which is in accordance with the well-known N_v^{-1} convergence behavior of the correlation energy.

In order to demonstrate the physical relevance of the transition structure factor we present results for singlet $S = 0$ and triplet $S = 1$ electron pairs, which have different cusp conditions [100, 101]. Specifically, these conditions lead to distinct convergence patterns in their respective correlation energy contributions. This distinction can be identified by partitioning the correlation energy expression in Eq. (4.4), as demonstrated in the following manner [103],

$$E_\mathrm{c}^{(S=0)} = \frac{1}{2} \sum_{ijab} v_{ab}^{ij} \left(t_{ij}^{ab} + t_{ji}^{ab} \right), \tag{4.16}$$

and

$$E_\mathrm{c}^{(S=1)} = \frac{3}{2} \sum_{ijab} v_{ab}^{ij} \left(t_{ij}^{ab} - t_{ji}^{ab} \right). \tag{4.17}$$

Deducing the corresponding structure factor expressions for the aforementioned energy contributions is straightforward. The results for the finite Uniform Electron Gas (UEG) at the MP2 and CCD levels of theory are depicted in Fig. 4.1. For both methods, it is clear that the transition structure factor for singlet pairs converges as q^{-4} for large values of q. This convergence is a consequence of the singlet pair function typically being non-zero at electron-electron coalescence and complying with the cusp condition [99, 126]. On the other hand, the triplet pair function must be antisymmetric under the exchange of spatial coordinates and, therefore, must vanish at electron-electron coalescence. This accounts for the faster decay of the triplet-pair transition structure factor.

The singlet pair energies converge as q^{-3}, mirroring the convergence behavior of the total correlation energy. In contrast, the energy contribution of triplet pairs converges as q^{-5}, corresponding to $N_\mathrm{v}^{-5/3}$. It is worth noting that this behavior is well-known for molecular systems, and Klopper proposed a corresponding extrapolation scheme for singlet and triplet contributions [127].

The preceding discussion demonstrates that both the derived correlation energies and the structure factors for the Uniform Electron Gas system, represented in reciprocal space, offer a suitable approach to investigate the basis set incompleteness error and its connection to the wave function's behavior at short interelectronic distances.

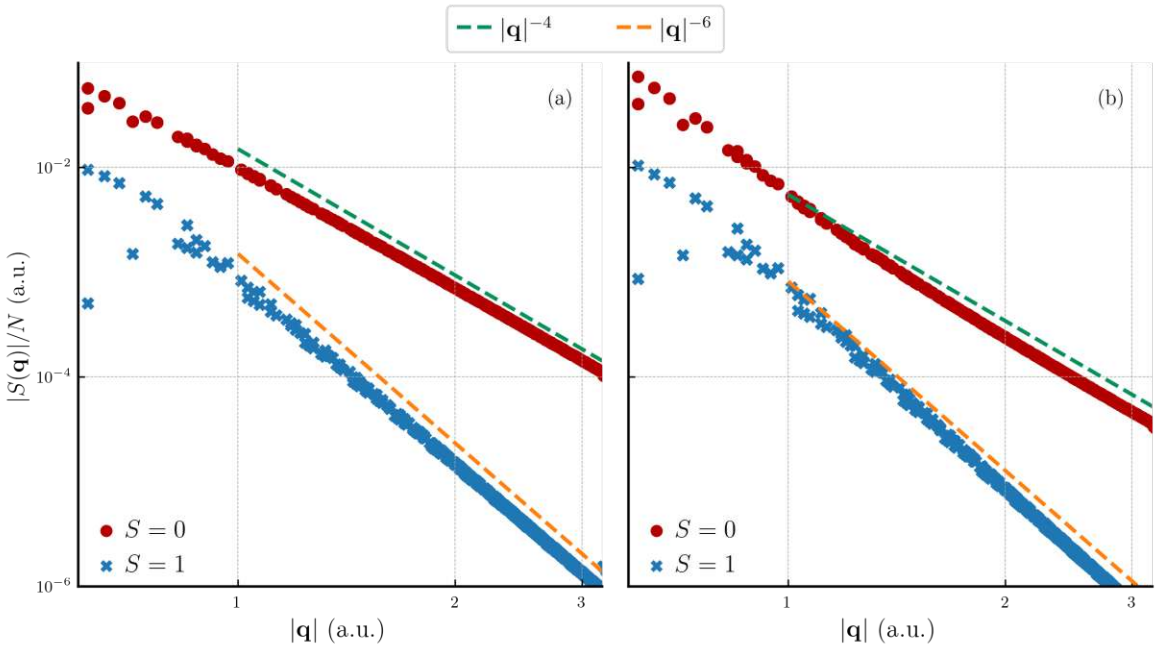

Figure 4.1: *Transition structure factors for the singlet and triplet energy contribution for (a) MP2 and (b) CCD level of theory. Results are shown for a UEG system with 54 electrons and a density of* $r_s = 5$ *a.u.*

Finally, we note that the BSIE ΔE_c is defined as the difference between the energy obtained from a calculation with a finite virtual basis set and the estimate from the complete basis set (CBS). In this work, CBS estimates are obtained by extrapolating energies from the two largest basis sets used for the given system, employing the corresponding power law.

4.4.1 Diagrammatic contributions to the CCD correlation energy

In this study, we partition the correlation energy and related quantities based on the right-hand-side contributions in Eq. (4.2). We refer to each contribution as a *channel*, aiming to identify distinct large-momentum behaviors in different channels, in order to improve or even justify correction schemes for the basis set incompleteness error. For this purpose, we introduce *channel amplitudes*, denoted as $t^{(X)}$ and defined by the expression:

$$t^{(X)}{}_{ij}^{ab}(t) = \frac{\text{Term } (X) \text{ of rhs. of Eq. (4.2) with given } t}{\Delta_{ij}^{ab}}, \tag{4.18}$$

where X represents one of the terms on the right-hand-side of Eq. (4.2). For instance, the MP2 and the particle-particle ladder channel amplitudes stem from the first and sixth terms on the right-hand-side of Eq. (4.2), denoted by MP2 and pp-ladder, respectively. They can be expressed as:

$$t^{(\mathrm{MP2})}{}_{ij}^{ab} = \frac{v_{ij}^{ab}}{\Delta_{ij}^{ab}}, \quad \text{and} \quad t^{(\mathrm{PPL})}{}_{ij}^{ab} = \frac{\sum_{cd} v_{cd}^{ab} t_{ij}^{cd}}{\Delta_{ij}^{ab}}. \tag{4.19}$$

The channel amplitudes depend on the choice of approximation for the doubles amplitudes, denoted as t on the right-hand-side of Eq. (4.2). We examine three cases: (i) $t = 0$, (ii) $t = t^{(1)}$, and (iii) the t that represents the fully self-consistent solution of Eq. (4.2). In case (i), only the MP2 channel is non-zero yielding the MP2 amplitudes $t^{(\mathrm{MP2})}(0) = t^{(1)}$. In cases (ii) and (iii), all channels $t^{(X)}(t)$ are non-zero and depend on the argument amplitudes t. The first channel always provides the MP2 amplitudes, as it is independent on t. We label the results obtained for cases (i), (ii), and (iii) as MP2, CCD$^{(1)}$, and CCD, respectively. While a similar analysis was performed in a previous work for some contributions [41], our current study extends beyond the prior work.

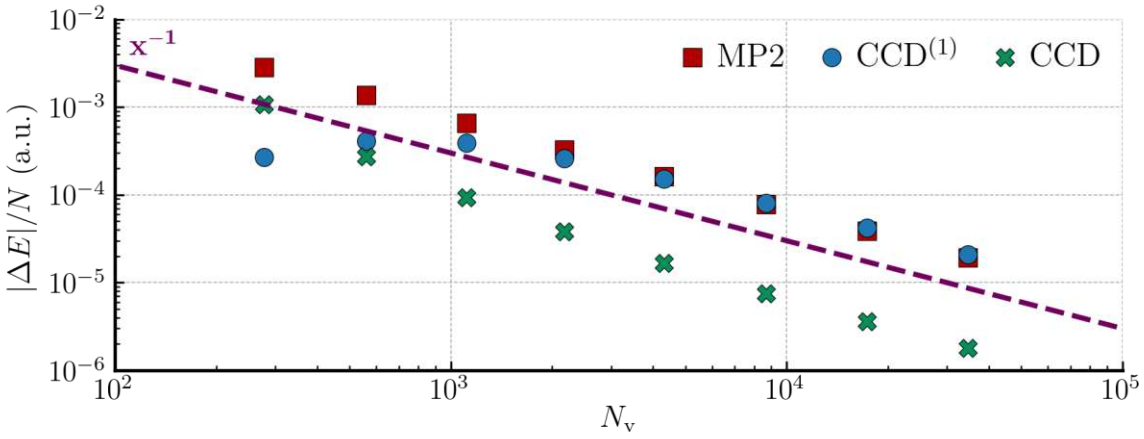

Figure 4.2: *The plot illustrates the BSIE $|\Delta E|$ per electron for MP2, CCD$^{(1)}$, and CCD. The dashed line is proportional to N_v^{-1}. Results are presented for the 54-electron system at a density of $r_s = 5$ a.u. CBS estimates are obtained by N_v^{-1} extrapolation using the two largest systems.*

Results for the density corresponding to $r_s = 5$ a.u. are presented in Fig. 4.2. In all calculations, the BSIE converges like N_v^{-1}. Notably, we observe significant differences in the magnitude of $|\Delta E|$ for a given basis set between MP2, CCD$^{(1)}$ and CCD. Additionally, it is worth noting that $|\Delta E|$ approaches zero in the CBS limit with an opposite sign in CCD$^{(1)}$ compared to MP2 and CCD. This prompts the question: *which contributions are responsible for these differences?*

We will now conduct a detailed analysis of the basis set incompleteness error and the rate of convergence for all diagrammatic channels $t^{(X)}(t)$. These channels are computed from the given amplitudes t, which are either the MP2 amplitudes $t^{(1)}$ or the solution of the amplitude equation [Eq. (4.2)], referred to as CCD$^{(1)}$ and CCD, respectively. Given the complexity of dealing with a large number of terms, this task is quite elaborate. However, employing a numerical approach one can readily obtain all BSIEs using CCD$^{(1)}$ and CCD theory. In Fig. 4.3, we illustrate all individual BSIEs through 20 plots labeled (a)–(t). The organization of these plots is as follows: Figs. 4.3(a)–(e) depict the BSIEs of all terms exhibiting a convergence of N_v^{-1} at the level of CCD$^{(1)}$ theory.

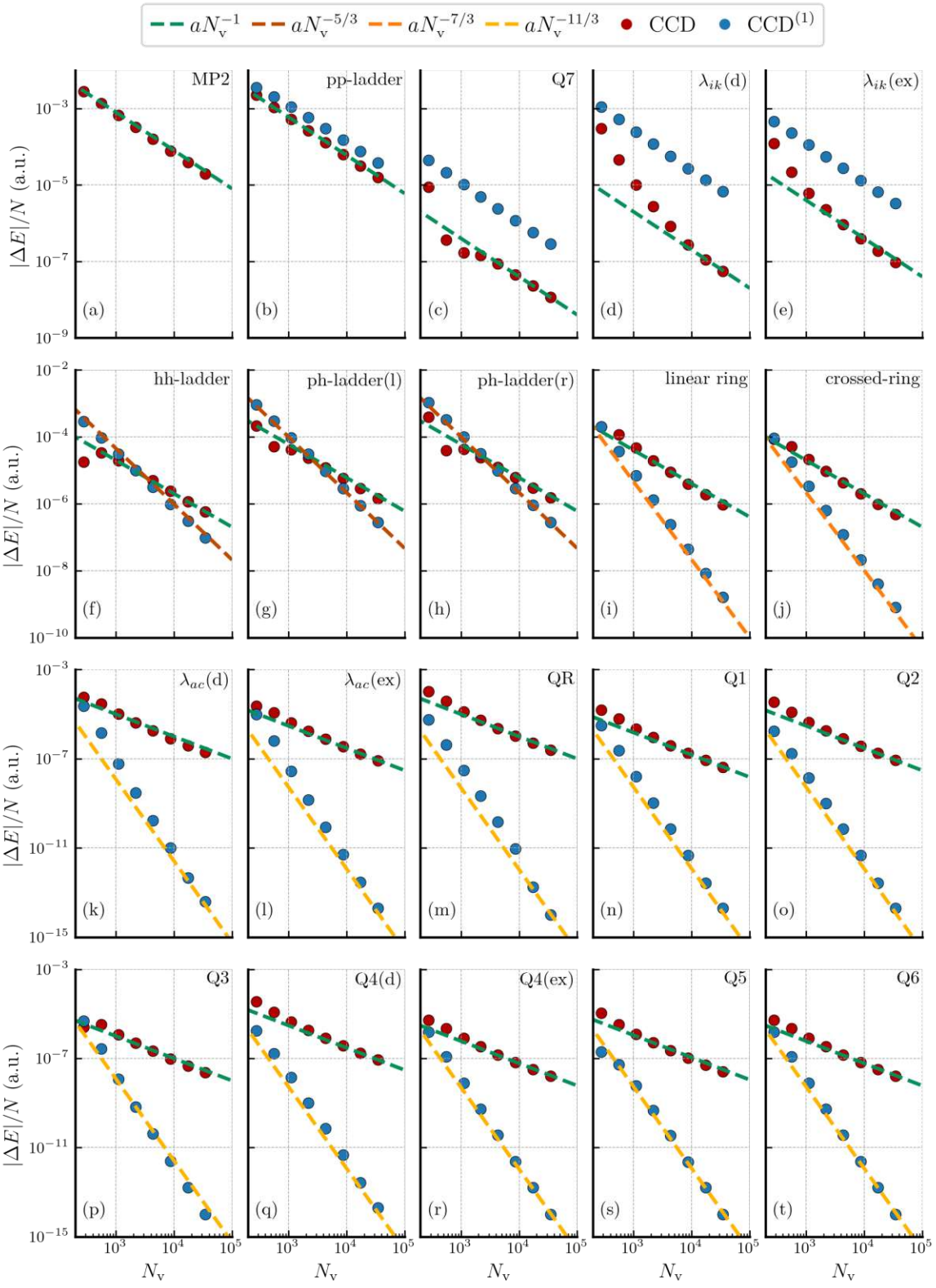

Figure 4.3: *Displayed are the absolute BSIE values per electron for all contributions to the CCD and CCD$^{(1)}$ correlation energy expressions. The individual terms are labeled with the names given in Eq. (4.2). The lines of various colors, indicating different power laws, are consistent across all plots. The results are presented for a system with 54 electrons and $r_s = 5$ a.u. CBS estimates are derived from the extrapolation of the two largest systems using the corresponding power law.*

Since MP2 is contained in both CCD$^{(1)}$ and CCD, Fig. 4.3(a) is identical to MP2 from Fig. 4.2. For Figs. 4.3(f)–(h), (i)–(j), and (k)–(t) the CCD$^{(1)}$ BSIEs exhibit convergence rates of $N_v^{-5/3}$, $N_v^{-7/3}$, and $N_v^{-11/3}$, respectively.

In contrast, all CCD BSIEs converge as N_v^{-1}. The results depicted in Fig. 4.3 highlight that the particle-particle ladder term in Fig. 4.3(b) has a notably significant contribution, alongside the MP2 term shown in Fig. 4.3(a). Therefore, our analysis begins with a focus on the PPL contribution. It's important to note that for the purpose of examining fundamental power laws, signs and prefactors will be suppressed in the following analysis.

4.4.1.1 The particle–particle ladder contribution

We will now examine the basis set convergence of the particle-particle ladder contribution to the CCD$^{(1)}$ and CCD energy. As illustrated in Fig. 4.3(b), this contribution converges in both approaches at the same rate as the MP2 term, scaling as N_v^{-1}. The magnitude of the PPL contribution is found to be comparable to that of the MP2, and especially in the case of CCD$^{(1)}$, the PPL contribution is even larger than the MP2 term. These results are consistent with the calculations performed for the same density and number of electrons as shown in Fig. 4.2.

We have previously discussed the significance of the particle-particle ladder contribution to the basis set incompleteness error in CCSD theory in Refs. [41, 128, 56]. These studies present various approaches to address the BSIE associated with the PPL con-

tribution. In Refs.[41, 128], we also offer insights into its N_{v}^{-1} convergence rate. To briefly recap, we divide the contribution to the amplitudes into the conventional and augmented virtual basis set, namely,

$$t^{(\mathrm{b})}{}_{ij}^{ab} = \frac{1}{\Delta_{ij}^{ab}} \left(\sum_{cd} v_{cd}^{ab} t_{ij}^{cd} + \sum_{\gamma\delta} v_{\gamma\delta}^{ab} t_{ij}^{\gamma\delta} \right), \tag{4.20}$$

$$t^{(\mathrm{b})}{}_{ij}^{\alpha\beta} = \frac{1}{\Delta_{ij}^{\alpha\beta}} \left(\sum_{cd} v_{cd}^{\alpha\beta} t_{ij}^{cd} + \sum_{\gamma\delta} v_{\gamma\delta}^{\alpha\beta} t_{ij}^{\gamma\delta} \right). \tag{4.21}$$

The first term in the parenthesis of Eq. (4.20) represents the PPL contribution in the conventional basis, while the second term illustrates the impact of the augmented basis on the amplitudes in the conventional basis. In the UEG, we can approximate the appearing Coulomb interaction $v_{\gamma\delta}^{ab}$ in the following way:

$$v(\mathbf{k}_\gamma - \mathbf{k}_a) \approx v(\mathbf{k}_\gamma - \mathbf{k}_i). \tag{4.22}$$

This is well justified for high lying augmented virtual states with very large momentum $|\mathbf{k}_\gamma| \gg |\mathbf{k}_a| > |\mathbf{k}_i|$. Using this approximation, the last term in Eq. (4.20) can be written as $\sum_{\gamma\delta} v_{\gamma\delta}^{ij} t_{ij}^{\gamma\delta} / \Delta_{ij}^{ab}$. As discussed earlier, this term exhibits a $1/N_{\mathrm{v}}$ convergence, indicating that the energy contribution derived from these amplitudes follows the same convergence behavior.

Moving on to the first term in Eq. (4.21), we can employ the approximation introduced in Eq. (4.22). This allows us to write the term as $\sum_{\alpha\beta} (v_{ij}^{\alpha\beta} / \Delta_{ij}^{\alpha\beta}) \sum_{cd} t_{ij}^{cd}$. The sum of the amplitudes in the aforementioned expression results in a scalar value. Notably, the first term corresponds to amplitudes at the MP2 level. This analysis stresses that for momenta $q \gg k_{\mathrm{cut}}$, the amplitudes arising from Eq. (4.21) become proportional to those from the MP2 level, albeit with an opposite sign. A straightforward observation indicates that the second term in Eq. (4.21) converges much more rapidly, specifically as q^{-6}, making it negligible in the limit of large momenta. We note that due to the symmetry of the particle-particle term, the energy contribution from the second term in Eq. (4.20) is identical to the first term in Eq. (4.21) at MP3 level of theory. In CCD, however, this is not necessarily the case.

4.4.1.2 Slowly converging quadratic contributions

We now aim to analyze the three contributions, quadratic in amplitude t, shown in Fig. 4.3(c)–(e). Notably, these are the only contributions, beyond MP2 and PPL, exhibiting a N_v^{-1} convergence of the BSIE at the CCD$^{(1)}$ level of theory.

To clarify this observation, we consider a two-electron singlet system and separate the contribution to the amplitudes into the conventional and augmented virtual basis sets. The three terms we are examining are the $\lambda_{ik}(d)$, $\lambda_{ik}(ex)$, and $Q7$ terms on the right side of Eq. (4.2). For the two-electron system, these terms become identical, except for different prefactors specific to that system. Their contributions are given by:

$$t^{(\mathrm{c\text{–}e})\,ab}_{\;\;ii}(t) = \frac{1}{\Delta^{ab}_{ii}}\, t^{ab}_{ii} \left(\sum_{cd} v^{ii}_{cd} t^{cd}_{ii} + \sum_{\gamma\delta} v^{ii}_{\gamma\delta} t^{\gamma\delta}_{ii} \right), \tag{4.23}$$

$$t^{(\mathrm{c\text{–}e})\,\alpha\beta}_{\;\;ii}(t) = \frac{1}{\Delta^{\alpha\beta}_{ii}}\, t^{\alpha\beta}_{ii} \left(\sum_{cd} v^{ii}_{cd} t^{cd}_{ii} + \sum_{\gamma\delta} v^{ii}_{\gamma\delta} t^{\gamma\delta}_{ii} \right). \tag{4.24}$$

In Eq. (4.23), the right term in the parenthesis illustrates how the presence of the augmented basis alters the amplitudes belonging to the conventional basis set. The respective amplitudes are scaled by the terms in parentheses. For the two-electron singlet, this sum corresponds to the BSIE of the correlation energy of the electron pair, which converges slowly as N_v^{-1}. Consequently, the (c–e) quadratic contributions exhibit the same power-law behavior in both CCD$^{(1)}$ and CCD calculations. The amplitudes from the augmented basis set of Eq. (4.24) show a faster convergence. As both orbitals ϕ_α and ϕ_β are virtual states with large momenta, it follows that $\Delta^{\alpha\beta}_{ii} \propto q^2$ and consequently, $t^{\alpha\beta}_{ii} \propto q^{-4}$. This results in an overall q^{-6} convergence of the corresponding amplitudes. Applying these amplitudes with augmented virtual states in the energy expression Eq. (4.4) leads to the observed $N_\mathrm{v}^{-5/3}$ behavior of the BSIE. Now, we are in the position to explain the significant difference in the magnitude of the BSIE for these contributions in CCD$^{(1)}$ and CCD [see Fig. 4.3(c)-(e)]. In the previous section, we have seen that the amplitude elements of the augmented virtual manifold are altered by the PPL contribution [see Eq. (4.21)]. For the studied system with 54 electrons at a density of $r_\mathrm{s} = 5.0$ a.u., the amplitude elements from the augmented virtual states are significantly smaller in CCD, than they are in CCD$^{(1)}$. The predominant BSIE

contribution stems from Eq. (4.23) which contains a contraction of such amplitude elemts from augmented virtual states. This explains why the BSIE of the above terms is larger in CCD$^{(1)}$ compared to CCD.

We emphasize that this analysis, limited to a two-electron singlet, has evident constraints. The results for the 54-electron system in Fig. 4.3(c)–(e) reveal differences of more than one order of magnitude between the various terms. However, for the two-electron singlet, all terms are identical, apart from a factor of two.

4.4.1.3 Hole-hole and particle-hole ladder diagrams

This section addresses the three other ladder terms, linear in the amplitude t, shown in Fig. 4.3(f)–(h). For all three terms, the BSIE converges as $N_{\mathrm{v}}^{-5/3}$ in the CCD$^{(1)}$ calculations. We focus on a specific term, namely a particle–hole term ${t^{(\mathrm{g})}}_{ij}^{ab}(t)$ depicted in Fig. 4.3(g), to study the origin of this convergence behavior. The remaining two terms can be treated similarly. We list all contributions after partitioning the virtual states A and B explicitly into conventional and augmented virtual basis sets as:

$$ {t^{(\mathrm{g})}}_{ij}^{ab} = \frac{1}{\Delta_{ij}^{ab}} \sum_{ck} v_{ci}^{ak} t_{kj}^{cb} + \frac{1}{\Delta_{ij}^{ab}} \sum_{\gamma k} v_{\gamma i}^{ak} t_{kj}^{\gamma b}, \tag{4.25} $$

$$ {t^{(\mathrm{g})}}_{ij}^{\alpha b} = \frac{1}{\Delta_{ij}^{\alpha b}} \sum_{ck} v_{ci}^{\alpha k} t_{kj}^{cb} + \frac{1}{\Delta_{ij}^{\alpha b}} \sum_{\gamma k} v_{\gamma i}^{\alpha k} t_{kj}^{\gamma b}, \tag{4.26} $$

$$ {t^{(\mathrm{g})}}_{ij}^{a\beta} = \frac{1}{\Delta_{ij}^{a\beta}} \sum_{ck} v_{ci}^{ak} t_{kj}^{c\beta} + \frac{1}{\Delta_{ij}^{a\beta}} \sum_{\gamma k} v_{\gamma i}^{ak} t_{kj}^{\gamma\beta}, \tag{4.27} $$

$$ {t^{(\mathrm{g})}}_{ij}^{\alpha\beta} = \frac{1}{\Delta_{ij}^{\alpha\beta}} \sum_{ck} v_{ci}^{\alpha k} t_{kj}^{c\beta} + \frac{1}{\Delta_{ij}^{\alpha\beta}} \sum_{\gamma k} v_{\gamma i}^{\alpha k} t_{kj}^{\gamma\beta}. \tag{4.28} $$

The first term on the right hand side of Eq. (4.25) is the conventional expression in the finite basis set. The second term in Eq. (4.25), as well as the terms in Eqs. (4.26) and (4.27) contain amplitudes or Coulomb integrals with one virtual orbital in the finite basis and the other in the augmented basis set. The vast majority of these terms are zero due to momentum conservation. Non-zero contributions can only be found in a volume corresponding to the Fermi sphere. Consequently, these contributions are expected to be negligible compared to the terms in Eq. (4.28). In this context, the

first term also involves one virtual state from the finite basis and the other from the augmented virtual states, making this contribution negligible as well. The second term in Eq. (4.28) converges as q^{-6}, originating from the energy denominator $1/\Delta_{ij}^{\alpha\beta}$ and the amplitudes $t_{kj}^{\gamma\beta}$ scaling as q^{-2} and q^{-4}, respectively. The maximum momentum transfer in the appearing Coulomb interaction cannot exceed $2k_\mathrm{F}$, ensuring that the Coulomb interaction of this form does not alter the convergence behavior for large momenta q. Additionally, the sum over the states k and γ does not affect the asymptotic behavior, as the number of states fulfilling momentum conservation in the Coulomb integral is proportional to k_F. In conclusion, the three ladder terms discussed here converge as q^{-6}, corresponding to $N_\mathrm{v}^{-5/3}$.

Interestingly, the BSIE behavior of ladder terms (f)–(h) undergoes a fundamental change from $N_\mathrm{v}^{-5/3}$ in CCD$^{(1)}$, to N_v^{-1} in CCD calculations. The primary cause of this effect lies primarily in the PPL contribution, and to a lesser extent, in the other three quadratic contributions discussed in the previous section. Expressions such as Eq. (4.23) couple the amplitudes of the augmented virtual states to the amplitudes of conventional virtual states. Consequently, the argument amplitudes in Eq. (4.18) are altered, leading to a change in the energy contribution of the given channel.

4.4.1.4 Linear ring type diagrams

The terms depicted in Fig. 4.3(i)–(j) are commonly referred to as ring and crossed-ring diagrams. Similar to the previously discussed ladder diagrams, the ring and crossed-ring diagrams also exhibit a N_v^{-1} behavior in CCD, stemming from the same underlying mechanism. In CCD$^{(1)}$, however, the BSIE converges as $N_\mathrm{v}^{-7/3}$. We illustrate the ring contribution as an example in Fig.4.3(i). The corresponding amplitudes are given by:

$$t^{(i)}{}_{ij}^{\alpha\beta} = \frac{1}{\Delta_{ij}^{\alpha\beta}} \sum_{k\gamma} v_{i\gamma}^{ak} t^{(1)}{}_{kj}^{\gamma b}. \tag{4.29}$$

In the limit of high-lying virtual states, the ring contribution exhibits q^{-2}, q^{-2}, and q^{-4} contributions from $1/\Delta_{ij}^{\alpha\beta}$, $v_{i\gamma}^{ak}$, and $t^{(1)}{}_{kj}^{\gamma b}$, respectively. This results in an overall q^{-8} convergence of the amplitudes. It's worth noting that both diagrams in Fig. 4.3(i)

and 4.3(j) become identical in the large q regime, except for a different prefactor, while it is well-known that they behave very differently in the small q limit [21].

4.4.1.5 Other quadratic contributions

The remaining ten contributions in Fig. 4.3(k)–(t) are all quadratic in the amplitudes t. In CCD$^{(1)}$, the BSIE of these contributions exhibits rapid decay, scaling as $N_\mathrm{v}^{-11/3}$. Similar to the previously discussed cases, this behavior can be explained by the aggregation of factors: q^{-4} for each amplitude, q^{-2} for the Coulomb interaction mediating momentum q, and another q^{-2} for the energy denominator $1/\Delta_{ij}^{\alpha\beta}$. Additionally, in CCD calculations, the convergence behavior of the BSIE changes and becomes inversely proportional to the number of employed states, N_v.

4.4.2 Structure Factor analysis

As discussed in previous sections, in CCD, the elements of the amplitudes depend on the employed basis set. This dependence also extends to the transition structure factor, as indicated by Eq. (4.14). Consequently, we analyze the transition structure factor using a large basis set with over 2500 virtual states per occupied orbital. Our analysis focuses solely on results from fully converged CCD amplitudes, excluding those from CCD$^{(1)}$ calculations. The channel-resolved transition structure factor $S^{(X)}$ is defined by employing the respective channel amplitudes $t^{(X)}$ in Eq. (4.14). Fig. 4.4 illustrates the transition structure factors in the limit of large transfer momenta q, providing insights into features at very short interelectronic distances. Notably, we identify only two channels that are of leading order for large q, a central finding in this study. These contributions correspond to the MP2 and the PPL contributions, both exhibiting a q^{-4} decay for large values of q. It follows from Eq. (4.13) that this q^{-4} behavior of the transition structure factor corresponds to an N_v^{-1} convergence of the BSIE. This implies that all other channels do not significantly influence the transition structure factor at large momentum transfers q. Consequently, they cannot alter the linear slope of the singlet transition pair correlation function at the coalescence point. It's important to note that the transition pair correlation function is not an observable. However, these results support the idea that, for all channels besides MP2 and PPL, the slow

N_v^{-1} convergence of the BSIE arises from long-range modulations of the corresponding channel-decomposed transition structure factor.

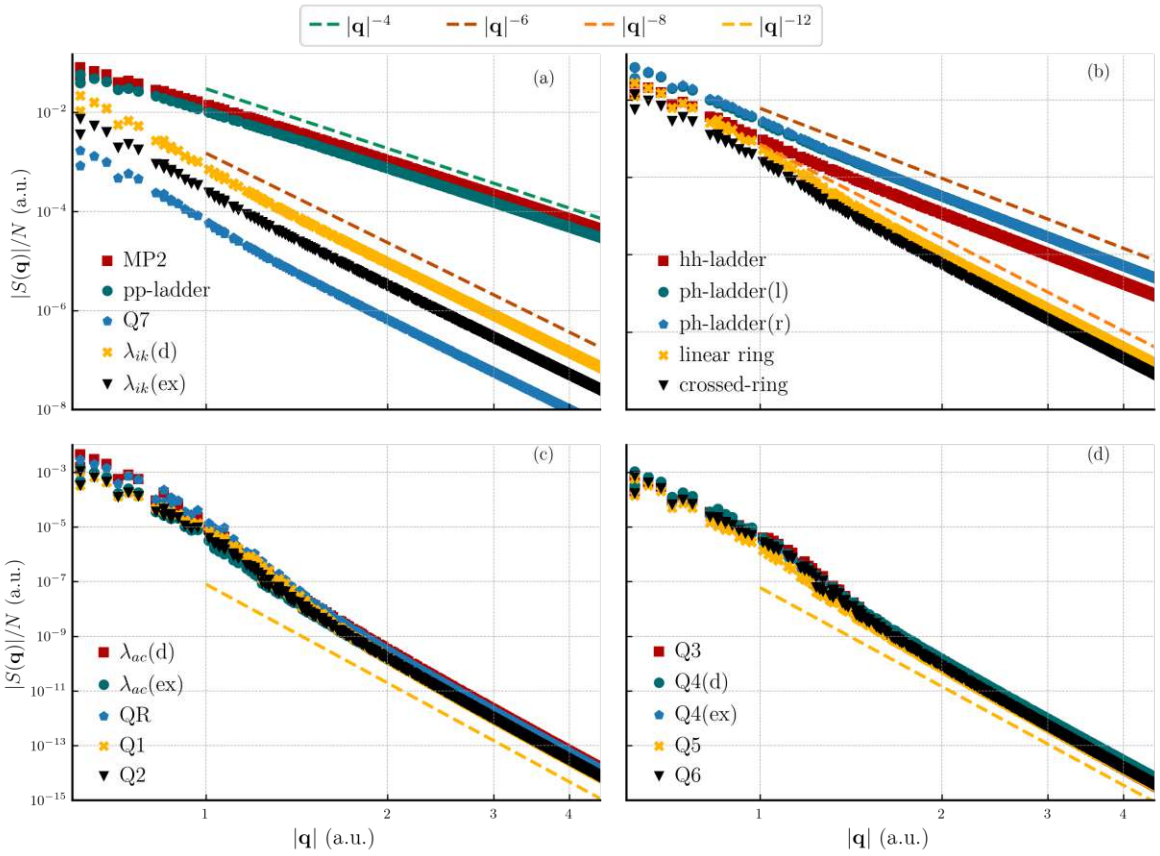

Figure 4.4: *Transition structure factor results for the individual diagrammatic channels. Results are obtained from a converged CCD calculation with 54 electrons at $r_\mathrm{s} = 5$ a.u. and 67664 virtual orbitals. All figures show various diagrammatic contributions, labeled as in Fig. 4.3. In addition, four lines with different powers of q^{-n} are shown.*

4.4.3 Dependence on electron number and density

In the preceding sections, we conducted a detailed examination of the BSIE for various contributions to the CCD energy in a single system comprising of 54 electrons at a

density of $r_s = 5$ a.u. Our findings revealed that, unlike the MP2 term, the PPL contribution exhibits the most substantial BSIE. Given that the BSIE of the PPL and MP2 terms have opposite signs, this discrepancy can result in a significant reduction of the overall BSIE in CCD.

In this section, we demonstrate the general applicability of our main findings across various electron numbers and densities. It is important to note that we focus exclusively on the CCD level of theory, as it is the primary focus of this work, omitting analysis at the CCD$^{(1)}$ level. We examine the BSIE of different diagrammatic channels, by taking advantage of the identical N_v decay exhibited by all channels in CCD. Results for three distinct electron numbers and two electron densities are presented in Table 4.1.

Table 4.1: *Shown is the ratio of BSIEs between different channels and the MP2 term. These ratios are obtained from calculations with sufficiently large basis sets ($N_v/N_o \approx 150 - 200$). We have grouped the slowly quadratic contributions, i.e. (c)–(e), the linear ladder terms except PPL, (f)–(j), and finally all other quadratic terms (k)–(t). All values are scaled by* 10^{-3}.

	$r_s = 1$			$r_s = 5$		
$\Delta E^{(X)}/\Delta E^{(a)}$	14	54	162	14	54	162
(b)	−410	−400	−404	−798	−795	−797
(c)–(e)	−11	−12	−8.3	0.9	−1.6	−3.7
(f)–(j)	−24	−15	−24	−97	−87	−80
(k)–(t)	−0.5	−2.5	−1.5	−1.2	−0.3	−0.9

In the high-density system with $r_s = 1$ a.u., all terms, except the PPL, exhibit minimal contributions to the total BSIE. Notably, the PPL term stands out with a significant BSIE, approximately 40% compared to MP2. Remarkably, the BSIE of the PPL term remains virtually independent of the system size for both densities under consideration.

In the lower density system with $r_s = 5$ a.u., the quadratic contributions (c)–(e) and (k)–(t) exhibit a small BSIE. In contrast, the BSIE of all linear terms (f)–(j) is notably larger compared to the system of higher density. Specifically, the BSIE of the PPL

contribution is around 80% of the MP2 value. Additionally, the other linear terms in (f)–(j) are much more pronounced at low densities, with a BSIE approximately 10% of the BSIE from MP2. Importantly, these results demonstrate no strong dependence on the employed electron number.

It is noteworthy that in the low-density limit, the PPL contribution becomes more significant compared to MP2 theory. This observation aligns with expectations, as higher-order perturbation theory terms become more prominent as r_s increases. Consequently, truncated finite-order perturbation theory approaches, such as $CCD^{(1)}$, become unreliable. Indeed, we find that $CCD^{(1)}$ overestimates the PPL contribution compared to CCD significantly. However, similar to the resummation over ring diagrams, CCD performs a resummation over ladder diagrams, which proves crucial for a well-balanced estimate of the PPL contribution in the low-density limit.

4.5 Perturbative triple excitations

This section focuses on the BSIE of the perturbative triples contributions discussed in Sec. (4.2.3). We initiate the analysis with the (T) method and subsequently explore the differences for the (cT) method.

4.5.1 The BSIE of the (T) method

The energy expression for the (T) contribution in Eq. (4.6) involves two distinct contractions: a particle contraction and a hole contraction [Eq. (4.7)]. Consequently, the total energy expression can be decomposed into three terms. The first term contains only hole contractions, denoted as (T)-hh hereafter. The second term contains both one hole and one particle contractions, denoted as (T)-ph. Finally, the third term comprises only terms with particle contractions, referred to as (T)-pp. The diagrammatic representations of these three terms are illustrated in Fig. 4.6(a)–(c) for non-permuted terms. It is important to note that the sum of these three terms, including the permutations between particles and between holes, equals the full (T) correlation energy.

We now analyze these three terms individually. In the following, we write the algebraic contributions without the intermediates defined in Section 4.2.3. We commence the analysis with the (T)-hh contribution, illustrated in Fig. 4.6(a), which can be expressed, without applying permutations, as:

$$E = 8 \sum_{ijk} \sum_{abc} \sum_{mn} t_{in}^{ab} t_{im}^{ab} v_{jk}^{nc} v_{mc}^{jk} \frac{1}{\Delta_{ijk}^{abc}}. \tag{4.30}$$

Initially, we investigate the BSIE of this contribution using MP2 amplitudes. As depicted in Fig. 4.5(a), the BSIE exhibits rapid convergence, scaling as $N_\mathrm{v}^{-7/3}$.

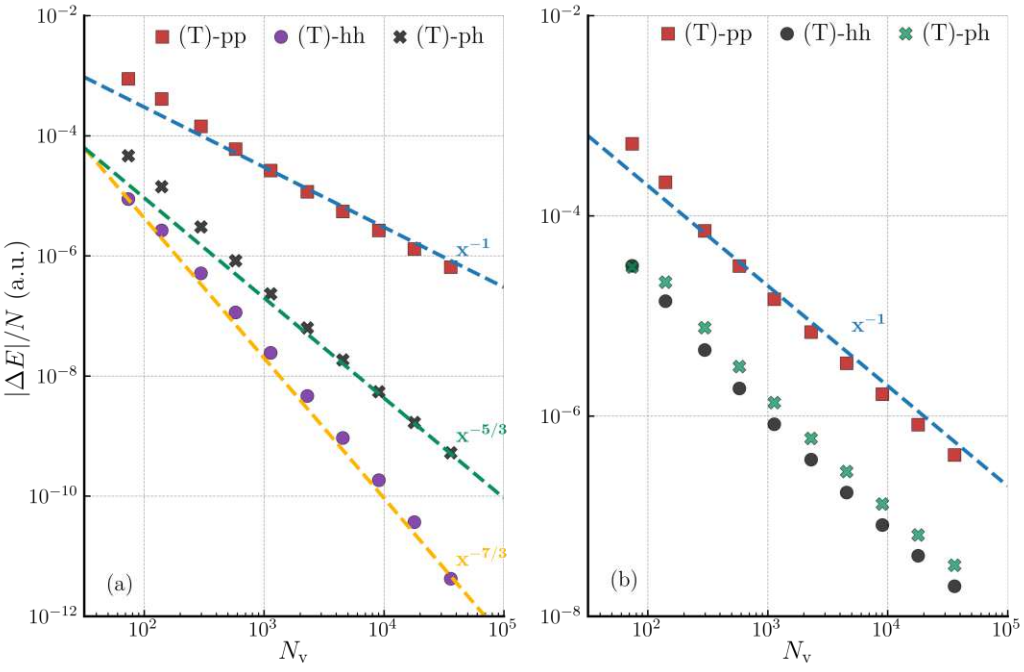

Figure 4.5: *Figures (a) and (b) present the BSIE of the three mentioned contributions for a system with 14 electrons and $r_\mathrm{s} = 5$ a.u. In (a), MP2 amplitudes are utilized, while (b) displays results with CCD amplitudes. CBS estimates are derived from extrapolation of the two largest systems using the respective power law.*

The expression involves a sum over three virtual states. Notably, the sum over the state c does not contribute to the correlation energy for sufficiently high-lying virtual

states. This is because the Coulomb integrals involved include three states from the set of occupied orbitals. As a result, all Coulomb integrals where the wave vector of the virtual state exceeds $3k_\mathrm{F}$ are zero due to momentum conservation. Therefore, an energy contribution from such high-lying virtual states can only arise from the sums over the states a and b. As mentioned earlier, contributions of type t_{ij}^{ab} have a negligibly small contribution. Using the notation of augmented virtual states, these contributions can be expressed as:

$$E = 8 \sum_{ijk} \sum_{\alpha\beta c} \sum_{mn} t_{in}^{\alpha\beta} t_{im}^{\alpha\beta} v_{jk}^{nc} v_{mc}^{jk} \frac{1}{\Delta_{ijk}^{\alpha\beta c}}. \tag{4.31}$$

As discussed earlier, contributions of the type $t_{in}^{a\beta}$ have negligible impact in the limit of large values of q. The fundamental convergence behavior of Eq. (4.31) is straightforward to derive. In the limit of high-energy virtual states, the wave vectors of states inside the Fermi sphere become negligible, leading to amplitudes converging as q^{-4}. Simultaneously, the energy denominator $\Delta_{ijk}^{\alpha\beta c}$ converges as q^{-2}. In this fundamental limit, the energy expression can be written as:

$$\lim_{q\to\infty} \int_q^\infty dq' q'^2 \frac{1}{q'^4} \frac{1}{q'^4} \frac{1}{q'^2}, \tag{4.32}$$

aligning with the observed $N_\mathrm{v}^{-7/3}$ behavior of the BSIE. When applying the permutations in Eqs. (4.6) and (4.8), the BSIE of some contributions is zero for sufficiently large transfer momenta q, as none of the additional contributions fulfill the corresponding momentum conservation. Next, we examine the scenario where the CCD amplitudes are utilized in the energy expression for $E^{(\mathrm{T})-\mathrm{hh}}$. The corresponding BSIE is illustrated in Fig. 4.5(b), displaying an explicit N_v^{-1} behavior. A similar observation was made in Secs. (4.4.1.3), (4.4.1.4), and (4.4.1.5), which can be attributed to the basis set incompleteness of the employed amplitudes t_{ij}^{ab} within the finite basis set.

The (T)-ph contribution, depicted in Fig. 4.6(b), exhibits the same fundamental convergence behavior as (T)-hh, but only when CCD amplitudes are utilized. However, when employing MP2 amplitudes the BSIE converges with $N^{-5/3}$. The corresponding BSIEs are shown in Fig. 4.5(a) and Fig. 4.5(b). Interestingly, the term without permutations, as illustrated in Fig. 4.6(b), converges faster, namely as $N^{-7/3}$. This behavior can be attributed to the presence of three occupied states in one of the Coulomb inte-

grals, preventing contributions from the sufficiently high-lying states c. Consequently, the momentum transfer of the other appearing Coulomb integral v_{bc}^{kf} is also restricted to a multiple of k_F. However, when employing the permutations in Eqs. (4.6) and (4.8), some of the contributions show a slower convergence rate, namely $N^{-5/3}$. For instance, this can be seen for the following contribution

$$E = -4 \sum_{ijk} \sum_{\alpha\beta c} \sum_{me} t_{im}^{\alpha\beta} t_{ij}^{ce} v_{\beta\alpha}^{ek} v_{jk}^{mc} \frac{1}{\Delta_{ijk}^{\alpha\beta c}}. \tag{4.33}$$

This energy expression represents a particular contribution of the full (T) energy, as given in Eq. (4.6). It is derived by considering only the contraction of the first element ($\overline{W}_{ijk}^{abc}$) in the parentheses of Eq. (4.6), where $\overline{W}_{ijk}^{abc}$ includes only the permutation from Eq. (4.8) where a and c are swapped. In Eq. (4.33) the finite and augmented virtual states are chosen to yield the dominant contribution for this term. In this expression, one set of amplitudes includes states from the augmented virtual states, while the other can incorporate states from the finite virtual basis set. Consequently, the expression accumulates the factors q^{-4}, q^{-2}, and q^{-2} from the amplitudes, Coulomb integral and energy denominator, respectively. The final BSIE is found by the corresponding limit

$$\lim_{q\to\infty} \int_q^\infty dq' q'^2 \frac{1}{q'^4} \frac{1}{q'^2} \frac{1}{q'^2}. \tag{4.34}$$

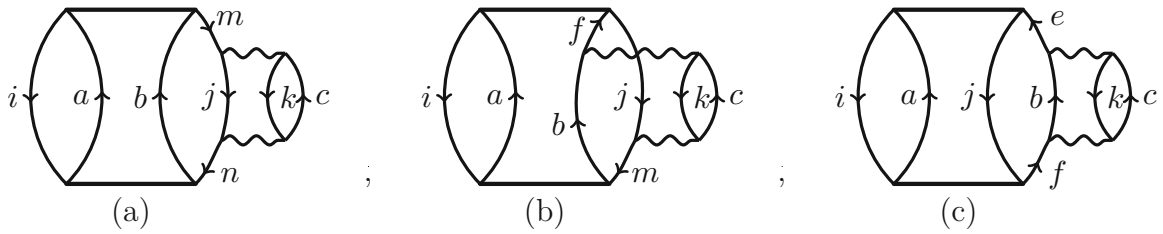

Figure 4.6: *(a), (b), and (c) illustrate diagrammatically the three different contributions to (T) approximation: hh, ph, and pp, respectively.*

Lastly, we address the contribution (T)-pp, depicted in Fig. 4.6(c), which exhibits a significantly larger BSIE compared to the two other discussed contributions, as evident

in Fig. 4.5(a) and Fig. 4.5(b). The BSIE for this contribution follows a N_{v}^{-1} behavior for both MP2 and CCD amplitudes. In this case, both of the appearing Coulomb interactions involve three particle and one hole state. Consequently, amplitudes containing states from the finite virtual basis set can couple with augmented virtual states at the Coulomb interactions. The corresponding expression, represented in the notation of finite and augmented virtual states, is as follows:

$$E = 8 \sum_{ijk} \sum_{a\beta\gamma} \sum_{ef} t_{ij}^{af} t_{ij}^{ae} v_{\beta k}^{f\gamma} v_{e\gamma}^{\beta k} \frac{1}{\Delta_{ijk}^{a\beta\gamma}}. \tag{4.35}$$

The two occurring amplitudes belong to the finite virtual basis set and do not introduce a further power of q^{-4} , however the Coulomb interactions now scale as q^{-2} resulting in a fundamentally different limit, namely,

$$\lim_{q\to\infty} \int_q^\infty dq' q'^2 \frac{1}{q'^2} \frac{1}{q'^2} \frac{1}{q'^2}. \tag{4.36}$$

These terms, as expressed in Eq. (4.35), dominate the BSIE of the (T)-pp contribution, thereby influencing the overall BSIE of the entire (T) contribution. Contributions where the amplitudes contain states from the augmented virtual basis set show a convergence of $N^{-5/3}$ or faster. We note that certain permutations in Eqs. (4.6) and (4.8) exhibit faster converging contributions.

It is important to note that these findings are not entirely new. It has been empirically well-known that the leading rate of convergence of (T) is similar to MP2 [129]. This observation has prompted the development of *ad hoc* correction schemes that rescale the (T) contributions with MP2 terms to address the BSIE of (T) [77, 130]. Additionally, Köhn incorporated an explicit correlated framework for the (T) contribution [131]. He successfully identified, through numerical analysis, that the terms provided in Eq. (4.35) contain crucial contributions to the BSIE [132].

4.5.2 (T) vs. (cT) methods

In this concluding section, we investigate the BSIE of the recently proposed complete perturbative triples correction (cT). The motivation behind this work was to incorporate additional contributions to prevent the perturbative correction from diverging

for metallic systems [125]. These additional contributions are provided in Eqs. (4.11) and (4.12), totaling ten terms beyond the bare Coulomb interactions in Eqs. (4.11) and (4.12). It is noteworthy that only two of these additional terms, namely $v_{ef}^{bm} t_{km}^{cf}$ and $v_{jf}^{mn} t_{kn}^{cf}$, are responsible for resolving the divergence for metallic systems in the (T) approximation. The previous analysis in the literature focused on the small-q regime where the divergence occurs. However, in this work, we analyze the behavior for large q, specifically studying the BSIE of the (cT) method.

For these reasons, we examine the convergence of the energy expressions (T) and (cT) for the same system. Similar to the CCD analysis, the BSIE is depicted for MP2 amplitudes and converged CCD amplitudes in Fig. 4.7(a) and (b), respectively. It is evident that the BSIE of the additional terms in (cT) is at least one order of magnitude smaller than the BSIE of the (T) expression. Although the difference between (T) and (cT) is more pronounced when using CCD amplitudes, this difference also exhibits a slow N_{v}^{-1} convergence with MP2 amplitudes. This analysis indicates that at least one of the additional terms is expected to lead to a slow N_{v}^{-1} convergence. Consequently, we perform an individual analysis of the ten additional contributions. The diagrammatic contributions are illustrated in Fig. 4.8. It is worth noting that the first diagram on the right-hand-side corresponds to (T), whereas all others are included in (cT) and are denoted as p/h1–p/h5. Once again, we use amplitudes from the MP2 level of theory for the subsequent analysis, as all terms exhibit a N_{v}^{-1} convergence with CCD amplitudes. This phenomenon was already observed for the CCD terms, as discussed in Section (4.4.1.3). The BSIEs of the individual terms are presented in Fig. 4.7(c) and (d). Evidently, only one of these terms demonstrates slow convergence, while all other contributions converge as $N_{\mathrm{v}}^{-5/3}$.

Notably, the slowly converging h1 contribution exhibits striking similarities to one of the terms showing slow convergence in the CCD expression [see Fig. 4.3(d)].

4.5.3 Dependence on electron number and density

Up to this point, the analysis of the BSIE of the triples contributions was conducted for a system with 14 electrons and a density of $r_{\mathrm{s}} = 5\,\mathrm{a.u.}$ In this section, we extend

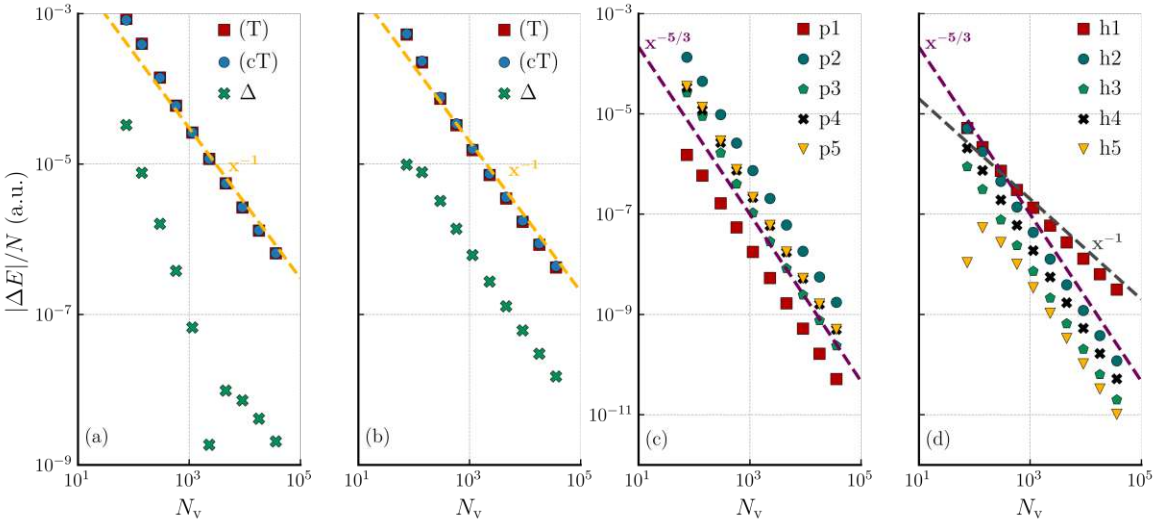

Figure 4.7: *(a-b) The BSIEs per electron of the (T) and (cT) contributions for a system with 14 electrons at a density $r_s = 5$ a.u. are shown. Additionally, the convergence of the energy difference between (T) and (cT), denoted as Δ, is presented. (a),(b) display results for MP2 and CCD amplitudes, respectively. (c-d): p1-5 are the five additional diagrams emerging from Eq. (4.11), whereas h1-5 are the corresponding terms connected from Eq. (4.12). CBS estimates are obtained from extrapolation of the two largest systems using the corresponding power law.*

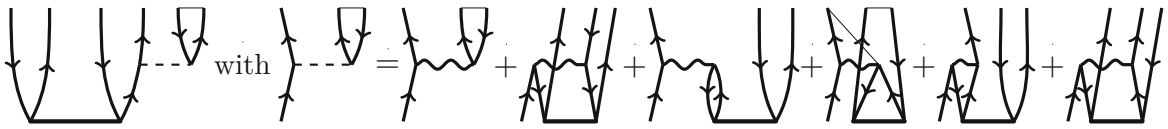

Figure 4.8: *Diagrammatic illustration of the terms in (cT) as given in Eq. (4.11). The additional terms connected to a doubles amplitude on the right are introduced in the (cT) method, labeled 1 to 5 based on their order of appearance.*

our study to two different densities, $r_s = 1$ a.u. and $r_s = 5$ a.u., as well as three different system sizes: 14, 54, and 114 electrons. All results are obtained with fully converged

CCD amplitudes. Fig. 4.9 provides an overview of the BSIE for the quantities discussed in the previous sections, including the contributions of the previously defined channels T-pp, T-ph, and T-hh, as well as the difference between the (T) and the (cT) methods.

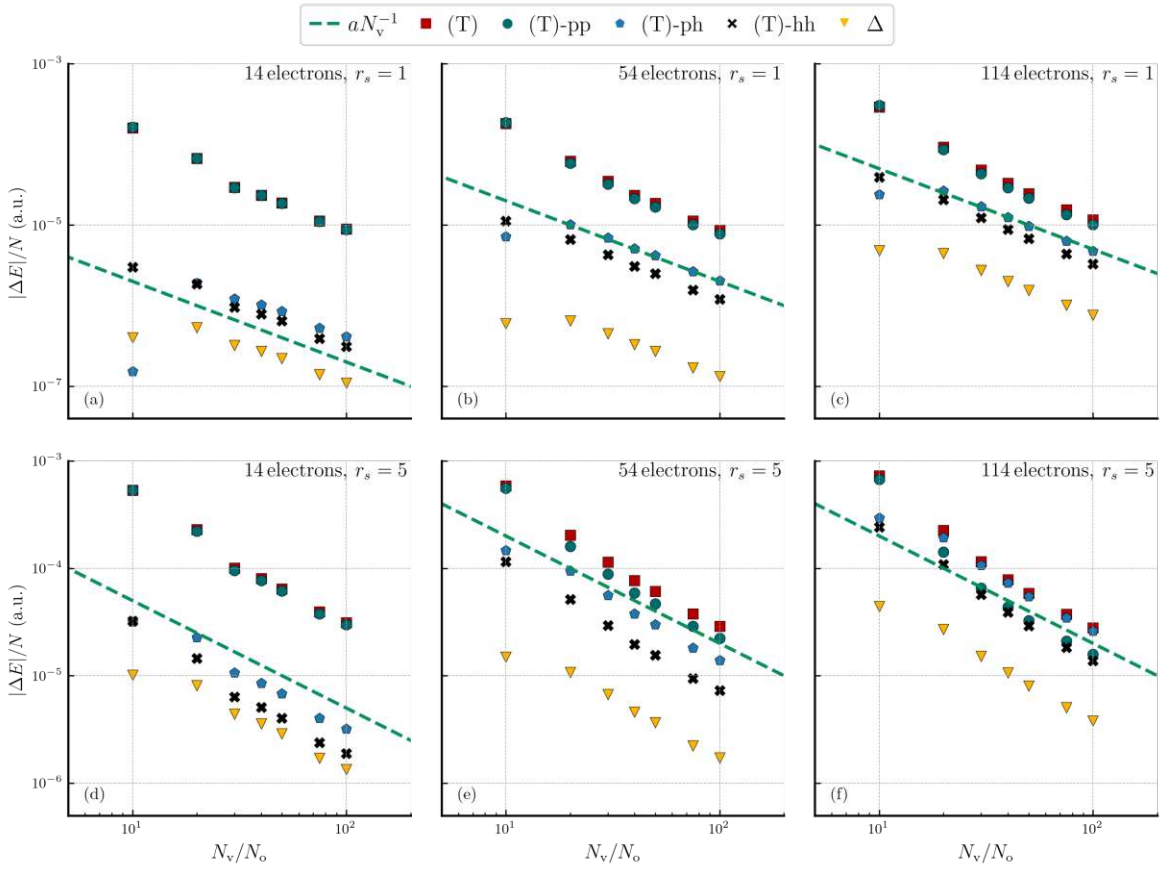

Figure 4.9: *BSIEs per electron for different contributions are presented. (a)–(c) show results for $r_s = 1$ a.u., whereas (d)–(f) use a density of $r_s = 5$ a.u. Panels in the left, middle, and right columns show different system sizes with 14, 54, and 114 electrons, respectively. To allow comparison between systems with different electron numbers, we present the results in BSIE per electron, with respect to the number of virtual states per occupied orbitals. Moreover, the energy difference between (T) and (cT) is denoted as Δ.*

For all analyzed systems, the difference between (T) and (cT) is consistently at least one order of magnitude smaller than the BSIE of (T). Notably, the terms beyond (T) in (cT) become more significant for larger electron numbers and r_s values.

Moving on to the discussion of the three different channels of the (T) contribution, we observe that for small values of r_s, as well as for a small number of electrons, the (T)-pp channel dominates the BSIE of the overall (T). However, the BSIE of the other two channels, namely (T)-ph and (T)-hh, increases on a relative scale when the number of electrons or the value of r_s is increased, respectively. For the system with 114 electrons and a density of $r_s = 5\,\text{a.u.}$, the (T)-ph term becomes the channel with the largest BSIE. It is crucial to note, as discussed in the previous section, that the N_v^{-1} decay of (T)-ph and (T)-hh does not originate from contributions with large momenta q. Instead, the BSIE arises from changes in the CCD amplitude elements corresponding to the finite virtual basis set. These two leading order contributions, namely the basis set incompleteness in the CCD amplitudes and the additional contributions from $W_{ijk}^{a\beta\gamma}$ as given in Eq. (4.35) have already been identified by Köhn [131, 132] in the context of an F12 correction for the (T) contribution. The analysis conducted here demonstrates that the relative importance of one or the other contribution depends on the studied system.

4.6 Summary and conclusions

This work provides a comprehensive analysis of various coupled-cluster theories applied to the uniform electron gas (UEG) in the large-momentum-transfer limit, allowing for a detailed investigation of the basis set incompleteness error (BSIE) in these theories. While the dominance of MP2 and PPL contributions in CCD is well-established from previous works, this study explores all additional terms in CCD. Particularly, it is revealed that in MP3 theory, which corresponds to a low-order approximation of CCD (here referred to as the linear terms of $\text{CCD}^{(1)}$), all diagrammatic contributions, except MP2 and PPL, exhibit faster convergence, specifically as $N_v^{-5/3}$ or $N_v^{-7/3}$. On the other hand, in CCD theory, all different diagrammatic contributions converge slowly

as N_{v}^{-1}. This behavior is attributed to the coupling of amplitude elements with small and large momenta in the PPL term, as well as other contributions. Nevertheless, it has been shown that MP2 and PPL remain the dominant terms across various densities and electron numbers. The analysis also extends to the transition structure factor, showing a distinctive q^{-4} decay only for the MP2 and PPL terms at large momentum transfers. Overall, these key findings hold within the range of realistic densities, $1.0\,\mathrm{a.u.} \leq r_s \leq 5.0\,\mathrm{a.u.}$ and, exhibit minimal dependence on the number of electrons in the system.

For the (T) contribution a similar decomposition into three different channels was carried out. It was shown that for large values of q only one of the channels shows a leading order contribution. In CCD, however, due to the basis set incompleteness of the employed doubles amplitudes, all three channels show the same N_{v}^{-1} decay. Specifically, it was shown that there are essentially two major contributions to the overall BSIE: (i) a term which stems from elements with large momentum transfer on the additional Coulomb interaction of (T), which is only dominantly present in the so-called (T)-pp channel, and (ii) contributions which are linked to the basis set incompleteness of the underlying CCD amplitudes. The latter contribution is significant for all three different channels, (T)-pp, (T)-ph, and (T)-hh. Additionally, the relative strength of the three different channels to the total BSIE depends on the number of electrons and the employed density.

Finally, the BSIE of the recently proposed (cT) approach was investigated. It was shown that the additional contributions beyond the (T) approach show only a small BSIE. This is desirable as this new approach was conceptualize as a non-diverging perturbative triples correction for zero-gap systems. The mentioned divergence occurs for small values of q, whereas the BSIE is attributed mainly in the regime of large values of q.

Chapter 5

Summary and conclusions

Ab initio wavefunction methods, such as coupled-cluster theory, have proven successful in accurately predicting molecular properties. Over the last decade, there has been a shift in focus towards their application in electronic structure theory, aiming for systematic improvability in predicting various material properties. However, computationally, two challenges must be addressed: approaching the thermodynamic and complete basis set limits. The central theme of this thesis has been the exploration and computational development of coupled-cluster theories in these regimes, particularly when applied to the Uniform Electron Gas, an archetype for metallic systems.

In Chapter 3, our primary focus was on applying various levels of coupled-cluster theories, including CCD and CCD(T), to the Uniform Electron Gas (UEG). The goal was to conduct a detailed analytical and numerical analysis of these theories when employed in metallic systems, aiming to identify their characteristics and limitations as they approach the thermodynamic limit. For the UEG, it is known that the infrared divergence in second-order perturbation theory can be averted by including higher-order contributions, particularly corresponding to ring diagrams. Our numerical analysis revealed that ring-type diagrams, play a crucial role, possessing the leading-order contribution in the long-wavelength limit, in contrast to the other terms included in the

CCD method. This inclusion results in convergent CCD correlation energies at metallic densities.

However, the inclusion of higher-order excitations is essential for achieving accurate results compared to experimental data. Our numerical demonstrations confirmed the known divergence of CCD(T) in metallic systems. Through analytical and numerical findings, we successfully identified and incorporated specific triple excitation terms essential for curing the infrared catastrophe present in the CCD(T) method.

Consequently, we introduced coupled-cluster doubles plus complete perturbative triples, denoted as CCSD(cT), a highly accurate and computationally efficient theory tailored to achieve chemical accuracy in *ab initio* calculations of real metals. Applying CCSD(cT) to molecular systems demonstrated its ability to retain the desirable properties of CCSD(T), providing high accuracy at a reduced computational cost. Notably, the method proved applicable to metallic lithium, aligning well with experimental estimates of the cohesive energy. Our work also suggests that embedding CCSD into the Random Phase Approximation (RPA) holds promise for metals and might contribute to understanding the discrepancies observed between Diffusion Monte Carlo (DMC) and CCSD(T) interaction energies in large molecules.

Furthermore, in chapter 4 we focused on investigating the basis set incompleteness error (BSIE), which arises from the truncation of the employed basis functions, in coupled-cluster correlation energies for the uniform electron gas. Utilizing coupled-cluster doubles (CCD) theory, the study explores a range of parameters including densities, basis set sizes, and electron numbers. An in-depth analysis of individual contributions to amplitudes at the CCD level is conducted, revealing that only two terms, the MP2 and particle-particle ladder term, significantly impact the asymptotic large momentum behavior corresponding to the cusp region at short interelectronic distances. The coupling in amplitude equations results in a universal asymptotic convergence behavior for all CCD decomposed correlation energy contributions toward the complete basis set limit.

These findings support the success of a recent correction to the basis set incompleteness error in coupled-cluster theory. Chapter 4 concludes with an examination of the BSIE

in both CCD(T) and the newly proposed CCD(cT) methods, paving the way for future correction schemes for these methods.

In conclusion, our work contributes to the advancement of coupled-cluster theories, providing the CCSD(cT) method as a powerful tool for metal simulations. The comprehensive analysis of coupled-cluster theories for the UEG sheds light on the BSIE and convergence behavior, offering valuable insights for electronic structure calculations in materials science. The developed theories and our findings not only demonstrate improved accuracy but also address challenges concerning the high computational cost of wavefunction methods.

Appendix A

Pair correlation function and structure factor

In this appendix, we present the fundamental definitions and properties of the pair correlation function and its Fourier transform, known as the structure factor.

The pair correlation function, denoted as $g(\mathbf{r}_1, \mathbf{r}_2)$, is defined as the normalized probability of simultaneously finding an electron at $\mathbf{r}_1$ and another at $\mathbf{r}_2$:

$$g(\mathbf{r}_1, \mathbf{r}_2) \equiv \frac{1}{n(\mathbf{r}_1)n(\mathbf{r}_2)} \left\langle \sum_{i \neq j} \delta(\mathbf{r}_1 - \mathbf{r}_i)\delta(\mathbf{r}_2 - \mathbf{r}_j) \right\rangle, \tag{A.1}$$

where the angular brackets represent the average in the ground-state. This expression can also be rewritten in terms of the density operator:

$$g(\mathbf{r}_1, \mathbf{r}_2) = \frac{\langle \hat{n}(\mathbf{r}_1)\hat{n}(\mathbf{r}_2) \rangle}{n(\mathbf{r}_1)n(\mathbf{r}_2)} - \frac{\delta(\mathbf{r}_1 - \mathbf{r}_2)}{n(\mathbf{r}_1)}, \tag{A.2}$$

where the second term excludes the trivial correlation of a particle with *itself*. In the limit of large separation $|\mathbf{r}_1 - \mathbf{r}_2|$, the correlation between $\hat{n}(\mathbf{r}_1)$ and $\hat{n}(\mathbf{r}_2)$ is expected to vanish. Therefore, the average $\langle \hat{n}(\mathbf{r}_1)\hat{n}(\mathbf{r}_2) \rangle$ should reduce to the product of the two independent averages, i.e. $n(\mathbf{r}_1)n(\mathbf{r}_2)$. Thus we have,

$$\lim_{|\mathbf{r}_1 - \mathbf{r}_2| \to \infty} g(\mathbf{r}_1, \mathbf{r}_2) = 1. \tag{A.3}$$

In a homogeneous and isotropic system, such as the Uniform Electron Gas, $g(\mathbf{r}_1, \mathbf{r}_2)$ is a function of the magnitude of $\mathbf{r} = |\mathbf{r}_1 - \mathbf{r}_2|$, and in that case, we denote it as $g(\mathbf{r}, 0) \equiv g(\mathbf{r})$. Additionally, the quantity

$$h(\mathbf{r}_1, \mathbf{r}_2) = n(\mathbf{r}_2)[g(\mathbf{r}_1, \mathbf{r}_2) - 1], \tag{A.4}$$

describes the modification of the average electronic density at $\mathbf{r}_2$ due to the presence of an electron at $\mathbf{r}_1$. This quantity, when integrated over all space, must be equal to -1 because if an electron is present at $\mathbf{r}_1$, then it is not somewhere else, implying a net deficiency of one electron in the rest of the system. Thus, we have the important sum rule:

$$\int d^3\, r_2 h(\mathbf{r}_1, \mathbf{r}_2) = -1, \tag{A.5}$$

which explains why $h(\mathbf{r}_1, \mathbf{r}_2)$ is commonly referred to as the exchange-correlation hole for an electron at $\mathbf{r}_1$.

In a non-interacting Fermi system, the antisymmetry of the wave function ensures that $h(\mathbf{r}_1, \mathbf{r}_2)$ is everywhere negative, meaning the presence of an electron at $\mathbf{r}_1$ causes a reduction in electron density everywhere else. This depletion effect is known as the exchange hole and can be easily quantified starting from the second-quantized expression for $g(\mathbf{r}_1, \mathbf{r}_2)$:

$$g(\mathbf{r}_1, \mathbf{r}_2) = \sum_{\sigma_1, \sigma_2} \frac{\langle \hat{\psi}^\dagger_{\sigma_2}(\mathbf{r}_2) \hat{\psi}^\dagger_{\sigma_1}(\mathbf{r}_1) \hat{\psi}_{\sigma_1}(\mathbf{r}_1) \hat{\psi}_{\sigma_2}(\mathbf{r}_2) \rangle}{n(\mathbf{r}_1) n(\mathbf{r}_2)}, \tag{A.6}$$

where the average is taken in the ground-state of the non-interacting system. This average is evaluated with the help of Wick's theorem, by decomposing it into the sum of products of averages of pairs of operators. This leads us to the following general expression for the pair correlation function of a non-interacting Fermi system:

$$g^{(0)}(\mathbf{r}_1, \mathbf{r}_2) = 1 - \sum_{\sigma_1, \sigma_2} \frac{|\langle \hat{\psi}^\dagger_{\sigma_1}(\mathbf{r}_1) \hat{\psi}_{\sigma_2}(\mathbf{r}_2) \rangle|^2}{n(\mathbf{r}_1) n(\mathbf{r}_2)} \tag{A.7}$$

which is manifestly smaller than 1, thus proving the negativity of the exchange hole. In general, however, the pair correlation function of an interacting Fermi system can be larger than 1, and the full exchange-correlation hole $h(\mathbf{r}_1, \mathbf{r}_2)$ can be positive in some ranges of separations, even though it satisfies the global constraint Eq. (A.5).

The pair correlation function $g(\mathbf{r}_1, \mathbf{r}_2)$ as defined thus far is "blind" to the spin of the electrons. For a more detailed description of positional and spin correlations, we introduce the spin-resolved pair correlation function:

$$g_{\sigma_1\sigma_2}(\mathbf{r}_1, \mathbf{r}_2) = \frac{\langle \hat{n}_{\sigma_1}(\mathbf{r}_1)\hat{n}_{\sigma_2}(\mathbf{r}_2)\rangle}{n_{\sigma_1}(\mathbf{r}_1)n_{\sigma_2}(\mathbf{r}_2)} - \delta_{\sigma_1\sigma_2}\frac{\delta(\mathbf{r}_1 - \mathbf{r}_2)}{n_{\sigma_1}(\mathbf{r}_1)}, \tag{A.8}$$

which gives the probability of simultaneously finding an electron at $\mathbf{r}_1$ with spin projection σ_1 and another at $\mathbf{r}_2$ with spin projection σ_2. The normalization is chosen in a way that still fulfills:

$$\lim_{|\mathbf{r}_1 - \mathbf{r}_2|\to\infty} g_{\sigma\sigma'}(\mathbf{r}_1, \mathbf{r}_2) = 1. \tag{A.9}$$

It is evident that the complete pair correlation function is obtained from the spin-resolved one in the following manner:

$$g(\mathbf{r}_1, \mathbf{r}_2) = \sum_{\sigma_1,\sigma_2} \frac{g_{\sigma_1\sigma_2}(\mathbf{r}_1, \mathbf{r}_2)n_{\sigma_1}(\mathbf{r}_1)n_{\sigma_2}(\mathbf{r}_2)}{n(\mathbf{r}_1)n(\mathbf{r}_2)}. \tag{A.10}$$

It is often useful to express the pair correlation function $g_{\sigma\sigma'}(\mathbf{r}_1, \mathbf{r}_2)$ in terms of the relative coordinate $\mathbf{r} = \mathbf{r}_1 - \mathbf{r}_2$ and the center of mass $\mathbf{R} = \frac{\mathbf{r}_1+\mathbf{r}_2}{2}$. The resulting function $g_{\sigma\sigma'}(\mathbf{r}, \mathbf{R})$ satisfies the so-called cusp conditions, in which:

$$\lim_{\mathbf{r}\to 0} \frac{\partial g_{\uparrow\uparrow}(\mathbf{r}, \mathbf{R})}{\partial \mathbf{r}}\bigg|_{\mathbf{r}=0} = 0, \tag{A.11}$$

and

$$\lim_{\mathbf{r}\to 0} \frac{\partial g_{\uparrow\downarrow}(\mathbf{r}, \mathbf{R})}{\partial \mathbf{r}}\bigg|_{\mathbf{r}=0} = g_{\uparrow\downarrow}(0, \mathbf{R}). \tag{A.12}$$

These relations follow from the fact that the short-range behavior of the pair correlation function is controlled by the coulomb repulsion between just two electrons. . We conclude this brief summary of properties of the pair correlation function by presenting the results for $g_{\sigma\sigma'}(\mathbf{r})$ in a uniform non-interacting electron gas. In this case $g_{\uparrow\downarrow} = g_{\downarrow\uparrow} = 1$ at all distances because there are no Pauli correlations between non-interacting electrons of opposite spin. Then Eq. (A.7) and Eq. (A.10) easily lead us to:

$$g^{(0)}_{\sigma\sigma'}(\mathbf{r}) = 1 - \delta_{\sigma\sigma'}\left|\frac{1}{N_\sigma}\sum_{k\le k_F} e^{-i\mathbf{k}\cdot\mathbf{r}}\right|^2. \tag{A.13}$$

The sum over wave vectors can be evaluated analytically, yielding with the following results:

$$\frac{1}{N_\sigma}\sum_{k\leq k_F} e^{-i\mathbf{k}\cdot\mathbf{r}} = 3\frac{sin(k_F r) - k_F r cos(k_F r)}{(k_F r)^3}. \tag{A.14}$$

The structure factor

The structure factor $S(q)$ of a translationally invariant system is defined in terms of the pair correlation function as follows:

$$S(q) = 1 + n\int d^3r\,[g(\mathbf{r}) - 1]e^{-i\mathbf{q}\cdot\mathbf{r}}, \tag{A.15}$$

with the inverse of this relation being

$$g(\mathbf{r}) - 1 = \frac{1}{n}\int \frac{d^3q}{(2\pi)^3}\,[S(q) - 1]e^{i\mathbf{q}\cdot\mathbf{r}}. \tag{A.16}$$

Additionally, the sum rule Eq. (A.5) ensures that:

$$\lim_{q\to 0} S(q) = 0. \tag{A.17}$$

More precisely, it can be shown that the cusp conditions Eq. (A.11) and Eq. (A.12) imply the following limiting behavior for the structure factor

$$\lim_{q\to\infty} q^4[S(q) - 1] = -8\pi n g(0). \tag{A.18}$$

Substituting the form Eq. (A.1) of $g(\mathbf{r})$ in Eq. (A.15), we obtain an expression for $S(q)$ in terms of the Fourier components of the density fluctuation operator:

$$S(q) = \sum_{i,j}\frac{\langle e^{-i\mathbf{q}\cdot(\hat{\mathbf{r}}_i - \hat{\mathbf{r}}_j)}\rangle}{N} = \frac{\langle \hat{n}_{-q}\hat{n}_q\rangle}{N}. \tag{A.19}$$

Thus, $S(q)$ serves as a measure of the average squared amplitude of density fluctuations with a wave vector q. The spin-resolved version of the structure factor is given by:

$$S_{\sigma\sigma'}(q) = \frac{\langle \hat{n}_{-q,\sigma}\hat{n}_{q,\sigma'}\rangle}{N} = \frac{n_\sigma}{n}\delta_{\sigma\sigma'} + \frac{n_\sigma n_{\sigma'}}{n}\int d^3r\,[g_{\sigma\sigma'}(\mathbf{r}) - 1]e^{-i\mathbf{q}\cdot\mathbf{r}}, \tag{A.20}$$

with

$$S(q) = \sum_{\sigma,\sigma'} S_{\sigma\sigma'}(q). \tag{A.21}$$

The structure factor of the noninteracting electron gas at zero temperature can be calculated directly from the definition Eq. (A.19). The results in three dimensions are:

$$S^{(0)}_{\sigma\sigma'}(q) = \frac{3q}{8k_F} - \frac{q^3}{32k_F^3}, \qquad \text{for} \quad q \leq 2k_F, \tag{A.22}$$

$$S^{(0)}_{\sigma\sigma'}(q) = \frac{\delta_{\sigma\sigma'}}{2}, \qquad \text{for} \quad q > 2k_F. \tag{A.23}$$

Appendix B

Analytic structure and limiting behavior of the rCCD amplitudes in the long wavelength limit

In this appendix, we will briefly present the main points of Freeman's work on the coupled-cluster treatment of the correlation energy of the Uniform Electron Gas within the ring or Randon Phase Approximation. Ring diagrams constitute a specific class of perturbation theory diagrams summed to infinite order in the $\hat{T}_2$ or CCD equations. The ring-CCD equations take the form:

$$(\varepsilon_i + \varepsilon_j - \varepsilon_a - \varepsilon_b)t_{ij}^{ab} = v_{ij}^{ab} + 2\sum_{kc} v_{ic}^{ak} t_{kj}^{cb} + 2\sum_{kc} t_{ik}^{ac} v_{cj}^{kb} + 4\sum_{klcd} t_{ik}^{ac} v_{cd}^{kl} t_{lj}^{db}. \quad \text{(B.1)}$$

In the following analysis, we will represent the vectors of the reciprocal space without a bold notation; for instance, $\mathbf{k}_r \equiv k_r$. For tensor notation, we will utilize the subscripts of the reciprocal vectors. For the UEG, the Coulomb matrix elements are given by:

$$v_{ij}^{ab} = \frac{4\pi}{\Omega|k_a - k_i|^2}\delta_{k_a - k_i, k_j - k_b} = \frac{4\pi}{\Omega|q|^2}\delta_{k_a - k_i, k_j - k_b}, \qquad \text{with} \qquad q = k_a - k_i, \quad \text{(B.2)}$$

where q is the momentum transferred by the Coulomb interaction. Due to the conservation of momentum flow in the matrix elements, the coupled-cluster double amplitudes

t_{ij}^{ab} depend on the momenta of the two spatial occupied eigenstates, $i \equiv k_i$ and $j \equiv k_j$, as well as on the momentum flow q, namely,

$$t_{ij}^{ab} \equiv t_{k_i k_j}^{k_i+q;k_j-q} \equiv t_{ij}(q). \tag{B.3}$$

Consequently, Eq. (B.1) takes the form:

$$\begin{aligned} t_{ij}(q) = \frac{4\pi}{\Omega|q|^2 D(k_i,k_j,q)} \Bigg(& 1 + 2\sum_k [t_{kj}(q) + t_{ik}(q)]\theta(k_k)[1-\theta(k_k+q)] \\ & + 4\sum_{kl} [t_{ik}(q)t_{lj}(q)]\theta(k_k)\theta(k_l)\times \\ & \times [1-\theta(k_k+q)][1-\theta(k_l+q)] \Bigg), \end{aligned} \tag{B.4}$$

where we define the difference of the unoccupied one-particle eigenenergies from the occupied as:

$$(\varepsilon_i + \varepsilon_j - \varepsilon_a - \varepsilon_b) \equiv D(k_i,k_j,q) = q \cdot (q + k_i + k_j), \tag{B.5}$$

and refer to it as the *energy denominator*. To reduce the dimensionality of the equations, it is convenient to define the function:

$$T_i(q) = \sum_k t_{ik}(q)\theta(k_k)[1-\theta(k_k+q)], \tag{B.6}$$

so that Eq. (B.4) becomes:

$$t_{ij}(q) = \frac{4\pi}{\Omega|q|^2 D(k_i,k_j,q)} \Big(1 + 2[T_j(q) + T_i(q)] + 4[T_i(q)T_j(q)]\Big). \tag{B.7}$$

We can obtain an algebraic equation for $T_i(q)$ by summing Eq. (B.7) on both sides over k_j. The result is:

$$\begin{aligned} T_i(q) = \sum_{k_j} \frac{4\pi}{\Omega|q|^2 D(k_i,k_j,q)} \Big(1 + 2[T_j(q) + T_i(q)] + 4[T_i(q)T_j(q)]\Big)\times \\ \times \theta(k_j)[1-\theta(k_j+q)]. \end{aligned} \tag{B.8}$$

By rearranging Eq. (B.8), it is possible to show that:

$$\lim_{q\to 0} T_r(q) = -\frac{1}{2}. \tag{B.9}$$

By substituting Eq. (B.9) into Eq. (B.7), we arrive at:

$$\lim_{q\to 0} t_{ij}(q) = f(k_i, k_j)q^{-1}, \tag{B.10}$$

where $f(k_i, k_j)$ is a bounded and weak function of k_i and k_j, eventually, leading to convergent correlation energies.

Appendix C

Atomic structures of the bcc lithium supercells

All the data are presented in units of Ångstrom.

Table C.1: *26 atoms, volume of cell : 535.21*

Lattice Vectors of the Cell

6.905 952 995	−3.452 976 497	3.452 976 497
0.000 000 000	6.905 952 995	3.452 976 497
−3.452 976 498	−3.452 976 497	6.905 952 995

Length of Vectors

8.458 030 512	7.721 090 173	8.458 030 512

Position of Ions in Fractional Coordinates

0.000 000 000	0.000 000 000	0.000 000 000
0.923 076 923	0.384 615 385	0.846 153 846
0.615 384 615	0.923 076 923	0.230 769 231
0.461 538 462	0.692 307 692	0.923 076 923
0.846 153 846	0.769 230 769	0.692 307 692
0.153 846 154	0.230 769 231	0.307 692 308
0.538 461 538	0.307 692 308	0.076 923 077
0.230 769 231	0.846 153 846	0.461 538 462
0.384 615 385	0.076 923 077	0.769 230 769
0.769 230 769	0.153 846 154	0.538 461 538
0.076 923 077	0.615 384 615	0.153 846 154
0.307 692 308	0.461 538 462	0.615 384 615
0.692 307 692	0.538 461 538	0.384 615 385
0.230 769 231	0.346 153 846	0.961 538 462
0.153 846 154	0.730 769 231	0.807 692 308
0.846 153 846	0.269 230 769	0.192 307 692
0.692 307 692	0.038 461 538	0.884 615 385
0.076 923 077	0.115 384 615	0.653 846 154
0.384 615 385	0.576 923 077	0.269 230 769
0.769 230 769	0.653 846 154	0.038 461 538
0.461 538 462	0.192 307 692	0.423 076 923
0.615 384 615	0.423 076 923	0.730 769 231
0.000 000 000	0.500 000 000	0.500 000 000
0.307 692 308	0.961 538 462	0.115 384 615
0.538 461 538	0.807 692 308	0.576 923 077
0.923 076 923	0.884 615 385	0.346 153 846

Table C.2: *44 atoms, volume of cell : 905.74*

Lattice Vectors of the Cell

3.452 976 497	−6.905 952 995	6.905 952 995
0.000 000 000	6.905 952 995	6.905 952 995
−6.905 952 995	−3.452 976 497	6.905 952 995

Length of Vectors

10.358 929 492	9.766 492 386	10.358 929 492

Position of Ions in Fractional Coordinates

0.000 000 000	0.000 000 000	0.000 000 000
0.454 545 455	0.818 181 818	0.727 272 727
0.727 272 727	0.409 090 909	0.363 636 364
0.727 272 727	0.909 090 909	0.363 636 364
0.181 818 182	0.227 272 727	0.090 909 091
0.909 090 909	0.636 363 636	0.454 545 455
0.090 909 091	0.863 636 364	0.545 454 545
0.363 636 364	0.454 545 455	0.181 818 182
0.818 181 818	0.272 727 273	0.909 090 909
0.272 727 273	0.090 909 091	0.636 363 636
0.545 454 545	0.681 818 182	0.272 727 273
0.363 636 364	0.954 545 455	0.181 818 182
0.000 000 000	0.500 000 000	0.000 000 000
0.454 545 455	0.318 181 818	0.727 272 727
0.181 818 182	0.727 272 727	0.090 909 091
0.636 363 636	0.545 454 545	0.818 181 818
0.909 090 909	0.136 363 636	0.454 545 455
0.090 909 091	0.363 636 364	0.545 454 545
0.818 181 818	0.772 727 273	0.909 090 909
0.272 727 273	0.590 909 091	0.636 363 636

0.545 454 545	0.181 818 182	0.272 727 273
0.636 363 636	0.045 454 545	0.818 181 818
0.136 363 636	0.295 454 545	0.818 181 818
0.590 909 091	0.113 636 364	0.545 454 545
0.863 636 364	0.704 545 455	0.181 818 182
0.863 636 364	0.204 545 455	0.181 818 182
0.318 181 818	0.522 727 273	0.909 090 909
0.045 454 545	0.931 818 182	0.272 727 273
0.227 272 727	0.159 090 909	0.363 636 364
0.500 000 000	0.750 000 000	0.000 000 000
0.954 545 455	0.568 181 818	0.727 272 727
0.409 090 909	0.386 363 636	0.454 545 455
0.681 818 182	0.977 272 727	0.090 909 091
0.500 000 000	0.250 000 000	0.000 000 000
0.136 363 636	0.795 454 545	0.818 181 818
0.590 909 091	0.613 636 364	0.545 454 545
0.318 181 818	0.022 727 273	0.909 090 909
0.772 727 273	0.840 909 091	0.636 363 636
0.045 454 545	0.431 818 182	0.272 727 273
0.227 272 727	0.659 090 909	0.363 636 364
0.954 545 455	0.068 181 818	0.727 272 727
0.409 090 909	0.886 363 636	0.454 545 455
0.681 818 182	0.477 272 727	0.090 909 091
0.772 727 273	0.340 909 091	0.636 363 636

Table C.3: *68 atoms, volume of cell : 1399.78*

Lattice Vectors of the Cell

10.358 929 492	3.452 976 497	3.452 976 497
0.000 000 000	6.905 952 995	10.358 929 492
3.452 976 497	−10.358 929 492	3.452 976 497

Length of Vectors

11.452 227 451	12.449 883 814	11.452 227 451

Position of Ions in Fractional Coordinates

0.000 000 000	0.000 000 000	0.000 000 000
0.176 470 588	0.117 647 059	0.470 588 235
0.352 941 176	0.235 294 118	0.941 176 471
0.029 411 765	0.352 941 176	0.911 764 706
0.852 941 176	0.235 294 118	0.441 176 471
0.529 411 765	0.352 941 176	0.411 764 706
0.705 882 353	0.470 588 235	0.882 352 941
0.205 882 353	0.470 588 235	0.382 352 941
0.382 352 941	0.588 235 294	0.852 941 176
0.058 823 529	0.705 882 353	0.823 529 412
0.882 352 941	0.588 235 294	0.352 941 176
0.558 823 529	0.705 882 353	0.323 529 412
0.735 294 118	0.823 529 412	0.794 117 647
0.235 294 118	0.823 529 412	0.294 117 647
0.411 764 706	0.941 176 471	0.764 705 882
0.088 235 294	0.058 823 529	0.735 294 118
0.911 764 706	0.941 176 471	0.264 705 882
0.588 235 294	0.058 823 529	0.235 294 118
0.764 705 882	0.176 470 588	0.705 882 353
0.264 705 882	0.176 470 588	0.205 882 353
0.441 176 471	0.294 117 647	0.676 470 588
0.117 647 059	0.411 764 706	0.647 058 824
0.941 176 471	0.294 117 647	0.176 470 588
0.617 647 059	0.411 764 706	0.147 058 824
0.794 117 647	0.529 411 765	0.617 647 059
0.294 117 647	0.529 411 765	0.117 647 059

0.470 588 235	0.647 058 824	0.588 235 294
0.147 058 824	0.764 705 882	0.558 823 529
0.970 588 235	0.647 058 824	0.088 235 294
0.647 058 824	0.764 705 882	0.058 823 529
0.823 529 412	0.882 352 941	0.529 411 765
0.323 529 412	0.882 352 941	0.029 411 765
0.500 000 000	0.000 000 000	0.500 000 000
0.676 470 588	0.117 647 059	0.970 588 235
0.176 470 588	0.117 647 059	0.970 588 235
0.352 941 176	0.235 294 118	0.441 176 471
0.529 411 765	0.352 941 176	0.911 764 706
0.205 882 353	0.470 588 235	0.882 352 941
0.029 411 765	0.352 941 176	0.411 764 706
0.705 882 353	0.470 588 235	0.382 352 941
0.882 352 941	0.588 235 294	0.852 941 176
0.382 352 941	0.588 235 294	0.352 941 176
0.558 823 529	0.705 882 353	0.823 529 412
0.235 294 118	0.823 529 412	0.794 117 647
0.058 823 529	0.705 882 353	0.323 529 412
0.735 294 118	0.823 529 412	0.294 117 647
0.911 764 706	0.941 176 471	0.764 705 882
0.411 764 706	0.941 176 471	0.264 705 882
0.588 235 294	0.058 823 529	0.735 294 118
0.264 705 882	0.176 470 588	0.705 882 353
0.088 235 294	0.058 823 529	0.235 294 118
0.764 705 882	0.176 470 588	0.205 882 353
0.941 176 471	0.294 117 647	0.676 470 588
0.441 176 471	0.294 117 647	0.176 470 588
0.617 647 059	0.411 764 706	0.647 058 824
0.294 117 647	0.529 411 765	0.617 647 059
0.117 647 059	0.411 764 706	0.147 058 824
0.794 117 647	0.529 411 765	0.117 647 059

0.970 588 235	0.647 058 824	0.588 235 294
0.470 588 235	0.647 058 824	0.088 235 294
0.647 058 824	0.764 705 882	0.558 823 529
0.323 529 412	0.882 352 941	0.529 411 765
0.147 058 824	0.764 705 882	0.058 823 529
0.823 529 412	0.882 352 941	0.029 411 765
0.000 000 000	0.000 000 000	0.500 000 000
0.500 000 000	0.000 000 000	0.000 000 000
0.676 470 588	0.117 647 059	0.470 588 235
0.852 941 176	0.235 294 118	0.941 176 471

Table C.4: *128 atoms, volume of cell : 2634.88*

Lattice Vectors of the Cell

13.811 905 989	0.000 000 000	0.000 000 000
0.000 000 000	13.811 905 989	0.000 000 000
0.000 000 000	0.000 000 000	13.811 905 989

Length of Vectors

13.811 905 989	13.811 905 989	13.811 905 989

Position of Ions in Fractional Coordinates

0.000 000 000	0.000 000 000	0.000 000 000
0.000 000 000	0.000 000 000	0.250 000 000
0.000 000 000	0.000 000 000	0.500 000 000
0.000 000 000	0.000 000 000	0.750 000 000
0.000 000 000	0.250 000 000	0.000 000 000
0.000 000 000	0.250 000 000	0.250 000 000
0.000 000 000	0.250 000 000	0.500 000 000
0.000 000 000	0.250 000 000	0.750 000 000

0.000 000 000	0.500 000 000	0.000 000 000
0.000 000 000	0.500 000 000	0.250 000 000
0.000 000 000	0.500 000 000	0.500 000 000
0.000 000 000	0.500 000 000	0.750 000 000
0.000 000 000	0.750 000 000	0.000 000 000
0.000 000 000	0.750 000 000	0.250 000 000
0.000 000 000	0.750 000 000	0.500 000 000
0.000 000 000	0.750 000 000	0.750 000 000
0.250 000 000	0.000 000 000	0.000 000 000
0.250 000 000	0.000 000 000	0.250 000 000
0.250 000 000	0.000 000 000	0.500 000 000
0.250 000 000	0.000 000 000	0.750 000 000
0.250 000 000	0.250 000 000	0.000 000 000
0.250 000 000	0.250 000 000	0.250 000 000
0.250 000 000	0.250 000 000	0.500 000 000
0.250 000 000	0.250 000 000	0.750 000 000
0.250 000 000	0.500 000 000	0.000 000 000
0.250 000 000	0.500 000 000	0.250 000 000
0.250 000 000	0.500 000 000	0.500 000 000
0.250 000 000	0.500 000 000	0.750 000 000
0.250 000 000	0.750 000 000	0.000 000 000
0.250 000 000	0.750 000 000	0.250 000 000
0.250 000 000	0.750 000 000	0.500 000 000
0.250 000 000	0.750 000 000	0.750 000 000
0.500 000 000	0.000 000 000	0.000 000 000
0.500 000 000	0.000 000 000	0.250 000 000
0.500 000 000	0.000 000 000	0.500 000 000
0.500 000 000	0.000 000 000	0.750 000 000
0.500 000 000	0.250 000 000	0.000 000 000
0.500 000 000	0.250 000 000	0.250 000 000
0.500 000 000	0.250 000 000	0.500 000 000
0.500 000 000	0.250 000 000	0.750 000 000

0.500 000 000	0.500 000 000	0.000 000 000
0.500 000 000	0.500 000 000	0.250 000 000
0.500 000 000	0.500 000 000	0.500 000 000
0.500 000 000	0.500 000 000	0.750 000 000
0.500 000 000	0.750 000 000	0.000 000 000
0.500 000 000	0.750 000 000	0.250 000 000
0.500 000 000	0.750 000 000	0.500 000 000
0.500 000 000	0.750 000 000	0.750 000 000
0.750 000 000	0.000 000 000	0.000 000 000
0.750 000 000	0.000 000 000	0.250 000 000
0.750 000 000	0.000 000 000	0.500 000 000
0.750 000 000	0.000 000 000	0.750 000 000
0.750 000 000	0.250 000 000	0.000 000 000
0.750 000 000	0.250 000 000	0.250 000 000
0.750 000 000	0.250 000 000	0.500 000 000
0.750 000 000	0.250 000 000	0.750 000 000
0.750 000 000	0.500 000 000	0.000 000 000
0.750 000 000	0.500 000 000	0.250 000 000
0.750 000 000	0.500 000 000	0.500 000 000
0.750 000 000	0.500 000 000	0.750 000 000
0.750 000 000	0.750 000 000	0.000 000 000
0.750 000 000	0.750 000 000	0.250 000 000
0.750 000 000	0.750 000 000	0.500 000 000
0.750 000 000	0.750 000 000	0.750 000 000
0.125 000 000	0.125 000 000	0.125 000 000
0.125 000 000	0.125 000 000	0.375 000 000
0.125 000 000	0.125 000 000	0.625 000 000
0.125 000 000	0.125 000 000	0.875 000 000
0.125 000 000	0.375 000 000	0.125 000 000
0.125 000 000	0.375 000 000	0.375 000 000
0.125 000 000	0.375 000 000	0.625 000 000
0.125 000 000	0.375 000 000	0.875 000 000

0.125 000 000	0.625 000 000	0.125 000 000
0.125 000 000	0.625 000 000	0.375 000 000
0.125 000 000	0.625 000 000	0.625 000 000
0.125 000 000	0.625 000 000	0.875 000 000
0.125 000 000	0.875 000 000	0.125 000 000
0.125 000 000	0.875 000 000	0.375 000 000
0.125 000 000	0.875 000 000	0.625 000 000
0.125 000 000	0.875 000 000	0.875 000 000
0.375 000 000	0.125 000 000	0.125 000 000
0.375 000 000	0.125 000 000	0.375 000 000
0.375 000 000	0.125 000 000	0.625 000 000
0.375 000 000	0.125 000 000	0.875 000 000
0.375 000 000	0.375 000 000	0.125 000 000
0.375 000 000	0.375 000 000	0.375 000 000
0.375 000 000	0.375 000 000	0.625 000 000
0.375 000 000	0.375 000 000	0.875 000 000
0.375 000 000	0.625 000 000	0.125 000 000
0.375 000 000	0.625 000 000	0.375 000 000
0.375 000 000	0.625 000 000	0.625 000 000
0.375 000 000	0.625 000 000	0.875 000 000
0.375 000 000	0.875 000 000	0.125 000 000
0.375 000 000	0.875 000 000	0.375 000 000
0.375 000 000	0.875 000 000	0.625 000 000
0.375 000 000	0.875 000 000	0.875 000 000
0.625 000 000	0.125 000 000	0.125 000 000
0.625 000 000	0.125 000 000	0.375 000 000
0.625 000 000	0.125 000 000	0.625 000 000
0.625 000 000	0.125 000 000	0.875 000 000
0.625 000 000	0.375 000 000	0.125 000 000
0.625 000 000	0.375 000 000	0.375 000 000
0.625 000 000	0.375 000 000	0.625 000 000
0.625 000 000	0.375 000 000	0.875 000 000

0.625 000 000	0.625 000 000	0.125 000 000
0.625 000 000	0.625 000 000	0.375 000 000
0.625 000 000	0.625 000 000	0.625 000 000
0.625 000 000	0.625 000 000	0.875 000 000
0.625 000 000	0.875 000 000	0.125 000 000
0.625 000 000	0.875 000 000	0.375 000 000
0.625 000 000	0.875 000 000	0.625 000 000
0.625 000 000	0.875 000 000	0.875 000 000
0.875 000 000	0.125 000 000	0.125 000 000
0.875 000 000	0.125 000 000	0.375 000 000
0.875 000 000	0.125 000 000	0.625 000 000
0.875 000 000	0.125 000 000	0.875 000 000
0.875 000 000	0.375 000 000	0.125 000 000
0.875 000 000	0.375 000 000	0.375 000 000
0.875 000 000	0.375 000 000	0.625 000 000
0.875 000 000	0.375 000 000	0.875 000 000
0.875 000 000	0.625 000 000	0.125 000 000
0.875 000 000	0.625 000 000	0.375 000 000
0.875 000 000	0.625 000 000	0.625 000 000
0.875 000 000	0.625 000 000	0.875 000 000
0.875 000 000	0.875 000 000	0.125 000 000
0.875 000 000	0.875 000 000	0.375 000 000
0.875 000 000	0.875 000 000	0.625 000 000
0.875 000 000	0.875 000 000	0.875 000 000

Table C.5: *208 atoms, volume of cell : 4281.68*

Lattice Vectors of the Cell

13.811 905 989	−6.905 952 995	6.905 952 995
0.000 000 000	13.811 905 989	6.905 952 995
−6.905 952 995	−6.905 952 995	13.811 905 989

Length of Vectors

16.916 061 024	15.442 180 345	16.916 061 024

Position of Ions in Fractional Coordinates

0.000 000 000	0.000 000 000	0.000 000 000
0.923 076 923	0.384 615 385	0.846 153 846
0.615 384 615	0.923 076 923	0.230 769 231
0.461 538 462	0.692 307 692	0.923 076 923
0.846 153 846	0.769 230 769	0.692 307 692
0.153 846 154	0.230 769 231	0.307 692 308
0.538 461 538	0.307 692 308	0.076 923 077
0.230 769 231	0.846 153 846	0.461 538 462
0.384 615 385	0.076 923 077	0.769 230 769
0.769 230 769	0.153 846 154	0.538 461 538
0.076 923 077	0.615 384 615	0.153 846 154
0.307 692 308	0.461 538 462	0.615 384 615
0.692 307 692	0.538 461 538	0.384 615 385
0.076 923 077	0.115 384 615	0.153 846 154
0.000 000 000	0.500 000 000	0.000 000 000
0.692 307 692	0.038 461 538	0.384 615 385
0.538 461 538	0.807 692 308	0.076 923 077
0.923 076 923	0.884 615 385	0.846 153 846
0.230 769 231	0.346 153 846	0.461 538 462
0.615 384 615	0.423 076 923	0.230 769 231
0.307 692 308	0.961 538 462	0.615 384 615
0.461 538 462	0.192 307 692	0.923 076 923
0.846 153 846	0.269 230 769	0.692 307 692
0.153 846 154	0.730 769 231	0.307 692 308
0.384 615 385	0.576 923 077	0.769 230 769
0.769 230 769	0.653 846 154	0.538 461 538

0.961 538 462	0.192 307 692	0.923 076 923
0.884 615 385	0.576 923 077	0.769 230 769
0.576 923 077	0.115 384 615	0.153 846 154
0.423 076 923	0.884 615 385	0.846 153 846
0.807 692 308	0.961 538 462	0.615 384 615
0.115 384 615	0.423 076 923	0.230 769 231
0.500 000 000	0.500 000 000	0.000 000 000
0.192 307 692	0.038 461 538	0.384 615 385
0.346 153 846	0.269 230 769	0.692 307 692
0.730 769 231	0.346 153 846	0.461 538 462
0.038 461 538	0.807 692 308	0.076 923 077
0.269 230 769	0.653 846 154	0.538 461 538
0.653 846 154	0.730 769 231	0.307 692 308
0.038 461 538	0.307 692 308	0.076 923 077
0.961 538 462	0.692 307 692	0.923 076 923
0.653 846 154	0.230 769 231	0.307 692 308
0.500 000 000	0.000 000 000	0.000 000 000
0.884 615 385	0.076 923 077	0.769 230 769
0.192 307 692	0.538 461 538	0.384 615 385
0.576 923 077	0.615 384 615	0.153 846 154
0.269 230 769	0.153 846 154	0.538 461 538
0.423 076 923	0.384 615 385	0.846 153 846
0.807 692 308	0.461 538 462	0.615 384 615
0.115 384 615	0.923 076 923	0.230 769 231
0.346 153 846	0.769 230 769	0.692 307 692
0.730 769 231	0.846 153 846	0.461 538 462
0.192 307 692	0.038 461 538	0.884 615 385
0.115 384 615	0.423 076 923	0.730 769 231
0.807 692 308	0.961 538 462	0.115 384 615
0.653 846 154	0.730 769 231	0.807 692 308
0.038 461 538	0.807 692 308	0.576 923 077
0.346 153 846	0.269 230 769	0.192 307 692

0.730 769 231	0.346 153 846	0.961 538 462
0.423 076 923	0.884 615 385	0.346 153 846
0.576 923 077	0.115 384 615	0.653 846 154
0.961 538 462	0.192 307 692	0.423 076 923
0.269 230 769	0.653 846 154	0.038 461 538
0.500 000 000	0.500 000 000	0.500 000 000
0.884 615 385	0.576 923 077	0.269 230 769
0.269 230 769	0.153 846 154	0.038 461 538
0.192 307 692	0.538 461 538	0.884 615 385
0.884 615 385	0.076 923 077	0.269 230 769
0.730 769 231	0.846 153 846	0.961 538 462
0.115 384 615	0.923 076 923	0.730 769 231
0.423 076 923	0.384 615 385	0.346 153 846
0.807 692 308	0.461 538 462	0.115 384 615
0.500 000 000	0.000 000 000	0.500 000 000
0.653 846 154	0.230 769 231	0.807 692 308
0.038 461 538	0.307 692 308	0.576 923 077
0.346 153 846	0.769 230 769	0.192 307 692
0.576 923 077	0.615 384 615	0.653 846 154
0.961 538 462	0.692 307 692	0.423 076 923
0.153 846 154	0.230 769 231	0.807 692 308
0.076 923 077	0.615 384 615	0.653 846 154
0.769 230 769	0.153 846 154	0.038 461 538
0.615 384 615	0.923 076 923	0.730 769 231
0.000 000 000	0.000 000 000	0.500 000 000
0.307 692 308	0.461 538 462	0.115 384 615
0.692 307 692	0.538 461 538	0.884 615 385
0.384 615 385	0.076 923 077	0.269 230 769
0.538 461 538	0.307 692 308	0.576 923 077
0.923 076 923	0.384 615 385	0.346 153 846
0.230 769 231	0.846 153 846	0.961 538 462
0.461 538 462	0.692 307 692	0.423 076 923

0.846 153 846	0.769 230 769	0.192 307 692
0.230 769 231	0.346 153 846	0.961 538 462
0.153 846 154	0.730 769 231	0.807 692 308
0.846 153 846	0.269 230 769	0.192 307 692
0.692 307 692	0.038 461 538	0.884 615 385
0.076 923 077	0.115 384 615	0.653 846 154
0.384 615 385	0.576 923 077	0.269 230 769
0.769 230 769	0.653 846 154	0.038 461 538
0.461 538 462	0.192 307 692	0.423 076 923
0.615 384 615	0.423 076 923	0.730 769 231
0.000 000 000	0.500 000 000	0.500 000 000
0.307 692 308	0.961 538 462	0.115 384 615
0.538 461 538	0.807 692 308	0.576 923 077
0.923 076 923	0.884 615 385	0.346 153 846
0.115 384 615	0.173 076 923	0.980 769 231
0.038 461 538	0.557 692 308	0.826 923 077
0.730 769 231	0.096 153 846	0.211 538 462
0.576 923 077	0.865 384 615	0.903 846 154
0.961 538 462	0.942 307 692	0.673 076 923
0.269 230 769	0.403 846 154	0.288 461 538
0.653 846 154	0.480 769 231	0.057 692 308
0.346 153 846	0.019 230 769	0.442 307 692
0.500 000 000	0.250 000 000	0.750 000 000
0.884 615 385	0.326 923 077	0.519 230 769
0.192 307 692	0.788 461 538	0.134 615 385
0.423 076 923	0.634 615 385	0.596 153 846
0.807 692 308	0.711 538 462	0.365 384 615
0.192 307 692	0.288 461 538	0.134 615 385
0.115 384 615	0.673 076 923	0.980 769 231
0.807 692 308	0.211 538 462	0.365 384 615
0.653 846 154	0.980 769 231	0.057 692 308
0.038 461 538	0.057 692 308	0.826 923 077

0.346 153 846	0.519 230 769	0.442 307 692
0.730 769 231	0.596 153 846	0.211 538 462
0.423 076 923	0.134 615 385	0.596 153 846
0.576 923 077	0.365 384 615	0.903 846 154
0.961 538 462	0.442 307 692	0.673 076 923
0.269 230 769	0.903 846 154	0.288 461 538
0.500 000 000	0.750 000 000	0.750 000 000
0.884 615 385	0.826 923 077	0.519 230 769
0.076 923 077	0.365 384 615	0.903 846 154
0.000 000 000	0.750 000 000	0.750 000 000
0.692 307 692	0.288 461 538	0.134 615 385
0.538 461 538	0.057 692 308	0.826 923 077
0.923 076 923	0.134 615 385	0.596 153 846
0.230 769 231	0.596 153 846	0.211 538 462
0.615 384 615	0.673 076 923	0.980 769 231
0.307 692 308	0.211 538 462	0.365 384 615
0.461 538 462	0.442 307 692	0.673 076 923
0.846 153 846	0.519 230 769	0.442 307 692
0.153 846 154	0.980 769 231	0.057 692 308
0.384 615 385	0.826 923 077	0.519 230 769
0.769 230 769	0.903 846 154	0.288 461 538
0.153 846 154	0.480 769 231	0.057 692 308
0.076 923 077	0.865 384 615	0.903 846 154
0.769 230 769	0.403 846 154	0.288 461 538
0.615 384 615	0.173 076 923	0.980 769 231
0.000 000 000	0.250 000 000	0.750 000 000
0.307 692 308	0.711 538 462	0.365 384 615
0.692 307 692	0.788 461 538	0.134 615 385
0.384 615 385	0.326 923 077	0.519 230 769
0.538 461 538	0.557 692 308	0.826 923 077
0.923 076 923	0.634 615 385	0.596 153 846
0.230 769 231	0.096 153 846	0.211 538 462

0.461 538 462	0.942 307 692	0.673 076 923
0.846 153 846	0.019 230 769	0.442 307 692
0.307 692 308	0.211 538 462	0.865 384 615
0.230 769 231	0.596 153 846	0.711 538 462
0.923 076 923	0.134 615 385	0.096 153 846
0.769 230 769	0.903 846 154	0.788 461 538
0.153 846 154	0.980 769 231	0.557 692 308
0.461 538 462	0.442 307 692	0.173 076 923
0.846 153 846	0.519 230 769	0.942 307 692
0.538 461 538	0.057 692 308	0.326 923 077
0.692 307 692	0.288 461 538	0.634 615 385
0.076 923 077	0.365 384 615	0.403 846 154
0.384 615 385	0.826 923 077	0.019 230 769
0.615 384 615	0.673 076 923	0.480 769 231
0.000 000 000	0.750 000 000	0.250 000 000
0.384 615 385	0.326 923 077	0.019 230 769
0.307 692 308	0.711 538 462	0.865 384 615
0.000 000 000	0.250 000 000	0.250 000 000
0.846 153 846	0.019 230 769	0.942 307 692
0.230 769 231	0.096 153 846	0.711 538 462
0.538 461 538	0.557 692 308	0.326 923 077
0.923 076 923	0.634 615 385	0.096 153 846
0.615 384 615	0.173 076 923	0.480 769 231
0.769 230 769	0.403 846 154	0.788 461 538
0.153 846 154	0.480 769 231	0.557 692 308
0.461 538 462	0.942 307 692	0.173 076 923
0.692 307 692	0.788 461 538	0.634 615 385
0.076 923 077	0.865 384 615	0.403 846 154
0.269 230 769	0.403 846 154	0.788 461 538
0.192 307 692	0.788 461 538	0.634 615 385
0.884 615 385	0.326 923 077	0.019 230 769
0.730 769 231	0.096 153 846	0.711 538 462

0.115 384 615	0.173 076 923	0.480 769 231
0.423 076 923	0.634 615 385	0.096 153 846
0.807 692 308	0.711 538 462	0.865 384 615
0.500 000 000	0.250 000 000	0.250 000 000
0.653 846 154	0.480 769 231	0.557 692 308
0.038 461 538	0.557 692 308	0.326 923 077
0.346 153 846	0.019 230 769	0.942 307 692
0.576 923 077	0.865 384 615	0.403 846 154
0.961 538 462	0.942 307 692	0.173 076 923
0.346 153 846	0.519 230 769	0.942 307 692
0.269 230 769	0.903 846 154	0.788 461 538
0.961 538 462	0.442 307 692	0.173 076 923
0.807 692 308	0.211 538 462	0.865 384 615
0.192 307 692	0.288 461 538	0.634 615 385
0.500 000 000	0.750 000 000	0.250 000 000
0.884 615 385	0.826 923 077	0.019 230 769
0.576 923 077	0.365 384 615	0.403 846 154
0.730 769 231	0.596 153 846	0.711 538 462
0.115 384 615	0.673 076 923	0.480 769 231
0.423 076 923	0.134 615 385	0.096 153 846
0.653 846 154	0.980 769 231	0.557 692 308
0.038 461 538	0.057 692 308	0.326 923 077

Publications, conferences and miscellaneous

Publications

Peer reviewed

- Averting the Infrared Catastrophe in the Gold Standard of Quantum Chemistry
  Masios, Nikolaos and Irmler, Andreas and Schäfer, Tobias and Grüneis, Andreas
  2023, American Physical Society (APS), 10.1103/PhysRevLett.131.186401

Under review

- Investigating the basis set convergence of diagrammatically decomposed coupled-cluster correlation energy contributions for the uniform electron gas
  Masios, Nikolaos and Hummel, Felix and Grüneis, Andreas and Irmler, Andreas
  arXiv:2402.15907

Conferences

- Psi-k (Ψ_k) Conference, poster presentation, *August 2022, Lausanne, Switzerland*
  Towards chemical accuracy in metals using renormalized coupled-cluster theories

Miscellaneous

- *cc4ueg*, C++ code for coupled-cluster methods applied on the Uniform Electron Gas; available on `https://github.com/nmasios/cc4ueg.git`.

List of Figures

List of Tables

Bibliography

[1] E. Schrödinger. Quantisierung als eigenwertproblem. *Annalen der Physik*, 385:437–490, 1926.

[2] Trygve Helgaker, Poul Jørgensen, and Jeppe Olsen. *Molecular Electronic-Structure Theory*. John Wiley & Sons, Ltd, 8 2000.

[3] Chr. Møller and M. S. Plesset. Note on an approximation treatment for many-electron systems. *Physical Review*, 46:618–622, 1934.

[4] Tobias Schäfer, Benjamin Ramberger, and Georg Kresse. Quartic scaling mp2 for solids: A highly parallelized algorithm in the plane wave basis. *The Journal of Chemical Physics*, 146:104101, 3 2017.

[5] Tobias Schäfer, Benjamin Ramberger, and Georg Kresse. Laplace transformed mp2 for three dimensional periodic materials using stochastic orbitals in the plane wave basis and correlated sampling. *The Journal of Chemical Physics*, 148, 2 2018.

[6] Isaiah Shavitt and Rodney J Bartlett. *Many-body methods in chemistry and physics: MBPT and coupled-cluster theory*. Cambridge University Press, 2009.

[7] So Hirata, Ireneusz Grabowski, Motoi Tobita, and Rodney J. Bartlett. Highly accurate treatment of electron correlation in polymers: coupled-cluster and many-body perturbation theories. *Chemical Physics Letters*, 345(5):475–480, 2001.

[8] David L. Freeman. Coupled-cluster expansion applied to the electron gas: Inclusion of ring and exchange effects. *Phys. Rev. B*, 15(12):5512–5521, June 1977.

[9] Gustavo E. Scuseria, Thomas M. Henderson, and Danny C. Sorensen. The ground state correlation energy of the random phase approximation from a ring coupled

cluster doubles approach. *The Journal of Chemical Physics*, 129(23):231101, 12 2008.

[10] Krishnan Raghavachari, Gary W. Trucks, John A. Pople, and Martin Head-Gordon. A fifth-order perturbation comparison of electron correlation theories. *Chemical Physics Letters*, 157(6):479–483, 1989.

[11] James J. Shepherd and Andreas Grüneis. Many-body quantum chemistry for the electron gas: Convergent perturbative theories. *Phys. Rev. Lett.*, 110:226401, May 2013.

[12] Piotr Piecuch, Stanisław A. Kucharski, Karol Kowalski, and Monika Musiał. Efficient computer implementation of the renormalized coupled-cluster methods: The r-ccsd[t], r-ccsd(t), cr-ccsd[t], and cr-ccsd(t) approaches. *Computer Physics Communications*, 149(2):71–96, 2002.

[13] F. Coester and H. Kümmel. Short-range correlations in nuclear wave functions. *Nucl. Phys.*, 17:477–485, June 1960.

[14] Jiří Čížek. On the Use of the Cluster Expansion and the Technique of Diagrams in Calculations of Correlation Effects in Atoms and Molecules. In R. LeFebvre and C. Moser, editors, *Advances in Chemical Physics*, pages 35–89. John Wiley & Sons, Inc., 1969.

[15] W. Kohn and L. J. Sham. Self-consistent equations including exchange and correlation effects. *Phys. Rev.*, 140:A1133–A1138, Nov 1965.

[16] A. L. Fetter and J. D. Walecka. *Quantum Theory of Many-Particle Systems*. McGraw-Hill, Boston, 1971.

[17] Alexander Altland and Ben D. Simons. *Condensed Matter Field Theory*. Cambridge University Press, 2 edition, 2010.

[18] Louisa M. Fraser, W. M. C. Foulkes, G. Rajagopal, R. J. Needs, S. D. Kenny, and A. J. Williamson. Finite-size effects and coulomb interactions in quantum monte

carlo calculations for homogeneous systems with periodic boundary conditions. *Phys. Rev. B*, 53:1814–1832, Jan 1996.

[19] cc4ueg; available on `https://github.com/nmasios/cc4ueg.git`.

[20] Attila Szabo and Neil S Ostlund. *Modern quantum chemistry: introduction to advanced electronic structure theory*. Dover Publications, Mineola, N.Y., 1996.

[21] Richard D. Mattuck. *A guide to Feynman diagrams in the many-body problem*. Dover books on physics and chemistry. Dover Publications, New York, 2nd edition, 1992.

[22] Lars Onsager, Laurence Mittag, and Michael J. Stephen. Integrals in the theory of electron correlations. *Annalen der Physik*, 473:71–77, 1966.

[23] Frank E. Harris, Hendrik J. (Hendrik Jan) Monkhorst, and David L. Freeman. *Algebraic and diagrammatic methods in many-fermion theory*. 1992.

[24] Alec F. White and Garnet Kin-Lic Chan. Finite-temperature coupled cluster: Efficient implementation and application to prototypical systems. *The Journal of Chemical Physics*, 152:224104, 6 2020.

[25] Artem Pulkin and Garnet Kin-Lic Chan. First-principles coupled cluster theory of the electronic spectrum of transition metal dichalcogenides. *Physical Review B*, 101, 6 2020.

[26] Qiming Sun, Timothy C. Berkelbach, James D. McClain, and Garnet Kin-Lic Chan. Gaussian and plane-wave mixed density fitting for periodic systems. *The Journal of Chemical Physics*, 147:164119, 10 2017.

[27] James McClain, Qiming Sun, Garnet Kin-Lic Chan, and Timothy C. Berkelbach. Gaussian-based coupled-cluster theory for the ground state and band structure of solids. *Journal of Chemical Theory and Computation*, 13:1209–1218, 1 2017.

[28] Thomas Gruber, Ke Liao, Theodoros Tsatsoulis, Felix Hummel, and Andreas Grüneis. Applying the coupled-cluster ansatz to solids and surfaces in the thermodynamic limit. *Physical Review X*, 8, 2018.

[29] Felix Hummel, Thomas Gruber, and Andreas Grüneis. A many-electron perturbation theory study of the hexagonal boron nitride bilayer system*. *The European Physical Journal B*, 89(11):235, 11 2016.

[30] Gustavo E. Scuseria, Timothy J. Lee, and Henry F. Schaefer. Accelerating the convergence of the coupled-cluster approach: The use of the diis method. *Chemical Physics Letters*, 130(3):236–239, 1986.

[31] Ke Liao and Andreas Grüneis. Communication: Finite size correction in periodic coupled cluster theory calculations of solids. *The Journal of Chemical Physics*, 145(14):141102, 10 2016.

[32] Tina N. Mihm, Bingdi Yang, and James J. Shepherd. Power laws used to extrapolate the coupled cluster correlation energy to the thermodynamic limit. *Journal of Chemical Theory and Computation*, 17(5):2752–2758, 2021. PMID: 33830754.

[33] Tina N. Mihm, William Z. Van Benschoten, and James J. Shepherd. Accelerating convergence to the thermodynamic limit with twist angle selection applied to methods beyond many-body perturbation theory. *The Journal of Chemical Physics*, 154(2):024113, 01 2021.

[34] Laura Weiler, Tina N. Mihm, and James J. Shepherd. Machine learning for a finite size correction in periodic coupled cluster theory calculations. *The Journal of Chemical Physics*, 156(20):204109, 05 2022.

[35] Thomas Gruber, Ke Liao, Theodoros Tsatsoulis, Felix Hummel, and Andreas Grüneis. Applying the coupled-cluster ansatz to solids and surfaces in the thermodynamic limit. *Phys. Rev. X*, 8:021043, 5 2018.

[36] Tina N. Mihm, Laura Weiler, and James J. Shepherd. How the exchange energy can affect the power laws used to extrapolate the coupled cluster correlation energy to the thermodynamic limit. *Journal of Chemical Theory and Computation*, 19(6):1686–1697, 2023. PMID: 36918372.

[37] Tina N. Mihm, Alexandra R. McIsaac, and James J. Shepherd. An optimized twist angle to find the twist-averaged correlation energy applied to the uniform electron gas. *The Journal of Chemical Physics*, 150(19):191101, 05 2019.

[38] Tosio Kato. On the eigenfunctions of many-particle systems in quantum mechanics. *Communications on Pure and Applied Mathematics*, 10:151–177, 1957.

[39] Tosio Kato. Fundamental properties of hamiltonian operators of schrödinger type. *Transactions of the American Mathematical Society*, 70:195–195, 2 1951.

[40] Christof Hättig, Wim Klopper, Andreas Köhn, and David P. Tew. Explicitly correlated electrons in molecules. *Chemical Reviews*, 112(1):4–74, 2012.

[41] Andreas Irmler, Alejandro Gallo, Felix Hummel, and Andreas Grüneis. Duality of ring and ladder diagrams and its importance for many-electron perturbation theories. *Phys. Rev. Lett.*, 123:156401, Oct 2019.

[42] Andreas Grüneis, James J. Shepherd, Ali Alavi, David P. Tew, and George H. Booth. Explicitly correlated plane waves: Accelerating convergence in periodic wavefunction expansions. *The Journal of Chemical Physics*, 139(8):084112, 08 2013.

[43] Nikolaos Masios, Andreas Irmler, Tobias Schäfer, and Andreas Grüneis. Averting the infrared catastrophe in the gold standard of quantum chemistry. *Phys. Rev. Lett.*, 131:186401, Oct 2023.

[44] Dipayan Datta and Mark S. Gordon. A massively parallel implementation of the ccsd(t) method using the resolution-of-the-identity approximation and a hybrid distributed/shared memory parallelization model. *Journal of Chemical Theory and Computation*, 17(8):4799–4822, 2021. PMID: 34279094.

[45] Peter J. Feibelman, B. Hammer, J. K. Nørskov, F. Wagner, M. Scheffler, R. Stumpf, R. Watwe, and J. Dumesic. The co/pt(111) puzzle. *The Journal of Physical Chemistry B*, 105(18):4018–4025, 2001.

[46] M. Pozzo and D. Alfè. Hydrogen dissociation on mg(0001) studied via quantum monte carlo calculations. *Phys. Rev. B*, 78:245313, Dec 2008.

[47] Katharina Doblhoff-Dier, Jörg Meyer, Philip E. Hoggan, and Geert-Jan Kroes. Quantum monte carlo calculations on a benchmark molecule–metal surface reaction: H2 + cu(111). *Journal of Chemical Theory and Computation*, 13(7):3208–3219, 2017. PMID: 28514594.

[48] Norbert Nemec, Michael D. Towler, and R. J. Needs. Benchmark all-electron ab initio quantum monte carlo calculations for small molecules. *The Journal of Chemical Physics*, 132(3):034111, 2010.

[49] Rodney J. Bartlett and Monika Musiał. Coupled-cluster theory in quantum chemistry. *Rev. Mod. Phys.*, 79:291–352, Feb 2007.

[50] George H Booth, Andreas Grüneis, Georg Kresse, and Ali Alavi. Towards an exact description of electronic wavefunctions in real solids. *Nature*, 493(7432):365–70, 2013.

[51] James McClain, Qiming Sun, Garnet Kin-Lic Chan, and Timothy C. Berkelbach. Gaussian-based coupled-cluster theory for the ground state and band structure of solids. *J. Chem. Theory Comput.*, 13(3):1209–1218, 2017.

[52] Jun Yang, Weifeng Hu, Denis Usvyat, Devin Matthews, Martin Schütz, and Garnet Kin-Lic Chan. Ab initio determination of the crystalline benzene lattice energy to sub-kilojoule/mole accuracy. *Science*, 345(6197):640–643, 2014.

[53] Andreas Grüneis. A coupled cluster and møller-plesset perturbation theory study of the pressure induced phase transition in the lih crystal. *The Journal of Chemical Physics*, 143(10):102817, 2015.

[54] Laura Weiler, Tina N. Mihm, and James J. Shepherd. Machine learning for a finite size correction in periodic coupled cluster theory calculations. *The Journal of Chemical Physics*, 156(20), 05 2022. 204109.

[55] Thomas Gruber and Andreas Grüneis. Ab initio calculations of carbon and boron nitride allotropes and their structural phase transitions using periodic coupled cluster theory. *Phys. Rev. B*, 98:134108, Oct 2018.

[56] Andreas Irmler, Alejandro Gallo, and Andreas Grüneis. Focal-point approach with pair-specific cusp correction for coupled-cluster theory. *The Journal of Chemical Physics*, 154(23):234103, 2021.

[57] Tina N. Mihm, Tobias Schäfer, Sai Kumar Ramadugu, Laura Weiler, Andreas Grüneis, and James J. Shepherd. A shortcut to the thermodynamic limit for quantum many-body calculations of metals. *Nature Computational Science*, 1(12):801–808, Dec 2021.

[58] Verena A. Neufeld, Hong-Zhou Ye, and Timothy C. Berkelbach. Ground-state properties of metallic solids from ab initio coupled-cluster theory. *The Journal of Physical Chemistry Letters*, 13(32):7497–7503, 2022. PMID: 35939802.

[59] Verena A. Neufeld and Alex J. W. Thom. A study of the dense uniform electron gas with high orders of coupled cluster. *The Journal of Chemical Physics*, 147(19):194105, 2017.

[60] Chr. Møller and M. S. Plesset. Note on an Approximation Treatment for Many-Electron Systems. *Phys. Rev.*, 46(7):618–622, October 1934.

[61] W. Macke. Über die Wechselwirkungen im Fermi-Gas, Polarisationserscheinungen, Correlationsenergie, Elektronenkondensation. *Z. Naturforsch.*, 5a(8):192–208, 1950.

[62] Murray Gell-Mann and Keith A. Brueckner. Correlation Energy of an Electron Gas at High Density. *Phys. Rev.*, 106(2):364–368, April 1957.

[63] Gustavo E. Scuseria, Thomas M. Henderson, and Danny C. Sorensen. The ground state correlation energy of the random phase approximation from a ring coupled cluster doubles approach. *J. Chem. Phys.*, 129(23):231101, 2008.

[64] K. Emrich and J. G. Zabolitzky. Electron correlations in the bogoljubov coupled-cluster formalism. *Phys. Rev. B*, 30:2049–2069, Aug 1984.

[65] R. F. Bishop and K. H. Lührmann. Electron correlations. ii. ground-state results at low and metallic densities. *Phys. Rev. B*, 26:5523–5557, 11 1982.

[66] Tina N. Mihm, Laura Weiler, and James J. Shepherd. How the exchange energy can affect the power laws used to extrapolate the coupled cluster correlation energy to the thermodynamic limit. *Journal of Chemical Theory and Computation*, 0(0):null, 2023. PMID: 36918372.

[67] Ke Liao and Andreas Grüneis. Communication: Finite size correction in periodic coupled cluster theory calculations of solids. *J. Chem. Phys.*, 145:141102, 2016.

[68] R.M. Martin, L. Reining, and D.M. Ceperley. *Interacting Electrons*. Cambridge University Press, 2016.

[69] Verena A. Neufeld and Timothy C. Berkelbach. Highly accurate electronic structure of metallic solids from coupled-cluster theory with nonperturbative triple excitations. 2023.

[70] Christof Hättig, Wim Klopper, Andreas Köhn, and David P. Tew. Explicitly correlated electrons in molecules. *Chemical Reviews*, 112(1):4–74, 2012. PMID: 22206503.

[71] James J. Shepherd, Thomas M. Henderson, and Gustavo E. Scuseria. Coupled cluster channels in the homogeneous electron gas. *J. Chem. Phys.*, 140(12):124102, 2014.

[72] N. D. Drummond, R. J. Needs, A. Sorouri, and W. M. C. Foulkes. Finite-size errors in continuum quantum monte carlo calculations. *Phys. Rev. B*, 78:125106, Sep 2008.

[73] C. Lin, F. H. Zong, and D. M. Ceperley. Twist-averaged boundary conditions in continuum quantum monte carlo algorithms. *Phys. Rev. E*, 64:016702, Jun 2001.

[74] M. Valiev, E.J. Bylaska, N. Govind, K. Kowalski, T.P. Straatsma, H.J.J. Van Dam, D. Wang, J. Nieplocha, E. Apra, T.L. Windus, and W.A. de Jong. Nwchem: A comprehensive and scalable open-source solution for large scale molecular simulations. *Comput. Phys. Commun.*, 181(9):1477 – 1489, 2010.

[75] cc4s; available from `https://manuals.cc4s.org`.

[76] Alejandro Gallo, Felix Hummel, Andreas Irmler, and Andreas Grüneis. A periodic equation-of-motion coupled-cluster implementation applied to f-centers in alkaline earth oxides. *J. Chem. Phys.*, 154(6):064106, 2021.

[77] Gerald Knizia, Thomas B. Adler, and Hans-Joachim Werner. Simplified ccsd(t)-f12 methods: Theory and benchmarks. *The Journal of Chemical Physics*, 130(5):054104, 2009.

[78] G Kresse and J Furthmüller. Efficient iterative schemes for {ab initio} total-energy calculations using a plane-wave basis set. *Phys. Rev. B*, 54(16):11169–11186, 15 October 1996.

[79] G. Kresse and D. Joubert. From ultrasoft pseudopotentials to the projector augmented-wave method. *Phys. Rev. B*, 59(3):1758–1775, 1999.

[80] Andreas Grüneis, George H. Booth, Martijn Marsman, James Spencer, Ali Alavi, and Georg Kresse. Natural orbitals for wave function based correlated calculations using a plane wave basis set. *J. Chem. Theory Comput.*, 7(9):2780–2785, 2011.

[81] Felix Hummel, Theodoros Tsatsoulis, and Andreas Grüneis. Low rank factorization of the coulomb integrals for periodic coupled cluster theory. *J. Chem. Phys.*, 146:124105, 2017.

[82] James J Shepherd, Andreas Grüneis, George H Booth, Georg Kresse, and Ali Alavi. Convergence of many-body wave-function expansions using a plane-wave basis: From homogeneous electron gas to solid state systems. *Phys. Rev. B*, 86(3):035111, 9 July 2012.

[83] P. López Ríos, A. Ma, N. D. Drummond, M. D. Towler, and R. J. Needs. Inhomogeneous backflow transformations in quantum monte carlo calculations. *Phys. Rev. E*, 74:066701, Dec 2006.

[84] Laurids Schimka, Judith Harl, and Georg Kresse. Improved hybrid functional for solids: The HSEsol functional. *The Journal of Chemical Physics*, 134(2), 01 2011. 024116.

[85] Tobias Schäfer, Florian Libisch, Georg Kresse, and Andreas Grüneis. Local embedding of coupled cluster theory into the random phase approximation using plane waves. *The Journal of Chemical Physics*, 154(1):011101, 2021.

[86] Tobias Schäfer, Alejandro Gallo, Andreas Irmler, Felix Hummel, and Andreas Grüneis. Surface science using coupled cluster theory via local wannier functions and in-rpa-embedding: The case of water on graphitic carbon nitride. *The Journal of Chemical Physics*, 155(24):244103, 2021.

[87] Yasmine S. Al-Hamdani, Péter R. Nagy, Andrea Zen, Dennis Barton, Mihály Kállay, Jan Gerit Brandenburg, and Alexandre Tkatchenko. Interactions between large molecules pose a puzzle for reference quantum mechanical methods. *Nature Communications*, 12(1):3927, Jun 2021.

[88] Nikolaos Masios, Felix Hummel, Andreas Grüneis, and Andreas Irmler. Investigating the basis set convergence of diagrammatically decomposed coupled-cluster correlation energy contributions for the uniform electron gas. *In preparation.*

[89] Elena Voloshina, Denis Usvyat, Martin Schütz, Yuriy Dedkov, and Beate Paulus. On the physisorption of water on graphene: a ccsd(t) study. *Phys. Chem. Chem. Phys.*, 13:12041, 2011.

[90] Adam Kubas, Daniel Berger, Harald Oberhofer, Dimitrios Maganas, Karsten Reuter, and Frank Neese. Surface adsorption energetics studied with "gold standard" wave-function-based ab initio methods: Small-molecule binding to tio2(110). *J. Phys. Chem. Lett*, 7(20):4207–4212, 2016.

[91] Jan Gerit Brandenburg, Andrea Zen, Martin Fitzner, Benjamin Ramberger, Georg Kresse, Theodoros Tsatsoulis, Andreas Grüneis, Angelos Michaelides, and Dario Alfè. Physisorption of water on graphene: Subchemical accuracy from many-body electronic structure methods. *The Journal of Physical Chemistry Letters*, 10(3):358–368, 2019.

[92] Theodoros Tsatsoulis, Sung Sakong, Axel Groß, and Andreas Grüneis. Reaction energetics of hydrogen on si(100) surface: A periodic many-electron theory study. *J. Chem. Phys.*, 149(24):244105, 2018.

[93] Joachim Sauer. Ab initio calculations for molecule–surface interactions with chemical accuracy. *Accounts of Chemical Research*, 52(12):3502–3510, 2019. PMID: 31765121.

[94] Bryan T. G. Lau, Gerald Knizia, and Timothy C. Berkelbach. Regional embedding enables high-level quantum chemistry for surface science. *The Journal of Physical Chemistry Letters*, 12(3):1104–1109, 2021. PMID: 33475362.

[95] Thomas Mullan, Lorenzo Maschio, Peter Saalfrank, and Denis Usvyat. Reaction barriers on non-conducting surfaces beyond periodic local mp2: Diffusion of hydrogen on alpha-al2o3(0001) as a test case. *The Journal of Chemical Physics*, 156(7):074109, 02 2022.

[96] Benjamin X. Shi, Andrea Zen, Venkat Kapil, Péter R. Nagy, Andreas Grüneis, and Angelos Michaelides. Many-body methods for surface chemistry come of age: Achieving consensus with experiments. *Journal of the American Chemical Society*, 0(0):null, 0. PMID: 37948071.

[97] Andreas Grüneis, James J Shepherd, Ali Alavi, David P Tew, and George H Booth. Explicitly correlated plane waves: accelerating convergence in periodic wavefunction expansions. *J. Chem. Phys.*, 139(8):084112, 28 August 2013.

[98] James M. Callahan, Malte F. Lange, and Timothy C. Berkelbach. Dynamical correlation energy of metals in large basis sets from downfolding and composite approaches. *The Journal of Chemical Physics*, 154(21):211105, 06 2021.

[99] Tosio Kato. On the eigenfunctions of many-particle systems in quantum mechanics. *Communications on Pure and Applied Mathematics*, 10:151–177, None 1957.

[100] Russell T Pack and W. Byers Brown. Cusp Conditions for Molecular Wavefunctions. *The Journal of Chemical Physics*, 45(2):556–559, 1966.

[101] John D. Morgan and Werner Kutzelnigg. Hund's rules, the alternating rule, and symmetry holes. *The Journal of Physical Chemistry*, 97:2425–2434, 03 1993.

[102] Werner Kutzelnigg and Wim Klopper. Wave functions with terms linear in the interelectronic coordinates to take care of the correlation cusp. i. general theory. *J. Chem. Phys.*, 94(3):1985, 1991.

[103] Seiichiro Ten-no. New implementation of second-order Møller-Plesset perturbation theory with an analytic Slater-type geminal. *The Journal of Chemical Physics*, 126(1):014108, 01 2007.

[104] Liguo Kong, Florian A. Bischoff, and Edward F. Valeev. Explicitly correlated r12/f12 methods for electronic structure. *Chemical Reviews*, 112(1):75–107, 2012.

[105] Andreas Grüneis, So Hirata, Yu-ya Ohnishi, and Seiichiro Ten-no. Perspective: Explicitly correlated electronic structure theory for complex systems. *The Journal of Chemical Physics*, 146(8):080901, 02 2017.

[106] Samuel Francis Boys, Nicholas Charles Handy, and John Wilfrid Linnett. A condition to remove the indeterminacy in interelectronic correlation functions. *Proc. Roy. Soc. London Ser. A.*, 309(1497):209–220, 1969.

[107] Samuel Francis Boys, Nicholas Charles Handy, and John Wilfrid Linnett. The determination of energies and wavefunctions with full electronic correlation. *Proc. Roy. Soc. London Ser. A.*, 310(1500):43–61, 1969.

[108] Ke Liao, Thomas Schraivogel, Hongjun Luo, Daniel Kats, and Ali Alavi. Towards efficient and accurate ab initio solutions to periodic systems via transcorrelation and coupled cluster theory. *Phys. Rev. Res.*, 3:033072, Jul 2021.

[109] Seiichiro Ten-no. A feasible transcorrelated method for treating electronic cusps using a frozen gaussian geminal. *Chem. Phys. Lett.*, 330(1):169 – 174, 2000.

[110] Aron J. Cohen, Hongjun Luo, Kai Guther, Werner Dobrautz, David P. Tew, and Ali Alavi. Similarity transformation of the electronic Schrödinger equation via Jastrow factorization. *The Journal of Chemical Physics*, 151(6):061101, 08 2019.

[111] David Feller. Benchmarks of improved complete basis set extrapolation schemes designed for standard ccsd(t) atomization energies. *J. Chem. Phys.*, 138(7):074103, 2013.

[112] David Pines and David Bohm. A Collective Description of Electron Interactions: II. Collective vs Individual Particle Aspects of the Interactions. *Phys. Rev.*, 85(2):338–353, January 1952.

[113] B. B. J. Hede and J. P. Carbotte. Spin-up-spin-down pair distribution function at metallic densities. *Canadian Journal of Physics*, 50(15):1756–1763, 1972.

[114] H Yasuhara. Short-range correlation in electron gas. *Solid State Commun.*, 11:1481–1483, 1972.

[115] K. S. Singwi, M. P. Tosi, R. H. Land, and A. Sjölander. Electron correlations at metallic densities. *Phys. Rev.*, 176:589–599, Dec 1968.

[116] Zhixin Qian. On-top pair-correlation function in the homogeneous electron liquid. *Physical Review B*, 73, 1 2006.

[117] Jerzy Cioslowski and Paul Ziesche. Applicability of the ladder theory to the three-dimensional homogeneous electron gas. *Physical Review B*, 71:125105, 3 2005.

[118] R.M. Martin. *Electronic Structure: Basic Theory and Practical Methods*. Cambridge University Press, 2004.

[119] Ravishankar Sundararaman and T. A. Arias. Regularization of the coulomb singularity in exact exchange by wigner-seitz truncated interactions: Towards chemical accuracy in nontrivial systems. *Phys. Rev. B*, 87:165122, Apr 2013.

[120] Yoon S. Lee and Rodney J. Bartlett. A study of Be2 with many-body perturbation theory and a coupled-cluster method including triple excitations. *The Journal of Chemical Physics*, 80(9):4371–4377, 05 1984.

[121] Yoon S. Lee, Stanislaw A. Kucharski, and Rodney J. Bartlett. A coupled cluster approach with triple excitations. *The Journal of Chemical Physics*, 81(12):5906–5912, 12 1984.

[122] Miroslav Urban, Jozef Noga, Samuel J. Cole, and Rodney J. Bartlett. Towards a full CCSDT model for electron correlation. *The Journal of Chemical Physics*, 83(8):4041–4046, 10 1985.

[123] Jozef Noga, Rodney J. Bartlett, and Miroslav Urban. Towards a full ccsdt model for electron correlation. ccsdt-n models. *Chemical Physics Letters*, 134(2):126–132, 1987.

[124] Krishnan Raghavachari, Gary W. Trucks, John A. Pople, and Martin Head-Gordon. A fifth-order perturbation comparison of electron correlation theories. *Chemical Physics Letters*, 157(6):479–483, 1989.

[125] Nikolaos Masios, Andreas Irmler, Tobias Schäfer, and Andreas Grüneis. Averting the infrared catastrophe in the gold standard of quantum chemistry, 2023.

[126] J. C. Kimball. Short-Range Correlations and Electron-Gas Response Functions. *Phys. Rev. A*, 7(5):1648–1652, May 1973.

[127] W. Klopper. Highly accurate coupled-cluster singlet and triplet pair energies from explicitly correlated calculations in comparison with extrapolation techniques. *Molecular Physics*, 99(6):481–507, 2001.

[128] Andreas Irmler and Andreas Grüneis. Particle-particle ladder based basis-set corrections applied to atoms and molecules using coupled-cluster theory. *The Journal of Chemical Physics*, 151(10):104107, 09 2019.

[129] Ericka C. Barnes, George A. Petersson, David Feller, and Kirk A. Peterson. The CCSD(T) complete basis set limit for Ne revisited. *The Journal of Chemical Physics*, 129(19):194115, 11 2008.

[130] Mihály Kállay, Réka A. Horváth, László Gyevi-Nagy, and Péter R. Nagy. Size-consistent explicitly correlated triple excitation correction. *The Journal of Chemical Physics*, 155(3):034107, 07 2021.

[131] Andreas Köhn. Explicitly correlated connected triple excitations in coupled-cluster theory. *J. Chem. Phys.*, 130(13):131101, 2009.

[132] Andreas Köhn. Explicitly correlated coupled-cluster theory using cusp conditions. II. Treatment of connected triple excitations. *J. Chem. Phys.*, 133(17):174118, 2010.